The Gravity Field of Venus and Its Relationship to the Dynamic Processes in the Mantle

Research report to the Czech National Grant No. 205/02/1306*

Martin Pauer

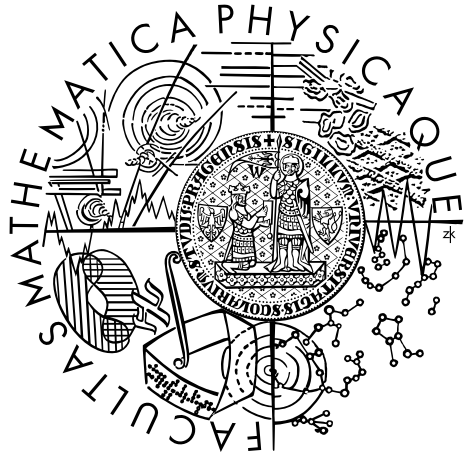

* This report was submitted as a diploma thesis
at the Department of Geophysics, Faculty of Mathematics and Physics,
Charles University, Prague, in April 2004.

Here I would like to give thanks to all the people who helped me in writing this diploma thesis. First of all to Ondřej Čadek for his kind care and to Jiří Zahradník for his everlasting enthusiasm. Then also to Luděk Vecsey for his help in investigating wavelet analysis and to Hana Čížková and Ctirad Matyska for their helpful advice and discussions. To the rest of our department for their kind and personal attitude toward the students, to Ondřej Santolík for his nice lectures on the magnetosphere, to Marie Běhounková for her valuable support during my studies, to Casey Heagerty for proofreading this thesis and to Ladislav Hanyk for his genuinely good mood.

Many thanks belong to my whole family who have supported me all these years and to my friends – without them I would probably not have completed my studies. And of course to my dear Martina who believed in me more than I did ...

Because the planetary sciences are not yet the subject of general studies in Czech I have several times during my work on this thesis asked foreign academic colleagues for help or materials, which they kindly provided. Therefore I wish to thank also Gerald Schubert (UCLA), Tilman Spohn (DLR), Ulrich Christensen (Max Planck Institute für Aeronomie), David Yuen (MSI), Greg Neumann (MIT), Alex Konopliv (JPL) and Donald Gurnett (University of Iowa).

Printed by LaTeX

Contents

Název práce: Gravitační pole Venuše a jeho vztah k dynamickým procesům v jejím plášti
Autor: Martin Pauer
Katedra (ústav): Katedra geofyziky, MFF UK v Praze
Vedoucí diplomové práce: Doc. RNDr. Ondřej Čadek, CSc.
E-mail vedoucího: oc@karel.troja.mff.cuni.cz
Abstrakt: Modelováním mechanismů vzniku geoidu Venuše lze získat cenné poznatky o vnitřní struktuře planety. Spektrum geoidu se nám daří rozdělit na dvě části a každou z nich vysvětlit samostatně v rámci jiné teorie kompenzace topografie. Na stupních $j > 40$ je vhodným mechanismem izostatická kompenzace kůry o jedné vrstvě s mocností 35 km; na stupních j=2-40 je vhodným kompenzačním mechanismem dynamické tečení v plášti. To v této práci modelujeme za použití teorie odezvových funkcí. Za předpokladu vztlakových sil měnících se pouze laterálně se nám daří vystihnout kolem 90% pozorovaného geoidu i topografie. Řešením obrácené úlohy pro viskózní strukturu dostáváme litosféru o mocnosti 100-200 km s viskozitou o několik řádů vyšší v porovnání s hlubšími partiemi. Pro zbytek pláště pak dostáváme nárůst viskozity směrem k jádru o 1-1.5 řádu bez přítomnosti ostře ohraničené zóny nízké viskozity (podobné astenosféře u Země). Predikované hodnoty dynamického geoidu i topografie jsou analyzovány pomocí spektrálních i lokalizačních metod a vykazují dobrou korelaci s pozorovanými daty.
Klíčová slova: Venuše, struktura pláště, viskozita, gravitační pole

Title: The Gravity Field of Venus and Its Relationship to Dynamic Processes in the Mantle
Author: Martin Pauer
Department: Department of Geophysics, MFF UK in Prague
Supervisor: Doc. RNDr. Ondřej Čadek, CSc.
Supervisor's e-mail address: oc@karel.troja.mff.cuni.cz
Abstract: Modelling Venus' gravity gives us acceptable constraints on the structure of the planet. We can successfully divide the geoid spectrum into two main parts and each of them explain on the basis of different topographic support. For a signal at degrees $j > 40$ it is appropriate to use the crustal-isostasy model with the one-layer crust of thickness 35 km; for degrees j=2-40 is the suitable compensation mechanism a dynamic flow in the mantle. In our work this is investigated in the framework of internal loading theory. When we assume that the buoyancy force is only varying laterally we can explain well about 90% of both the geoid and topography. By solving the inverse problem for a viscosity structure we obtain a lithosphere with a thickness 100-200 km and of a viscosity stiffer by several orders of magnitude than the deeper parts. For the rest of the mantle we obtain a viscosity increase towards the core by 1-1.5 orders of magnitude with no indication of a narrow low-viscosity zone (similar to Earth's asthenosphere). The predicted dynamic geoid and topography are analyzed by means of both spectral and localization methods and show a good correlation to the observed data.
Keywords: Venus, mantle structure, viscosity, gravity

Earth is the cradle of mankind.
But one cannot live in the cradle forever.

K. E. Ciolkovski (1857-1935)

Chapter 1

Introduction

In the case of planets other than Earth our knowledge of their interiors is very poor because, except for the Moon, we have no seismological observations which can give us direct information about their structure. Our only tool to uncover the subsurface structure and mantle properties is to carefully analyze the gravity/topography relations – both of these fields are precisely measured by orbiting space probes. This work's aim is to continue such efforts in the case of Venus, previously studied by other authors, with modifications of currently used methods and employing new data models obtained by recent analyses. Our effort is to identify the part of the geoid generated by dynamic processes in the mantle and then, by means of the inverse problem, find the best rheological model to reproduce it.

Basically this thesis is divided into two parts. Chapter 2 has a character of literature retrieval, where all the different findings concerning geophysics of Venus are reviewed – for identification of interdisciplinary links this section also contains parts focused on the magnetosphere and atmosphere of Venus. Chapter 3 deals with the used spherical harmonic models of geoid and topography and with the techniques of obtaining them.

Our own contribution to the understanding of Venus' structure comes in the chapters after these. In Chapter 4 the global estimates of the crustal thickness based on the isostasy for short wavelengths are made, and in Chapter 5 we applied the internal loading theory to explain the dynamic geoid and topography which are believed to be observed at long wavelengths on Venus. The test of our results by the multidimensional methods is done in Chapter 6 and the discussion of it with regards to the work of other authors in Chapter 7.

Because some of the materials included in this thesis are obtained from the internet, their reference is noted as [i?] and the list of sources is given at the end of the thesis. The supplemental CD contains the PDF version of this work, the source files of geoid and topography coefficients and some of the results in EPS format.

Chapter 2

Venus As We Know It

From the very beginnings of civilization people have known Venus as a morning or evening star. Its dense clouds (Fig. 2.1) reflect incident sun light so intensely that they could not overlook it. The Greeks named such stars which wandered through the sky among other fixed stars "planets", which means travellers. And perhaps for its brightness this planet got its name from the Roman goddess of beauty and love, Venus.

But the same dense clouds prevented the first astronomers from observing its surface after the telescope was invented. However, because of the physical similarity between Venus and our planet, it was for a long time accepted that the surface conditions would be the same. We had to wait until the radiotelescope was constructed and used for purposes of astronomy before we could learn more about this planet. The first radio reflections gave people suggestions of what could be hidden under the dense venusian atmosphere.

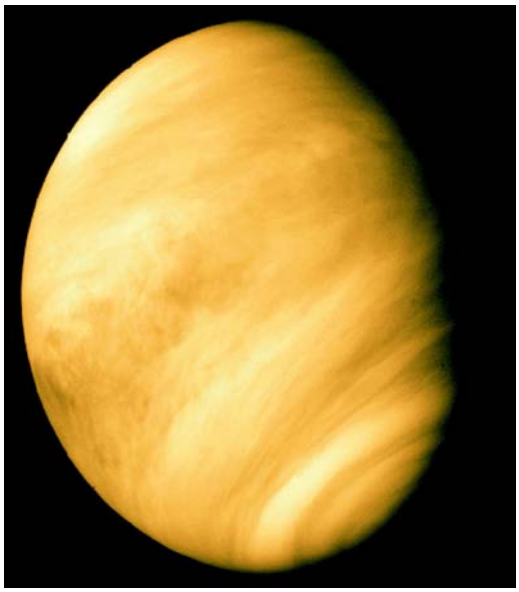

Figure 2.1: Venus observed in visible light [i1]

After WWII the time came to go into the space – first Sputnik in 1957 and then other spacecrafts. Both Russians and Americans tried to reach Venus with unmanned space probes – russian Veneras several times landed softly on the surface of Venus and worked until the hostile environment destroyed them. Americans succeeded with Pioneer Venus and Magellan missions to get into orbit, and so obtained important global observations.

People always speculated about Venus – maybe because it looked so similar to Earth. After getting the first data from space missions, the geoscientists focused on applying their knowledge of our planet to this body. Nowadays there is whole new scientific discipline called **planetology** and a lot of people work seriously on Venus research. Many questions have already been answered but more remain yet unsolved – one of them is the origin of Venus' geoid. Answering these questions will maybe lead us to discover of general rules of planetary behavior and this could help us to better understand our own planet Earth.

2.1 Structure of Venus

All we know about Venus are data recorded at ground-based facilities placed here on Earth, obtained by orbiting probes or by several landers – no interior data are available to help us if thinking about the structure and processes in Venus' interior. Therefore we often consider it as Earth's twin and try to apply the knowledge of our planet to our understanding of Venus. This assumption is allowed mainly because of the shared conditions during the Solar System's formation – the material composition does not differ too much, the main differences were probably just the abundance of water on Earth and the incoming energy from the Sun (which is greater on Venus because it is closer to our star than Earth).

2.1.1 Magnetic Field

Most of the planets of the Solar System have huge magnetospheres. These structures are often 10-100 times larger than the planet itself and in the cases of Mercury, Earth and the giant planets originate in the interior of the planets by the dynamo processes.

But in the case of Venus – as for comets – there is no internal mechanism producing the magnetic field. However, it is the interaction of a solar wind with the ionosphere (the part of the atmosphere with charged particles) that produces a weak magnetic field (e.g. Phillips and McComas, 1991). This field shows a behavior similar to an internally-generated one except for the dipole characteristics – the structure is shown in Fig. 2.2.

There the bow shock is formed in front of the ionosphere where the particles of the solar wind are decelerating to sub-Alfvénic and sub-sonic speeds. The magnetic lines and so even the solar wind particles accumulate in the magnetosheath behind the bow shock. This magnetosheath is separated from the ionosphere by the ionopause – here the plasma pressure is in the equilibrium with thermal pressure of venusian atmosphere. The interplanetary magnetic field is draped around the planet and forms an induced magnetotail behind it similar to Earth's but with polarity controlled solely by the surrounding field. Without the dipole field there is no system of trapped particles surrounding Venus.

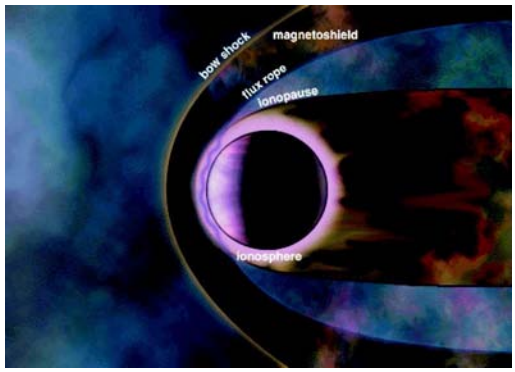

Figure 2.2: Structure of Venus' induced magnetosphere [i2]

2.1.2 Atmosphere

In the early state of the formation of the Solar System Venus probably had an atmosphere very similar to that of the Earth, both in physical properties and chemical composition. But because of global warming (caused by the greenhouse effect) the water vaporized and partially escaped from the planet, the atmosphere overheated and has stayed in this state trough the present.

Chemical element		**Fraction**
Carbon Dioxide	CO_2	96.5%
Nitrogen	N_2	3.5%
Sulfur Dioxide	SO_2	150 ppm
Argon	Ar	70 ppm
Water	H_2O	20 ppm
Carbon Monoxide	CO	17 ppm
Helium	He	12 ppm

Table 2.1: Chemical composition of Venus' atmosphere (de Pater and Lissauer, 2001)

The question remains of how much water was there. The measured ratio of deuterium and hydrogen (D:H) is much higher (~ 0.016) than on Earth (0.00015) (as shown e.g. by Donahue and Hodges, 1992). That could mean Venus may have once had a certain volume of surface water (where both D and H were contained) but this evaporated as the greenhouse effect intensified. Because of the lack of a magnetic field (see previous section) which protects the planet and its atmosphere from the solar-wind's high energies particles, the light isotopes of hydrogen were expelled to space and the D:H ratio increased. If this is the case, Venus had at least a few tenths of a percent of the Earth's hydrosphere.

On the other hand a second interpretation for this D/H measurement indicates the possibility that Venus' atmosphere is permanently supplied with hydrogen from some other source (Grinspoon, 1993). By studying the escape time of atmospheric particles the historic reservoir of water is doubted and a permanent outgassing from volcanoes or other internal sources is suggested. Possible connections to resurfacing event are also arising because of a supposed fractionation of subducted surface crust. Which of these theories is valid will be proven by future probes measuring precisely the surface chemical composition.

The atmosphere of Venus is very dense compared to that of Earth – the pressure at the surface reaches 92 bars and the density is 65 kg·m^{-3} (on Earth it is only 1.22 kg·m^{-3}). The chemical composition is similar to the Earth's atmosphere except that the dominant element is not nitrogen but carbon dioxide (which is the cause of the greenhouse effect) as is shown in Table 2.1 (e.g. Hunten et al., 1983). Clouds on Venus are made mostly of sulfuric acid and they help distribute the heat around the planet, and because of this the temperatures on both the day-side and the night-side are almost equal. As shown in Fig. 2.3 the main cloud layer lies approximately in 45 km above the surface and is about 15 km thick – above and below this the atmosphere is quite clear and just sparse haze is apparent. The clouds rain sulphuric acid but this does not reach the surface because the intense heat below the clouds evaporates the raindrops about 30 km above Venus.

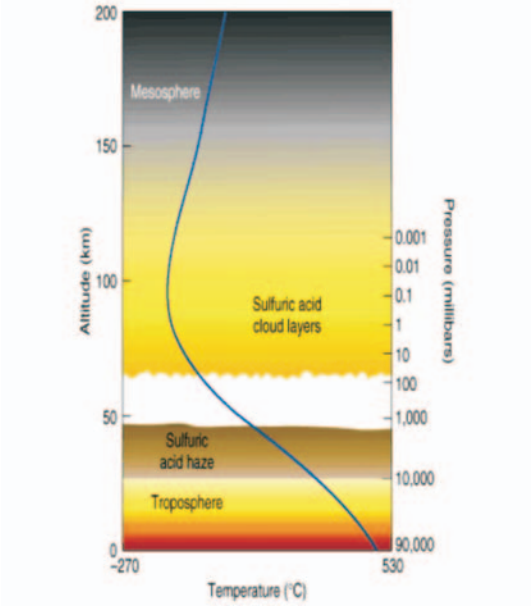

Figure 2.3: Structural and thermal profile of venusian atmosphere [i3]

The wind is very fast in the upper atmosphere (around 350 km·h^{-1}, almost 60 times faster than the rotation of the planet; this is called superrotation) but at the surface is quite slow (around 5 km·h^{-1}). All around the planet the wind direction is the same as the planet's rotation direction but it is slower closer to the poles, which gives the clouds a typical "V" pattern. At altitudes greater than 100 km the day-to-night atmospheric flow is observed.

During the Venera and Pioneer Venus missions plasma wave signatures similar to the ones on Earth caused by lightning (whistlers) were detected. But the question was if these signatures were of local origin (in the neighborhood of the space probes) or they were generated in the atmosphere of Venus. The latest observation made by the Cassini spacecraft during two close flybys in 1998 and 1999 failed to detect any high-frequency radio waves (spherics) also commonly connected to the lightning (Gurnett et al., 2001). But there still remains a possibility of an other lightning, e.g. from clouds to ionosphere – this produces slow discharges and such low-frequency radio signals that they are difficult to detect.

2.1.3 Surface

The surface of Venus has mainly an unimodal character and over 80% of it lies within ±1 km from planetary mean radius. Unimodality is characteristic for all terrestrial bodies in the Solar System except Earth where the topography is basically bimodal at levels of continents (+200 m) and sea-floor (−3500 m). A comparison of planetary modalities can be seen in Fig. 2.4 left – at right is a cumulative age distribution of surfaces.

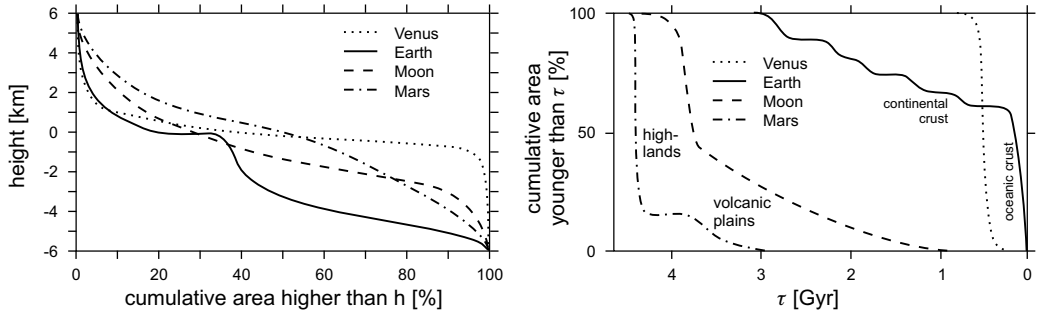

Figure 2.4: Modality and cumulative age distributions of terrestrial planet surfaces (both after Schubert et al., 2001)

Most of Venus' surface (Fig. 2.5) consists of relatively flat volcanic plains with several broad depressions and a few highlands. Everywhere on the surface we can see only a little erosion because of the absence of water and the slow wind at the surface. The dense atmosphere also prevents small meteors from impacting so only medium and large craters are observed.

The venusian highlands are 3-5 km above the average surface level – at the equator Aphrodite Terra (size of South America) and Beta Regio (smaller volcanic region), southern Alpha Regio and small Lada Terra. Close to the north pole of the planet is Australia-sized Ishtar Terra which shows several interesting features. Here, next to each other are located Maxwell Montes – the highest peak of Venus (10 km) – and several tectonic-like geological units. For these features some authors have proposed a crustal folding mechanism based on lithospheric stresses (e.g. Sandwell et al., 1997) whereas others favor as their cause dynamic-mantle topographic support, which could be a generating mechanism for both highlands (including local upwellings (Grimm and Philips, 1991) as well as downwellings

(Bindschadler et al., 1990)) and lowlands. There is no obvious evidence for ongoing or remanent plate tectonics similar to the subduction zones or large rifts located on Earth (e.g. Kaula, 1994). A possible reason for this could be the lack of water on Venus which enables the lithosphere to sustain larger stresses and so prevents the creation of plate tectonics (section 2.3). Thermal exchange between the planet and space is very efficient through plate tectonics and therefore an interior of the planet with a single-plate surface would slowly warm up (Nimmo, 2002). However we can find a lot of unusual topographic features on Venus (besides volcanoes – Fig. 2.6 – and craters – Fig. 2.7) like coronae and arachnoids (Fig. 2.8), chasmas (Fig. 2.9) and tesserae (Fig. 2.10) – some of which could be areas of local subduction. These together with signs of recent volcanic activity (lava channels – Fig. 2.11 – and domes – Fig. 2.12) show that Venus could still be an active planet. The surface itself (Fig. 2.13) is basically basaltic but more detailed geochemical research is needed in the future.

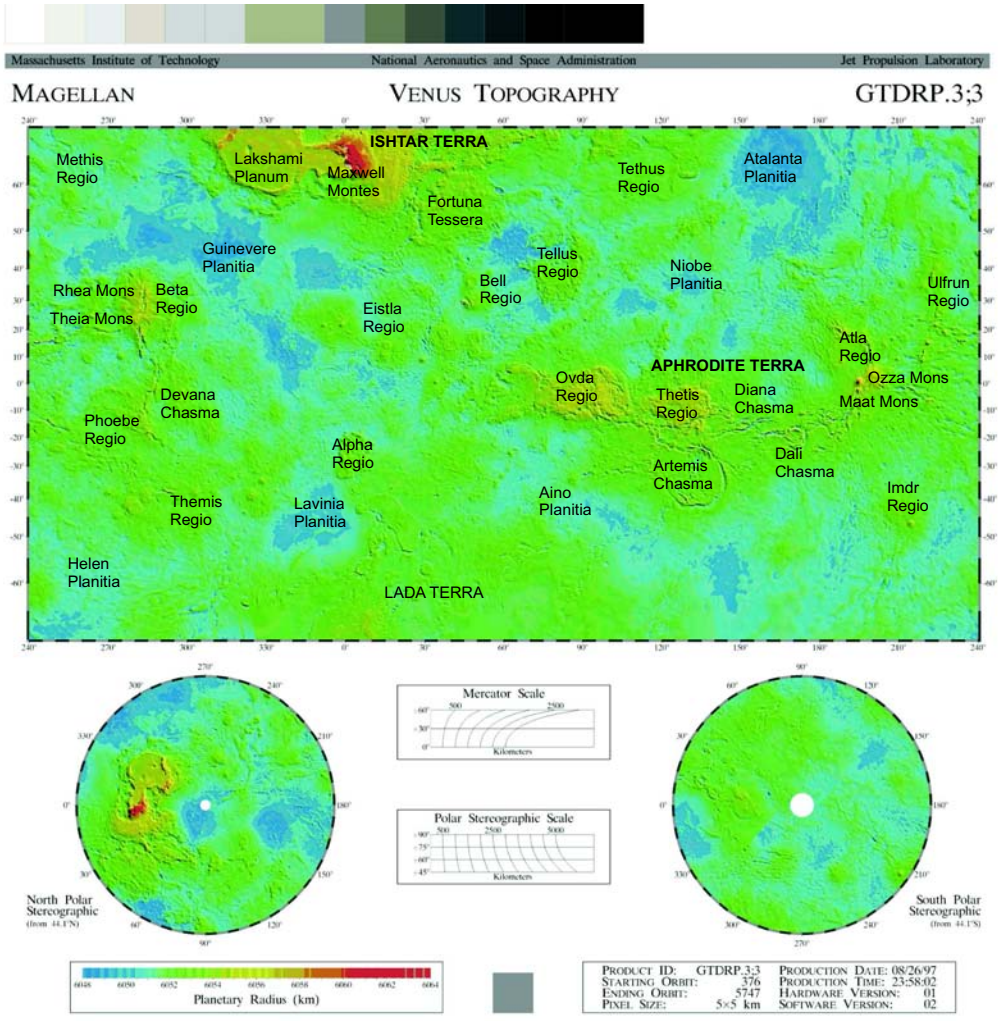

Figure 2.5: Topographic map of Venus based on the Magellan's observations [i3]

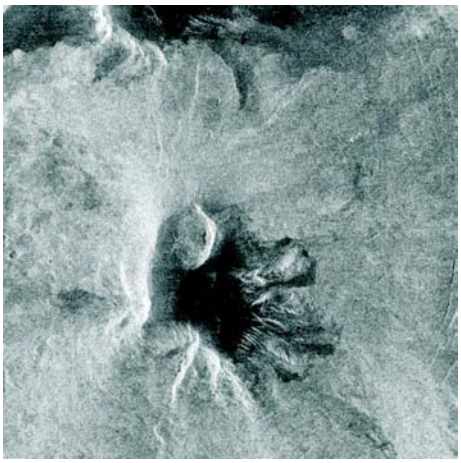

Figure 2.6: Magellan radar image of **Sapas Mons volcano** [i1]. On Venus there are several large shield volcanoes (similar to Hawaii or martian Olympus Mons) and many small ones which could be sources for the lava covering a large part of the surface. Recently announced findings indicate that Venus is still volcanically active, but only in a few locations – most of the surface has been rather quiet geologically since the resurfacing event

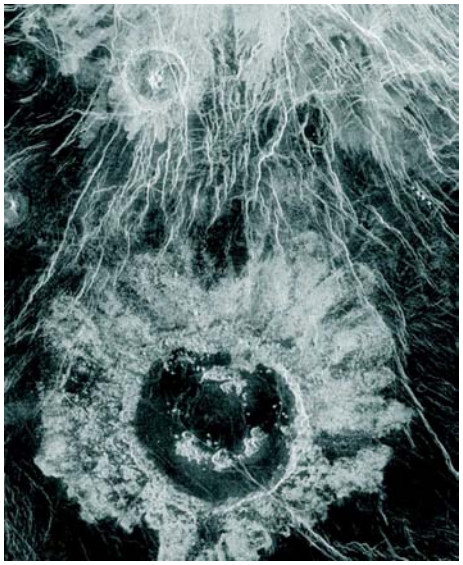

Figure 2.7: Magellan radar image of **Wheatley crater** [i1]. Craters at Venus are generally circular and sometimes surrounded by a rim formed mainly by meteorite impact. However we do not find the abundance of small craters as we do on the Moon or Mars because the small meteorites are destroyed during the flight through the dense atmosphere. But for the same reason we find there groups of craters – the dense atmosphere breaks the meteorites into smaller parts which impact around the same place

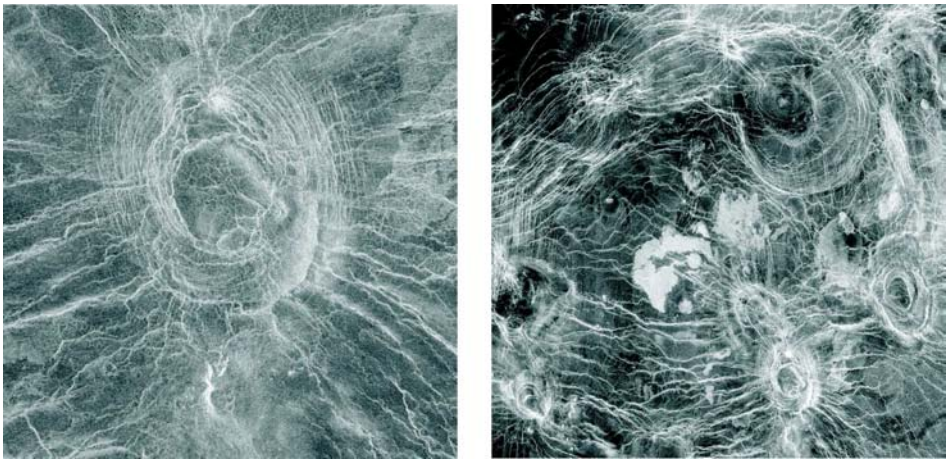

Figure 2.8: Magellan radar image of a **corona and arachnoids** [i4]. Coronae are circular surface features which are usually surrounded by several concentric ridges. We suppose that coronae are formed by hot spots in the mantle of Venus or by collapsed domes over large magma chambers. Arachnoids are smaller but similar to coronae, often clustered and with radial fractures and inter-fractures

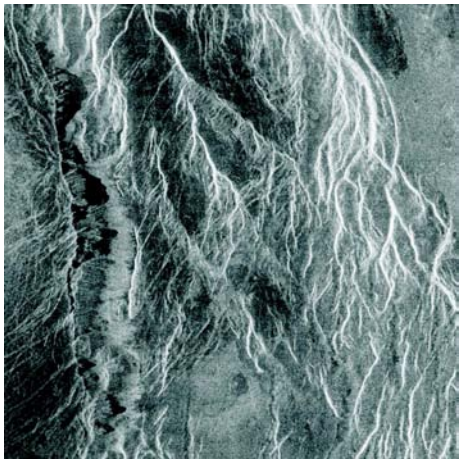

Figure 2.9: Magellan radar image of landslide debris in **Devana Chasma** [i1]. These formations and other similar features on the surface are basically deep valleys with often serpentine structure and are found mainly near volcanic or proposed-tectonic features. Often they are interpreted as signs of rifting however the originating mechanism is not yet fully understood

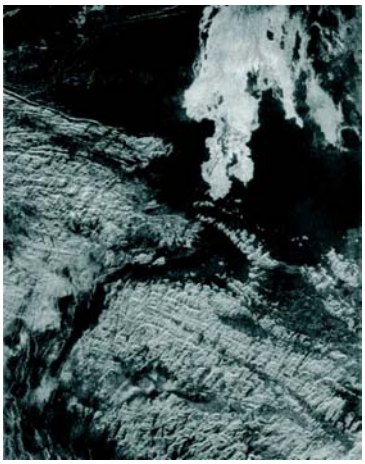

Figure 2.10: Magellan radar image of **tessera** in Eistla Regio [i1]. Tesserae are complex ridged terrains situated usually in the plateau highlands of Venus. They are quite unique because we suppose the mechanism of their origin is similar to the tectonic mountain-building processes on Earth, despite that today there are no signs of the plate tectonics on Venus. So this thickening and folding of the crust should originate through some other mechanism

Figure 2.11: Magellan radar image of a **channel** close to Fortuna Tessera near to Ishtar Terra [i1]. The origin of these channels is not clear however we can dismiss that they were formed by liquid water – the only possible fluid which could have caused them is a low-viscous lava. They can extent up to 1,000's km (much longer than similar ones on the Moon) and with widths 100's-1000's m. These features seem to be some of the most recent at the surface as they show no or little erosion and few superimposed craters

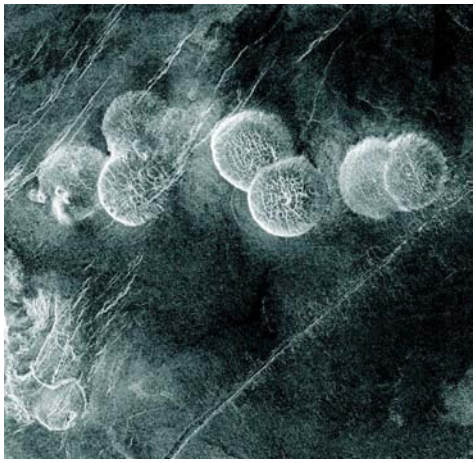

Figure 2.12: Circular **domes** on the eastern edge of Alpha Regio [i4]. These volcanic features seem to have an origin in eruptions of high viscous lava – they are often located near volcanoes or coronae which are both probably manifestations of ascending plumes. The domes have diameters up to 10's of km, steep sides and usually complex fracture patterns

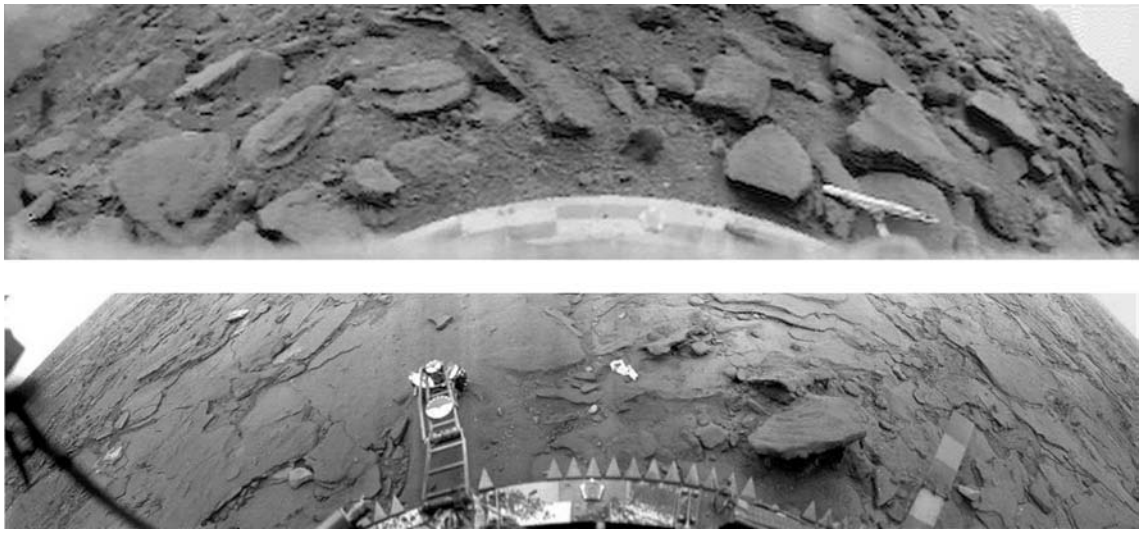

Figure 2.13: Pictures from Venera 9 and 14 (top and bottom respectively) which landed on the **surface of Venus** [i5]. The first panoramas from Venus were sent to Earth by the russian spacecraft Venera 7 in 1971. We notice the significant differences between the two landing sites – the first of them represents a tectonic site whereas the second one is typical of volcanic plains

2.1.4 Crust, Lithosphere and Mantle

There is not much information on venusian interior structure as we lack any seismic data from surface landing probes. Because of this we must estimate the mantle structure based on our knowledge of Earth and from the application of the appropriate scaling law.

The crustal and lithospheric thicknesses are derived usually from observed gravity signals and topography by means of gravimetric inversion combined with crustal isostasy and flexure. Many authors (e.g. Arkani-Hamed, 1996; Simons et al., 1997; Watts, 2001) put the bottom of the crust at the depth of between 15-50 km. However for the bottom of lithosphere the values differ much more – the estimates put the bottom of the lithosphere between 50-300 km but the elastic lithosphere seems to coincide with the crust (e.g. McKenzie, 1994; McKenzie and Nimmo, 1997). Some others (Simons et al., 1997), on the other hand, doubt our ability to discover the lithospheric thickness from data which we have presently – also from this point of view the information from upcoming missions to Venus might be crucial.

Just as the information we have on the subsurface is limited, our knowledge of mantle properties is very poor. However using knowledge of the Solar System's initial conditions and using thermal evolution models Stevenson et al., 1983 derived the depth of mantle to be 2900-3200 km. From a scaling law and knowledge of Earth the phase transitions (endothermic and exothermic) are assumed to be at depths of 440 and 740 km respectively (e.g. Schubert et al., 1997).

2.1.5 Core

As mentioned in Section 2.1.1 Venus does not possess an intrinsic magnetic field. That gives a strong condition on venusian core structure because we assume an internally generated field is produced by the thermal convection in the liquid, electrically-conductive part of core.

One possible explanation of this is that the core is completely frozen. In the time of the Solar System's formation the more volatile elements like sulfur were partially blown out from the Sun's neighborhood and so Venus' interior contains less iron sulfide than the Earth's one. This lighter alloy decreases melting temperatures and since the venusian interior conditions are not sufficient to melt the core, it could stay solid. However the observed venusian mean density is slightly less than Earth's (97% of Earth's density – e.g. de Pater and Lissauer, 2001) which contradicts the supposed smaller amount of these lighter materials in the core.

Another theory by Stevenson et al., 1983 states the possibility of a liquid core but with no convection. The slow rotation of Venus induces a Coriolis force great enough to keep the convection but the thermal gradient dropped down during the planet evolution and the magnetic field disappeared approximately 1.5 Ga. And because there is no solid inner-core the energy from phase transition (driving the thermal convection in Earth) is missing. This theory is supported by venusian Love number estimates which indicate that the core is liquid (Konopliv and Yoder, 1996). But as the planet cools it is possible that the solidification of the inner-core would happen (Fig. 2.14) and the magnetic field will be generated again.

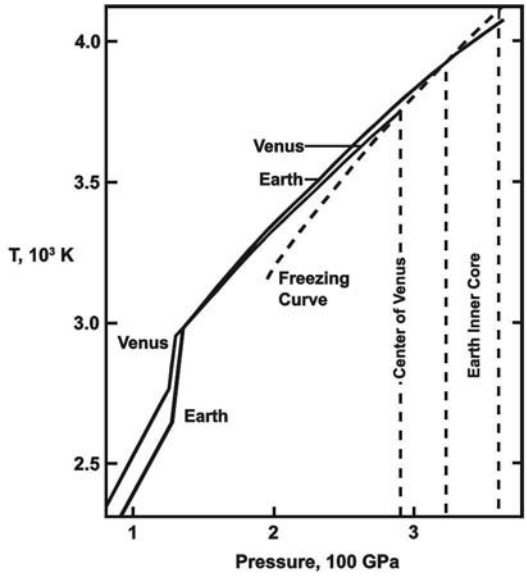

Figure 2.14: Possible formation and evolution conditions for cores of Venus and Earth (after Stevenson et al., 1983)

2.2 Evolution of Venus

Venus was formed during the accretion procedure of Solar system circa 4.5 Ga (giga-years i.e. billion years ago). Because of its proximity to the Sun a relatively major part of the volume is constituted by heavy elements (Fe, Si, Al etc.) with additional of volatiles (N, O, H_2O etc.) as in the case of Earth. From this comparative view most of our ideas about the evolution of Venus were originated.

In the beginning the planet was undifferentiated but the gravitational force and initial heat (from impacts and radioactive decay) caused the heavier elements to sink to the central part and the lighter ones to ascend to the surface. This process formed the core and also the initial mantle rheology – both of them then evolved as the primitive structure changed. The interior cooled and was chemically transformed and so the current state is a result of both the initial condition and planetary evolution.

2.2.1 Resurfacing Event Constraint

Even if we do not know the exact history of venusian evolution we can make judgements on it based on observed features. One of the most striking ones is the relatively low crater density observed by Magellan radar on the surface, as can be seen on comparison diagrams in Fig. 2.15. This means that any record of the craters older than approximately 500-750 Ma (Schaber et al., 1992; McKinnon et al., 1997) was erased by some global process and only the younger ones can be observed.

In any model of Venus' interior there must be a possibility of some unique event which changed the surface of the planet at a global level. The most suitable explanations is probably a resurfacing event which caused a subsidence of the existing surface (e.g. Turcotte, 1993) or covered it completely by material from volcanic eruptions material a relatively short period (e.g. Nimiki and Solomon, 1994). A possible mechanism for the first of them is a model of catastrophic lithosphere instability which could be a result of a lithosphere-thickening process connected with a single-plate tectonics. For the second, authors speculate about a periodical convective style, which once per period longer than 500 My, causes enormous volcanic activity. Of course the possibility of plate tectonics and volcanic suspension is an alternative which we can not deny. In all cases the most important factor could be the lack of water which had a major influence on the mantle rheology – the drier subsurface structure could be also the reason for the single-plate tectonics.

2.2.2 Heat Transport Models

It is very important is to fully understand the heat transport process. In the case of Earth about 70% of the internally generated heat is transferred by subduction of cold lithospheric slabs and by production of a new and hot oceanic crust at the middle-oceanic ridges. Other minor contributions are by ascending hot-spot, lithospheric delamination and secondary convection. However in the case of Venus we observe no plate tectonics and so the heat transfer must be done by some other means. There are generally three possible ways (see review in Schubert et al., 2001): the uniformitarian model (with constant heat flux and stable internal conditions), the catastrophic model (the heat flux is not in balance with heat generated and stored in the planet) and the differentiated-planet model (all heat producing elements are concentrated in the crust).

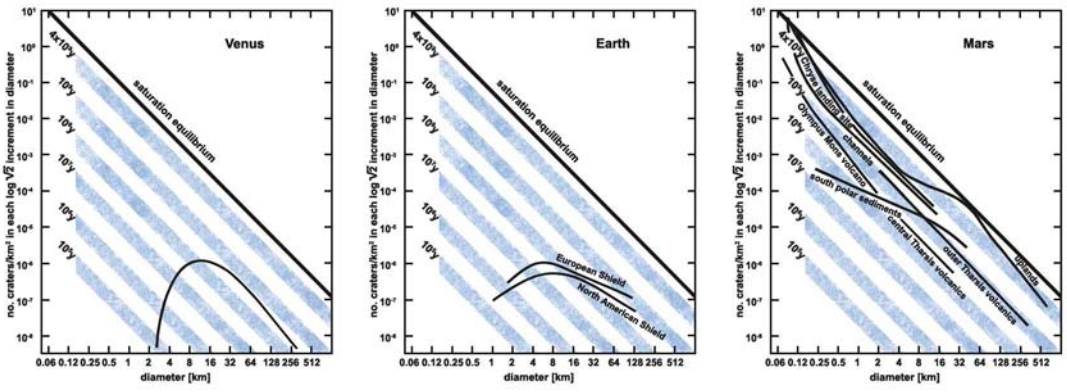

Figure 2.15: Crater density statistics for three well explored objects of the Solar System – the planets Venus, Earth and Mars. For Venus and Earth we see (except for the protective influence of atmosphere on small-size meteor penetrations) a certain degree of erosion but for Mars there are parts of the surface saturated with almost no erosion (after de Pater and Lissauer, 2001)

2.2.3 Convection Models

The very efficient means of cooling the deep planetary interior is the subsolidus mantle convection. This process controls not only the evolution of Earth (where it is demonstrated by plate motions) but also the thermal and chemical structure of other terrestrial planets and moons (SCHUBERT, 1979; SCHUBERT ET AL. 1986) where the manifestation is merely indirect, through surface volcanic and tectonic features. From our knowledge of Earth and presumed initial structure of Venus there is a general agreement that this planet is probably still active. Therefore through modelling of mantle convection we obtain important insights into the physics of Venus as well as its evolutionary history.

Several numerical studies of convection in the venusian mantle have been carried out – both for Cartesian (e.g. STEINBACH AND YUEN, 1992) and for 3D spherical geometry (e.g. SCHUBERT ET AL., 1997). The results show that the parameters of the model have a significant influence on the convection pattern, degree of layering, state of mixing and long-time behavior of convection – an example of the importance of an increase in viscosity is given in Fig. 2.16. Aside of this the importance of upper boundary condition is considered – whether the rigid or free upper boundary (stagnant, sluggish or mobile lid) is the case for Venus. If great importance in the mantle behavior is a Rayleigh number, which controls the nature of convection (e.g. RATCLIFF ET AL., 1997) in all the parametrization – for more detailed explanation see an extensive review on this theme in SCHUBERT ET AL., 2001.

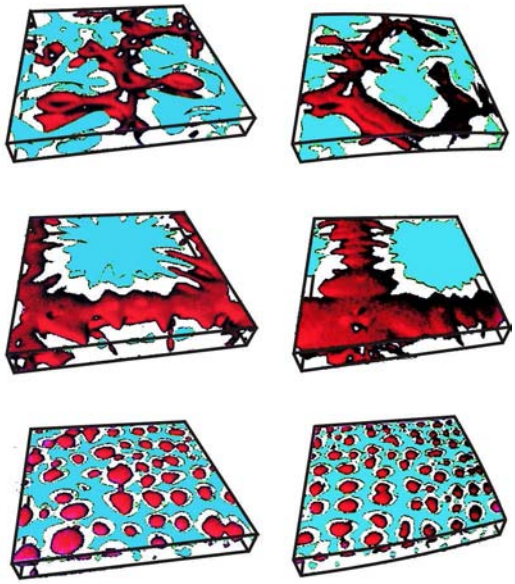

Figure 2.16: Convection models for Cartesian box $8 \times 8 \times 1$ with temperature-dependent viscosity and fixed Rayleigh number – from left to right and up to down we have viscosity contrasts: 10^0, 10^1, 10^2, 10^3, 10^4 and 10^5 respectively (redrawn from SCHUBERT ET AL., 2001). From comparison with observed dynamic features on the surface of Venus we can deal with viscosity models a)-d) and reject e)-f) for its small scale character

But another approach to the study the venusian mantle dynamics is also possible – because of the assumption, mentioned several times already, that Venus' topography and geoid are manifestations of interior dynamic processes we can include the gravity, topography and admittance as constraints for quantitative mantle convection. From such global models (e.g. KIEFER ET AL., 1986) we obtain surprisingly good agreement with observed values for even very simple parametrizations. Also from these studies come our current estimates of viscosity structure and mantle rheology – see the discussion in Chapter 7. A similar technique could be used also on the regional scale for those major surface features with strong gravity signals e.g. venusian equatorial highlands (KIEFER AND HAGER, 1991) or large volcanoes (KIEFER AND HAGER, 1992) but with the limitation that the obtained results may not represent the global characteristics. On the other hand the large percentage of explained observed data allows us to use these forward problems results to consider the venusian mantle as still being active, with similar structure to Earth, except for the existence of an asthenosphere and with a stiff lithosphere on top.

2.3 Quest for Water

As has been mentioned several times throughout the text the key question for understanding Venus is how much water it originally had and where it has gone. When we know the answer to this question we can assume more clearly the ongoing geophysical processes within the venusian interior and also the evolution of its climate conditions. Mainly the convection style problem and mantle rheology are tightly connected to the water budget in the minerals and these could have a significant influence on the resurfacing event.

Our only means of studying these problems are through studying surface mineralogic composition or atmospheric element ratios. Unfortunately the first is limited to the data from russian Venera missions and has not given us satisfactory answers. As our only other option the second possibility strongly depends on exact measurements not only of the element composition of the atmosphere but also of the escape-time from the atmosphere into space. This problem is already mentioned in Section 2.1.2 where the possible explanations for the current hydrogen and deuterium contents are also noted. However to decide if the D/H ratio is a sign of relatively late outgassing or a residual sign of original water reservoirs we need to have exact measurements of H escape flux (DONAHUE, 1999). Because these vary in the order of magnitude (7×10^6 - 3×10^7 $cm^{-2} \cdot s^{-1}$) the originating water could may have evaporated from the surface anytime from 500 Ma to 4 Ga. To decide whether Venus had an ocean or not we have to improve the sensitivity of our measurements.

2.4 Comparison with Earth

As mentioned above Venus is in many ways similar to Earth. In Table 2.2 some of the physical parameters and ratios of both planets are shown for comparison. The first three orbital parameters are directly connected to Venus' position in the Solar System, the other parameters probably to the evolution.

planetary parameters	**Venus**	**Earth**	**ratio**
mean distance from Sun	108 mil. km	150 mil. km	0.72
orbital period	225 day	365 days	0.66
orbital velocity	35 km·s^{-1}	30 km·s^{-1}	1.18
rotational axis inclination	177.4 °	23.5 °	–
rotational period	243 days	1 day	243
mass of planet	4.87×10^{24} kg	5.98×10^{24} kg	0.95
fraction of atmosphere to total mass	$\sim 10^{-4}$	$\sim 10^{-6}$	100
mean density	5.24 g·cm^{-3}	5.52 g·cm^{-3}	0.95
mean gravitational acceleration	8.89 m·s^{-2}	9.81 m·s^{-2}	0.91
escape velocity	10.36 m·s^{-1}	11.2 m·s^{-1}	0.93
albedo (reflexivity)	0.65	0.37	1.76
temperature interval	+446 to +482 °C	−88 to +58 °C	–
number of moons	0	1	–

Table 2.2: Comparison of Earth and Venus (after de Pater and Lissauer, 2001)

According to the latest celestial mechanics studies the orbits of terrestrial planets are very stable over astronomical short period. But over longer periods they can become chaotic and thus unpredictable because of weak but random-like gravitational impulses from other Solar System objects. The Ljapunov exponent of orbital decay in the case of Venus is approximately 50 My^{-1} (de Pater and Lissauer, 2001) so after this time the orbit changes distinguishably. But from similar studies done on Earth it is known that the group of possible orbits is quite narrow and so the changes in the insolence (important for temperature trend) are not significant.

Chapter 3

Data Sets

In the previous chapter we saw the importance of exact measurements of topography and gravity for the understanding of internal structure and processes in the mantle when we miss any seismic data. Unfortunately such data coverage is available only for a few terrestrial bodies (Venus, Earth, Moon, Mars) because a probe on stable orbit for a relatively long period is needed. For the other planets and moons we have just flybys (Mariner 10 around Mercury, Galileo around Jovian moons) which are not sufficient for the construction of global models.

The planetary topography is measured usually by laser altimetry whereas the gravity must be derived from the Doppler shift of radio signals received on Earth. These raw data could be easily converted to the spherical harmonic (SH) model – the spectral approach has several advantages so even the topography is used to transform to the SH model. But because of coefficient normalization by planetary parameters (Kaula, 1966; see Appendix A) proper knowledge of these parameters is needed. In Table 3.1 their values are listed – but as any data from the space missions their values could be re-set again in the future. However, throughout this work we will be dealing SH coefficients with no normalization.

	$\mathbf{GM[km^3 \cdot s^{-2}]}$	**radius[km]**	$\mathbf{g_0[m \cdot s^{-2}]}$
Venus	324,858.592	6,051	8.89
Earth	398,600.442	6,371	9.81
Moon	4,902.801	1,738	1.62
Mars	42,828.372	3,396	3.72

Table 3.1: Planetary parameters for SH coefficients normalization [i4]

One of the reasons for the use of SH models is to see the power of topography or the geoid on different scales – from this we can assume certain implications about the internal structure of planet. However these spectral methods have of course global characteristics and therefore they are unsuitable for the investigation of individual features on a local scale.

3.1 Spherical Harmonic Models for Venus

Both venusian geoid and topography models are known from orbital measurements made by the spacecrafts Pioneer 12 Venus Orbiter (1978–1993) and Magellan (1990–1994). The latter data sets from Magellan are much more accurate and so we have used them in our investigation. However because of a strong coupling between the present topography model and new gravity measurements and vice versa there is still a chance for future improvements. The SH coefficients were downloaded from Geophysical Node of Planetary Data System [i4].

3.1.1 Geoid model MGNP180U

The model of Venus' geoid was derived from Doppler tracking of the Magellan orbiter in form of line-of-sight (LOS) acceleration measurements. All aerodynamic processes were modelled so the gravity acceleration could be read from the Doppler shift of two-way radio communication and converted into a geoid model (Konopliv et al., 1999). The first three orbital cycles (1 cycle $\sim$ 243 days) of the Magellan mission were used just for preliminary models. The collection of data began with cycle 4 and continued until the loss of the spacecraft late in 1994. Using an equation A.30 we can convert measured quantities to a gravitational potential – this then gives us then the geoid as is shown in Fig. 3.2.

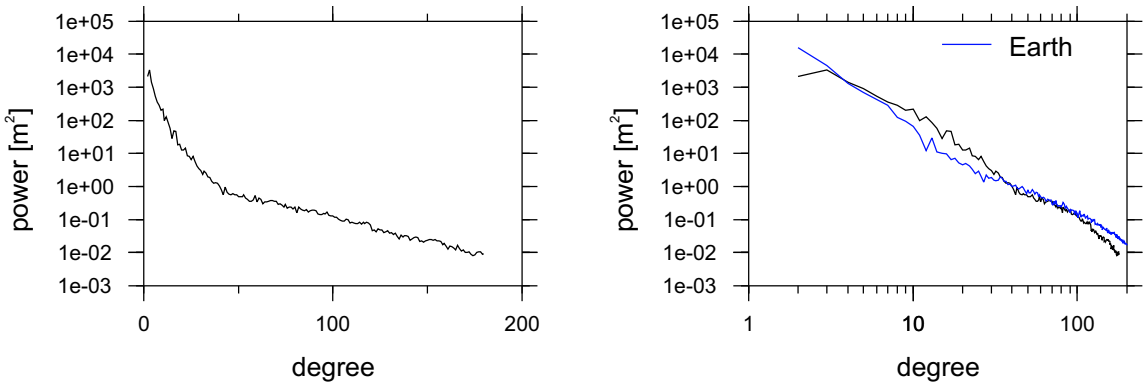

Figure 3.1: Power spectrum of the venusian geoid displayed an a linear and logarithmic scale compared with Earth geoid power spectrum (using equation A.12)

3.1.2 Topography model GTDR.3

During the Magellan mission orbital cycles 4, 5 and 6 4,284,578 measurements by its laser altimetry device were obtained, and so the entire surface was covered in great detail several times. The radial position of surface elements was determined based on gravity models obtained from previous maneuvering of the Magellan itself (see section above). The map in Fig. 3.3 shows 0.25° resolution of topography in equidistant projection – the corresponding SH model (Rappaport et al., 1999) was completed up to the degree and order 360.

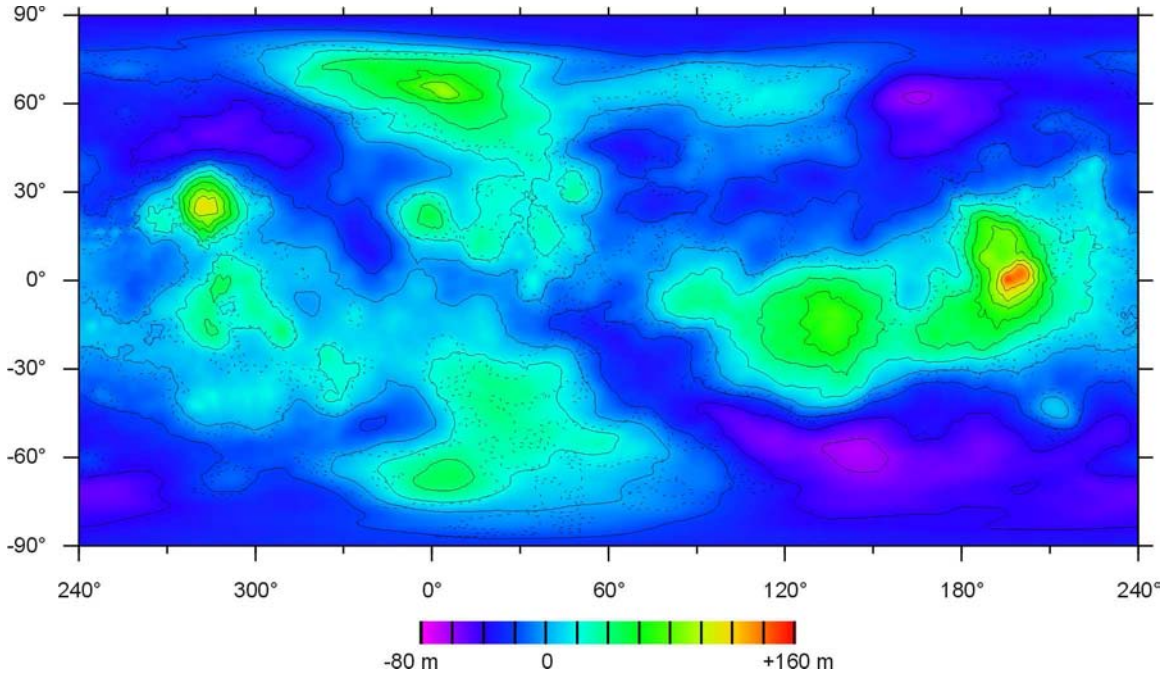

Figure 3.2: Model MGNP180U of the venusian geoid. The dashed line marks the zero-level topography contours

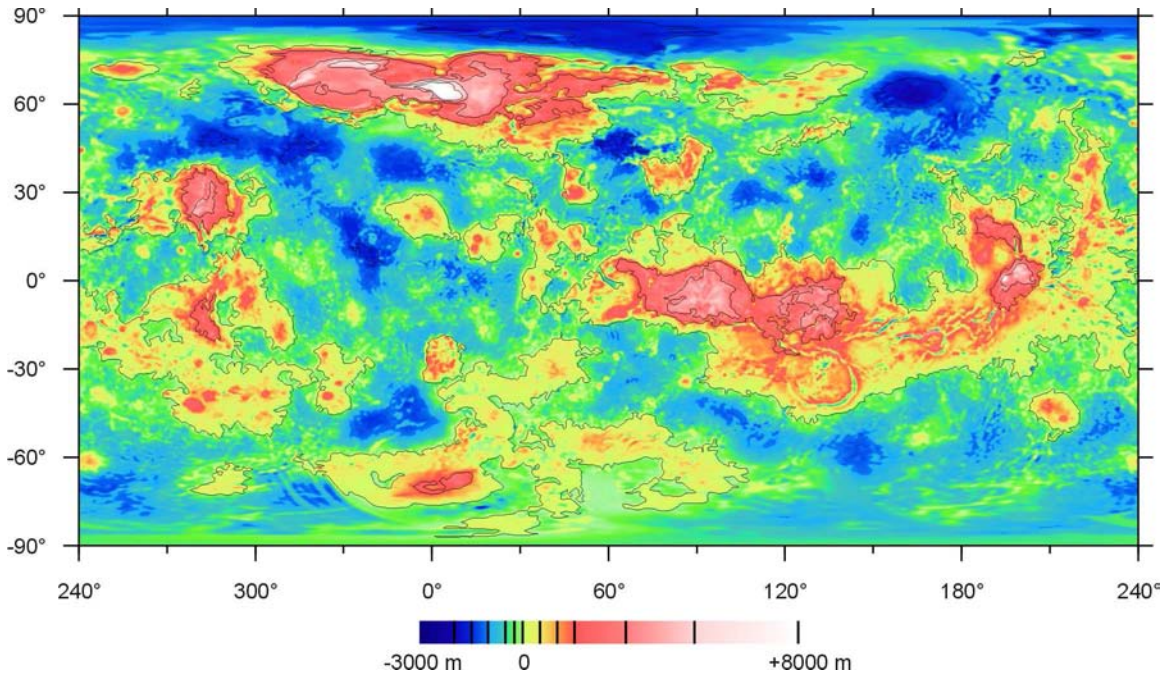

Figure 3.3: Model GTDR3.2 of venusian topography

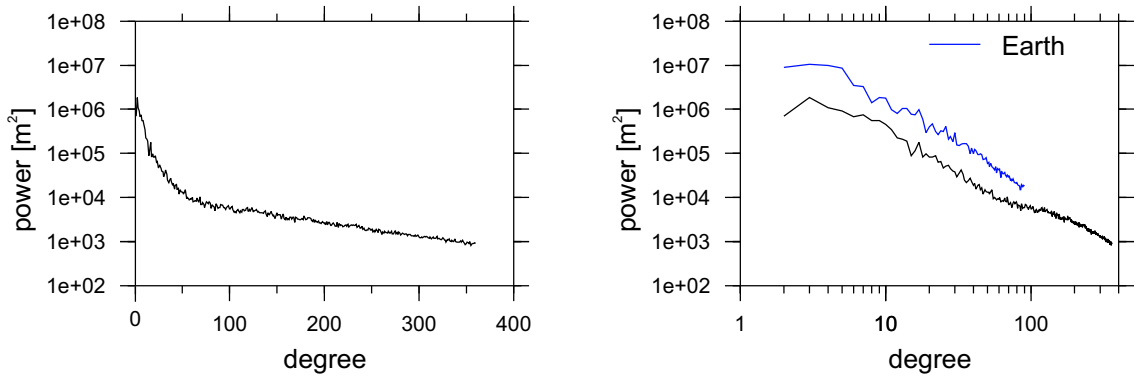

Figure 3.4: Power spectrum of the venusian topography displayed in linear and logarithmic scale compared with Earth topography power spectrum

The mean planetary radius was defined with new precision as 6,051,881 m and the planetary flattering of Venus as 9.75×10^{-5}. New calculations were also done for center-of-figure offset from center-of-mass and it was found lying beneath the north-west corner of Thetis Regio in Afrodite Terra with the radius of offset $r_f = 186.5$ m. This position is caused mainly by equatorial highlands which, given their non-uniform distribution mainly around the equator, mark an accumulation of the surface mass. However when compared to Earth's topography Venus' is generally much flatter, which is obvious also in the power spectra comparison diagram in Fig. 3.4. This could again corresponds to the overall character of the venusian surface (see Section 2.1.3) and our assumption that a large part of it represents the

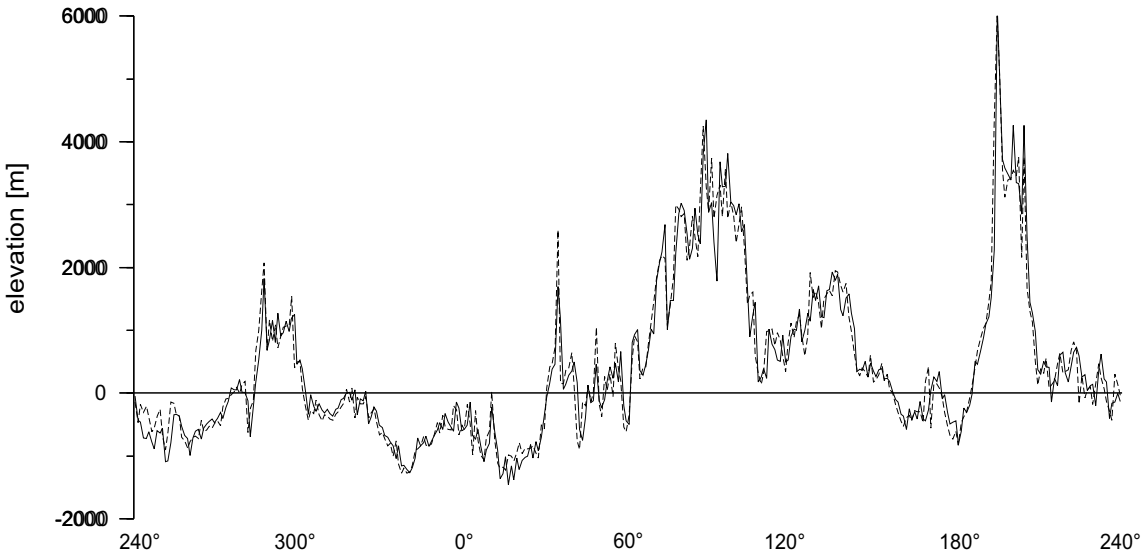

Figure 3.5: Displacement of digital and spherical harmonic models of venusian equatorial topography with respect to the reference radius (after Rappaport et al., 1999)

dynamic topography which has to have much smaller amplitudes (e.g. SCHUBERT ET AL., 2001) than a plate-tectonics one, with its existence of continents, sea-floor with subduction zones and plate-collisions areas inducing high mountain-chains of tectonic origin.

As mentioned above this latest spherical harmonic model of venusian topography is evaluated up to degree and order 360. It shows a generally higher degree of correlation with the geoid – in comparison to previous models – over the entire spectral interval and also for short wavelengths in spatial domain (KONOPLIV ET AL., 1999) and so enables us to investigate surface features of a smaller scale ($\sim$ 10's km) objects like coronae or volcanic domes. In Fig. 3.5 the misfit between the spherical harmonic model and the real digital altimetry on the equator is displayed (please note 2500$\times$ vertical exaggeration). However *a priori* constraint of using the Kaula's rule of thumb for higher degrees of geoid model (KONOPLIV ET AL., 1999) is a reason for the decreasing of correlation coefficient (Fig. 3.6 left) and for change of the admittance function character (Fig. 3.6 right) for degrees $j > 100$. Therefore we will use in our calculations both models truncated at $j = 90$ which guarantees the certain independence of data sets.

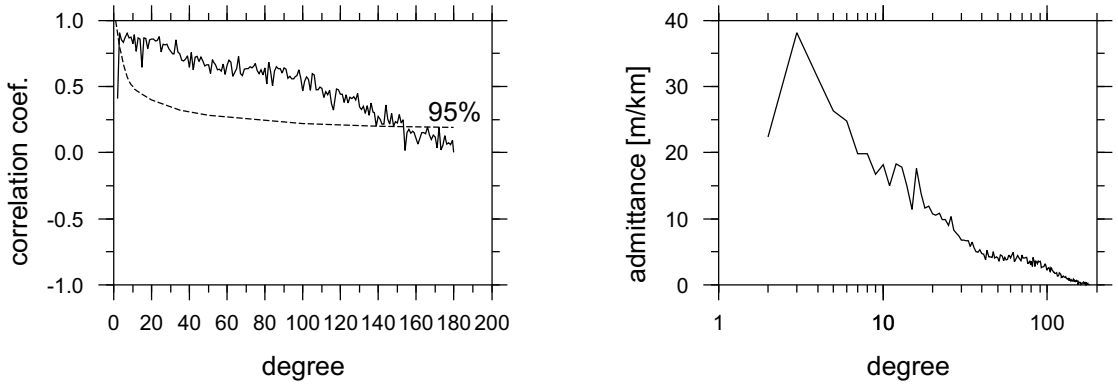

Figure 3.6: The degree correlation between Venus' geoid and topography (A.13 – the dashed line marks a 95% level of confidence) and degree admittance (A.15)

The key question however is how the topographic load is supported. In following two chapters we will apply different approaches to answer this question and by used methods then predict the venusian geoid. By comparison of the observed data and the predicted values we can find out properties of the venusian subsurface.

3.2 Spherical Harmonic Models for Other Planets

As we are enhancing our knowledge of the Solar System with automatic space probes mapping individual planets and moons we are still strongly pushed to look for the parallels between these bodies and our own planet Earth. Unfortunately the progress is complicated and several missions to a planet are needed to obtain reliable data with sufficient resolution. Some basic gravity and topographic data for Earth, Moon and Mars are shown to under-

lay wider planetological considerations which could help us not only in planetary research but also back in the Earth sciences. The data used (SH coefficients or grided values) were obtained from [i4] for Moon and Mars whereas those for the Earth from [i6] and [i7].

In Fig. 3.7 are the observed geoid and topography of Earth together with the power spectra and their correlation. The purpose of showing these diagrams is to offer a chance to compare it with other terrestrial planets – e.g. the correlation diagrams show important global-scale difference in the nature of planets. This is especially the case when compared to Venus, where the correlation coefficient for $j > 2$ is above 95% level of confidence. Another interesting feature is the bipolar structure of the geoid which is, in the case of Earth, interpreted as a manifestation of D" heterogeneity reservoirs connected with mantle upwelling (e.g. Forte and Mitrovica, 2001) but is similar to a martian geoid dominated by the Tharsis region and Utopia Planitia (which is by some – e.g. Harder and Christensen, 1996 – presumed to be a remanent sign of single-cell convection in the mantle).

Despite the fact that the Moon is our closest space neighbor we had to wait until 1990's to obtain more detailed information – the Clementine (1994) and then Lunar Prospector (1998–1999) missions provided us the global gravity and topography data. Recent gravity models have been completed up to the degree and order 165 (Konopliv et al., 2001) but with the handicap of no direct information from the far-side which limits the information on wavelengths $l > 110$ and needs a strong *a priori* constraint. From laser altimetry several topographic models were completed – here we use the model up to degree and order 90 (Smith et al., 1997) however truncated at $j = 70$ because of the coverage gaps in the polar regions. In the close future a major advance in lunar research is expected so these both problems should soon be solved and complete SH models up to a higher degree will be available. Analyzing these fields (Fig. 3.8) we can immediately observe the most striking features in the lunar geoid: so-called mascons (**mas**s **con**centrations). Most of these strong gravity peaks are located in large Mares or craters where the topographic minima are and most probably originate in some subsurface mass anomalies.

In the case of Mars the main contribution to our knowledge of the planet came from mission Mars Global Surveyor (1997-until now). This spacecraft's altimetry device produced a global topography model (Smith et al., 1999) with better precision than we have for many locations on Earth. However the current model of martian geoid GMM-2B (Lemoine et al., 2001) is only up to the degree and order 90 and in the short wavelengths a strong "contamination effect" is observed – see Fig. 3.9. Because of this basic problem the scientific community is impatiently awaiting the results from new missions, namely from the european Mars Express which has been in a polar orbit around Mars since 2003. The new results will then be used to better determine the crustal properties (of which the global distribution is already know from gravimetric inversions done recently by Zuber et al., 2000) and parameters of the lithosphere and mantle which are connected to planetary evolution.

In the future the automatic spacecrafts will explore for us the planet Mercury, the largest bodies of the asteroid belt and the Jovian moons. From these data we will hopefully uncover more on the Solar System's formation, terrestrial planet evolution and possibly also on icy-moon structure. The latter is crucial both for planetary sciences and for exobiology as we assume there are water oceans under the icy-crusts (Spohn and Schubert, 2003).

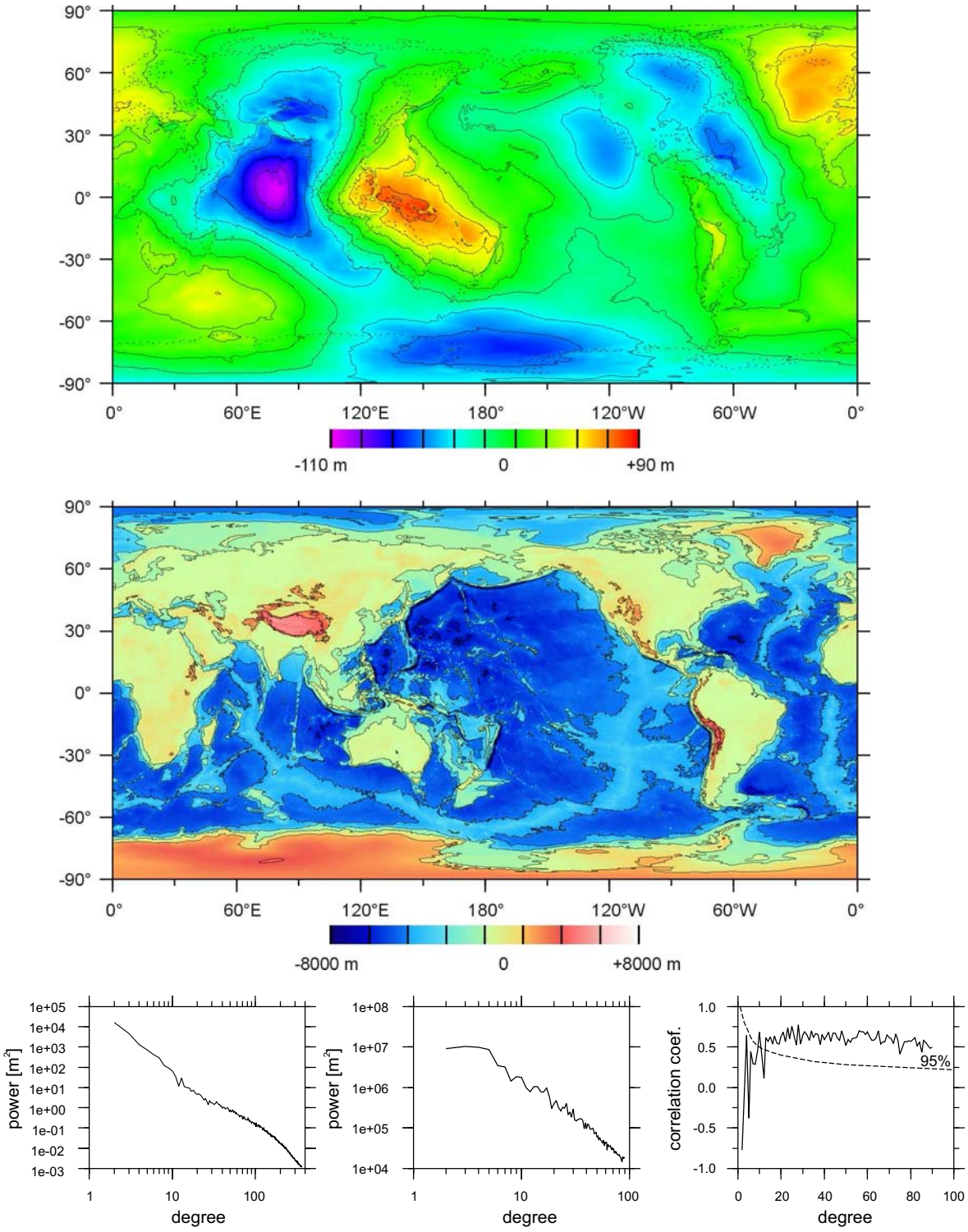

Figure 3.7: Earth's geoid (top) and topography (middle) together with their power spectra and the correlation between observed geoid and topography

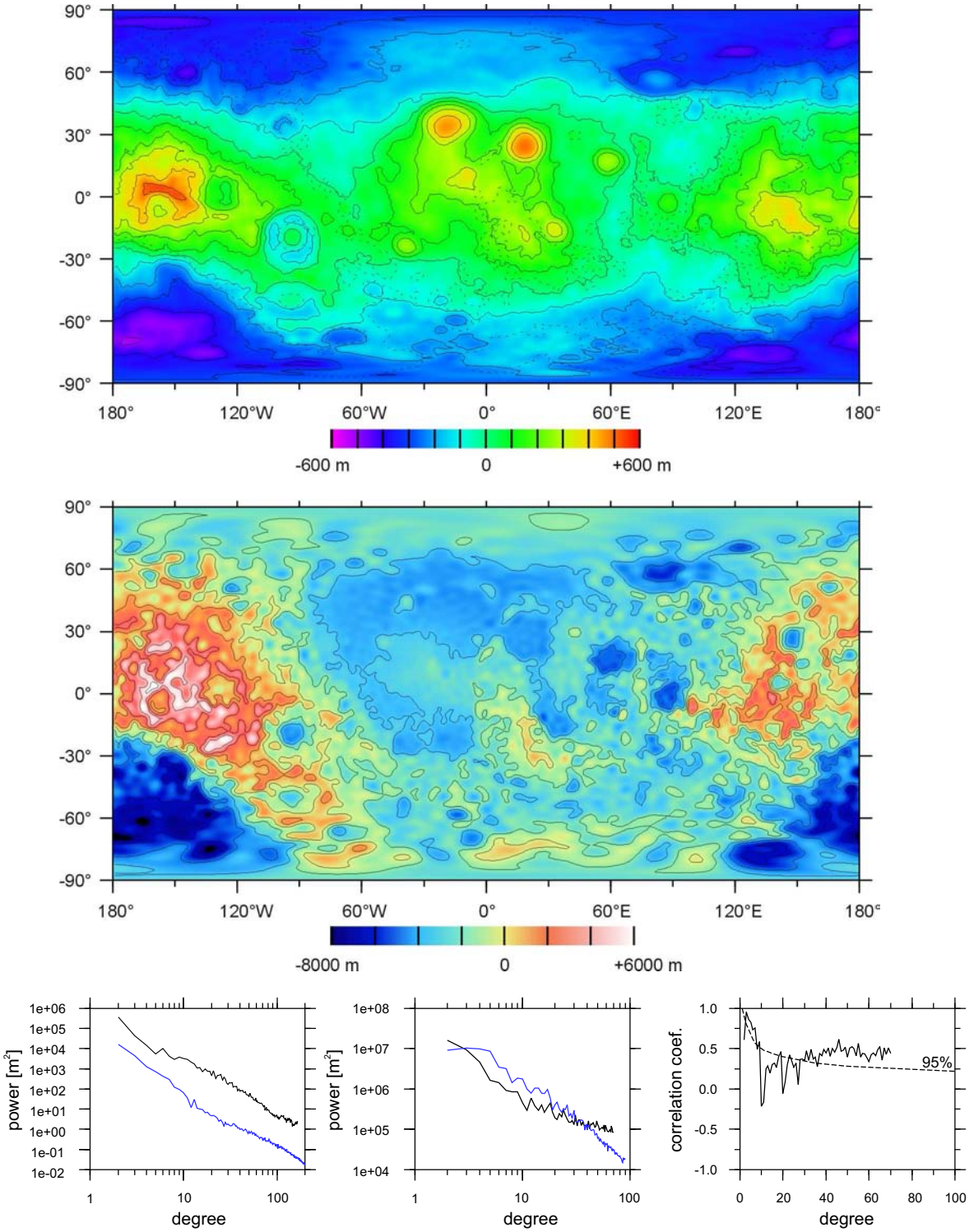

Figure 3.8: Lunar geoid (top) and topography (middle) together with their power spectra (compared to Earth – blue lines) and the correlation between observed geoid and topography

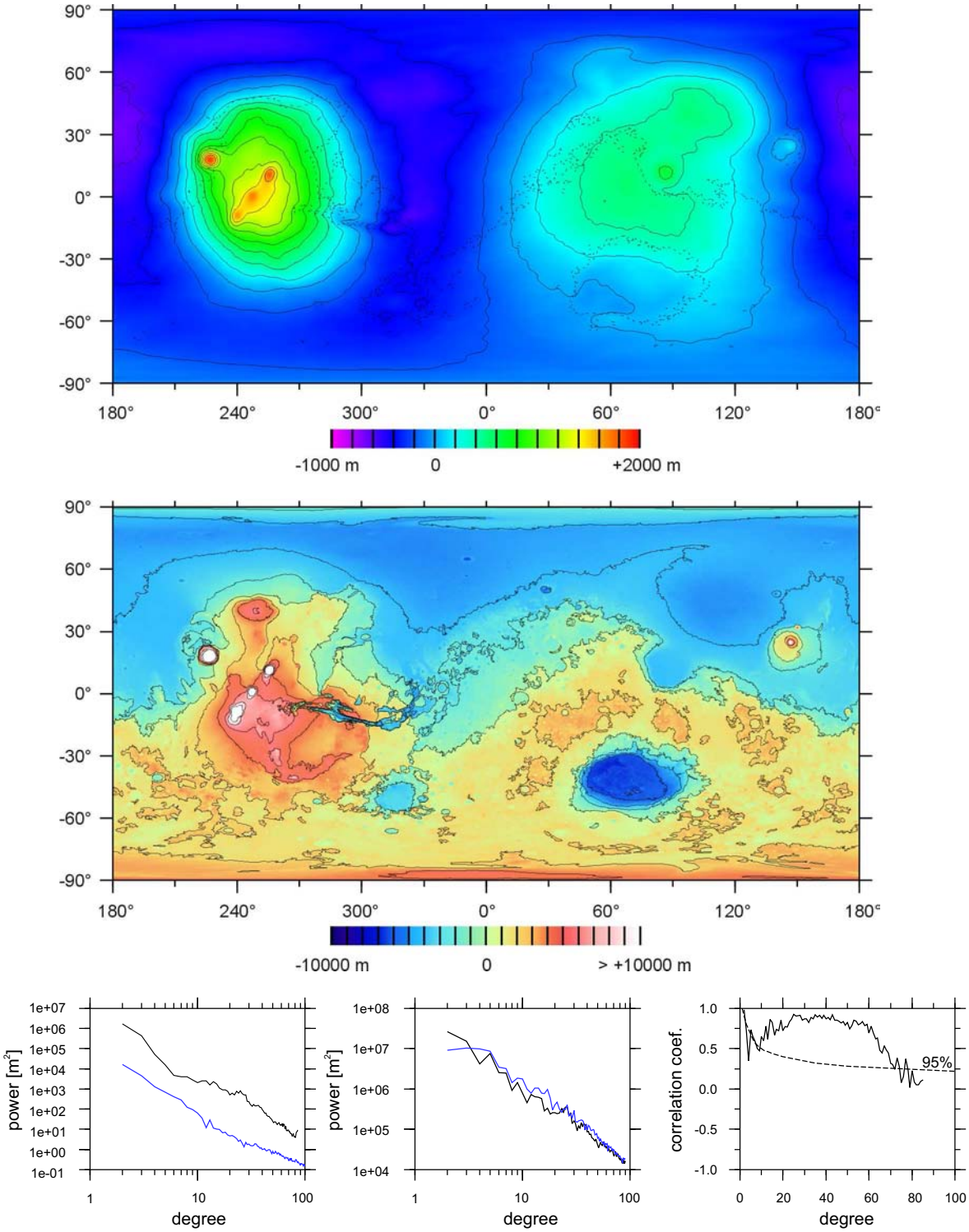

Figure 3.9: Martian geoid (top) and topography (middle) together with their power spectra (compared to Earth – blue lines) and the correlation between observed geoid and topography

Chapter 4

Isostasy and Crustal Structure

In Chapter 3 we saw in the correlation and admittance diagrams, that the key point in understanding the mechanisms producing the topography is an interpretation of the accompanying geoid. With Venus this is well correlated to the topography, hence the easiest explanation based on steady-state processes is acceptable. If these predict the observed data with high accuracy the current status of Venus may be explained by already ceased dynamic mantle processes and the heat flux removed from the planet through a thermal conduction.

4.1 Uncompensated Topography

Any model of the venusian geoid based on steady-state processes should contain the contribution of an uncompensated topography – this case is described by the equation A.26. However, comparing the observed and predicted power spectra (Fig. 4.1) we see that such a model predicts a geoid with a power spectrum of two orders of magnitude higher than the observed data.

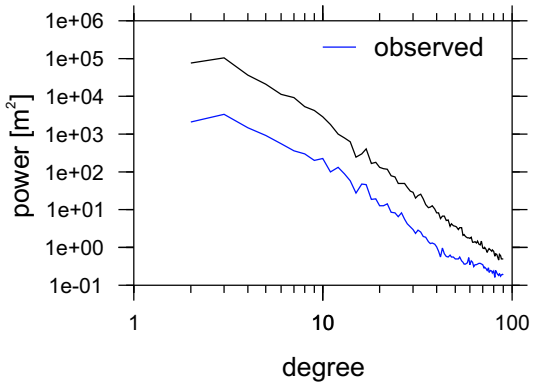

Figure 4.1: Power spectrum of geoid induced by the uncompensated topography compared with the power spectrum of the observed geoid

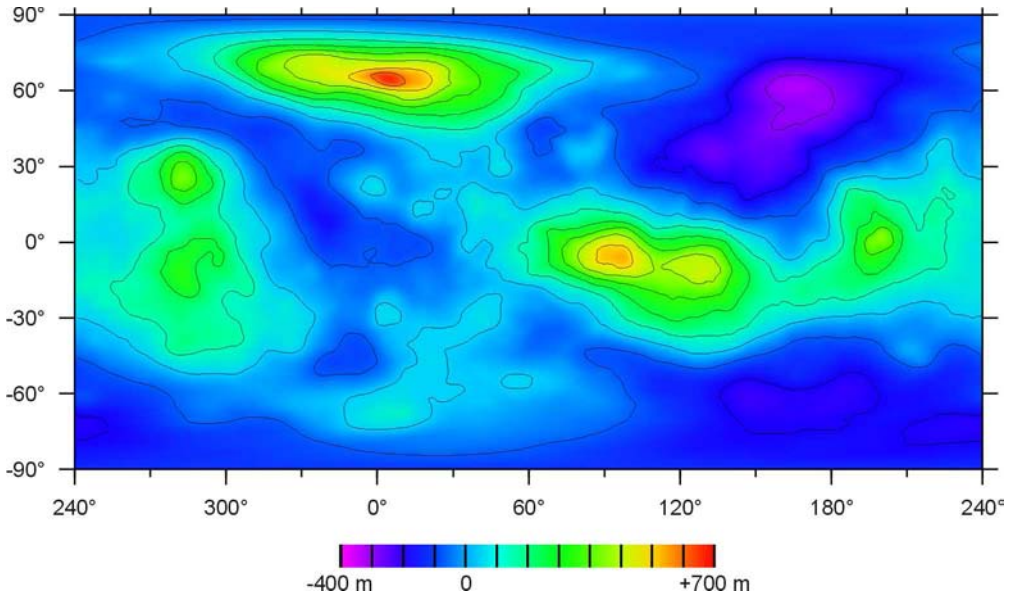

Figure 4.2: Geoid induced by venusian uncompensated topography

From analysis of the predicted power spectrum we can reject the hypothesis of uncompensated topography. Nevertheless it is worthy to also examine the spatial expansion of the obtained SH model. As seen in Fig. 4.2 we obtained a geoid with amplitudes one order of magnitude higher than the observed data. The major features of this model are also not well correlated with the observed ones as could be seen in comparison with Fig. 3.2 at page 29 (e.g. a high signal at Aphrodite Terra but instead of a major peak in Atla Regio this is quite low and higher signals are located in Ovda Regio – Maxwell Montes in Istar Terra became the highest peak on the planet). Because of these reasons we have to look for some other geoid generating mechanism.

4.2 Isostatic Compensation of Topography

To diminish the topographical contribution to the geoid we can employ the principle of isostatic compensation to our model. For our purpose we adopt a simple scheme of a homogeneous crust with density $\rho = 2{,}900$ kg·m^{-3} (e.g. Rappaport et al., 1999). To satisfy a principle of isostasy we prescribe on the bottom of the crust a topography which is an inverse of the surface and having amplitudes multiplied by the ratio $\frac{\rho_{surf}}{\Delta\rho_{moho}}$. We cannot determine the density contrast at the bottom of the crust ρ_{moho}, but when we are only dealing with the geoid contribution from this boundary, the amplitude of it cancels this term and we obtain the equation A.28 which is independent from it.

First we look for a single apparent depth of compensation (ADC) in the whole spectral interval j=2-90 (which is not severely biased by *a priori* constraint). We vary the parameter of the compensation depth in the interval 1-500 km and for every depth we calculate the

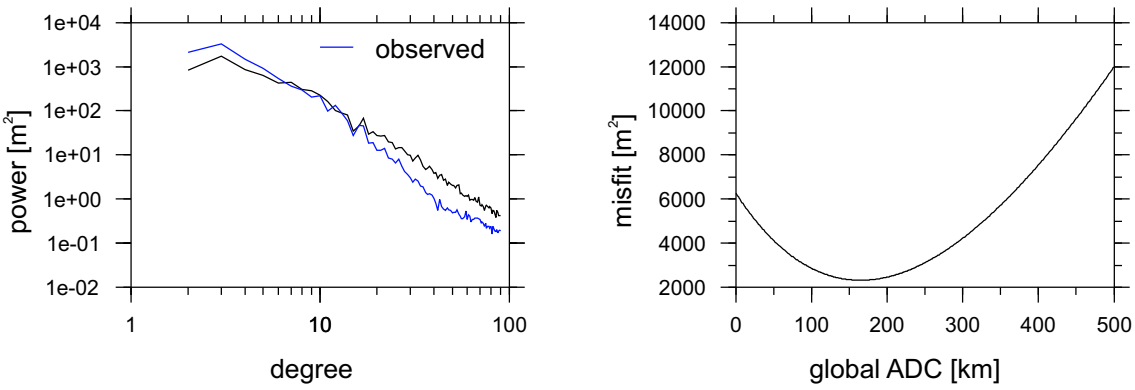

Figure 4.3: Power spectrum of the geoid induced by topography compensated in 165 km compared with the observed geoid power spectrum (left) and a misfit function for compensation in the whole spectral interval j=2-90 (right)

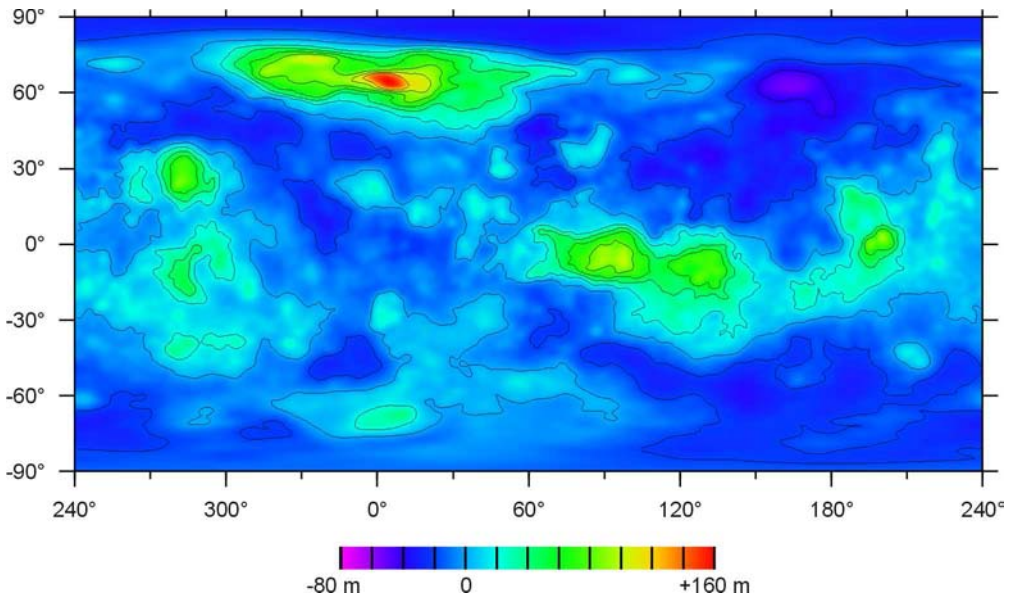

Figure 4.4: Geoid induced by topography compensated in 165 km. The predicted geoid shows similar defects to the uncompensated one, especially overcompensation at Istar Terra (twice the signal of the observed data) and Ovda Regio

least-squares misfit (based on A.29) between our model's predictions and the observed data. In the misfit diagram (Fig. 4.3) we see that the minimal misfit is obtained for a global ADC of 165 km. Such a crustal thickness model, however, produces a power spectrum (Fig. 4.3) and a geoid (Fig. 4.4) which are not in close agreement with observed data.

The second hypothesis which we will test is the assumption that only small scale venusian topography is isostatically compensated. Hence we apply the previously used method for finding a global ADC separately for each degree in the SH model (Arkani-Hamed, 1996). In the resulting diagram (Fig. 4.5 left) we can see the optimal depths of compensation for surface features at all wavelengths. At degrees j=2-40 the ADC is decreasing more or less monotonously from 200 to 30 km. But for degrees $j > 40$ the global ADC stays almost constant – from a misfit minimization (Fig. 4.6 right) we obtain a value of 35 km. Therefore we can suppose that the features smaller than approximately 500 km are well compensated by the crustal isostasy. Another approach to this problem (Simons et al., 1997) is based on fitting the admittance curve (Fig. 4.5 right) – calculated by using the equation A.15 – by the theoretical curve for the compensated topography. As shown, for degrees 40-90 a predicted admittance for compensation depth 35 km fits well with the observed values.

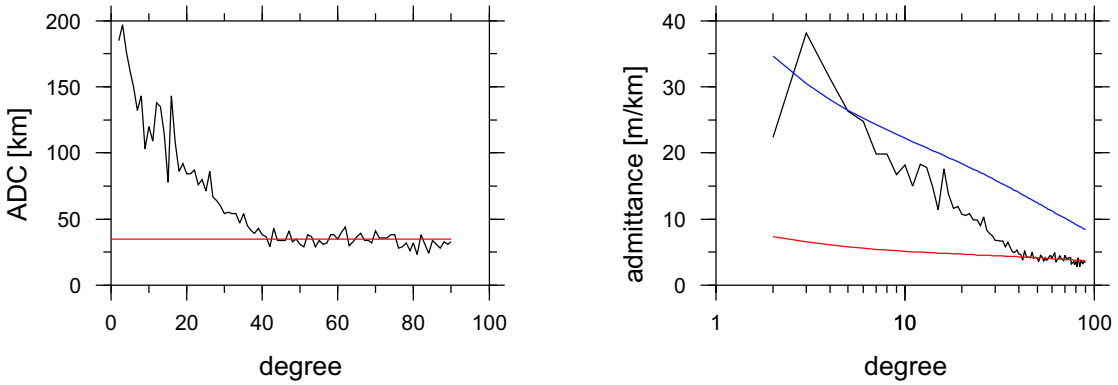

Figure 4.5: Degree ADC and degree admittance between the geoid and topography with synthetic admittance curves for 35 (red line) and 165 km (blue line) thick crust.

When we are studying the resulting power spectrum (Fig. 4.6 left) and geoid (Fig. 4.7) we find no direct contradictions with observed data and therefore this model of isostatic topographic support is acceptable. However, the amplitudes of both compared quantities are smaller than observed ones. From that we can assume that the geoid generating mechanism is not only of isostatic nature but rather some complex mechanism with a possible isostatic contribution from shallow compensation. This judgement then implies the possible importance of some active processes in Venus interior (presumably in the mantle) which will be studied in the next chapter.

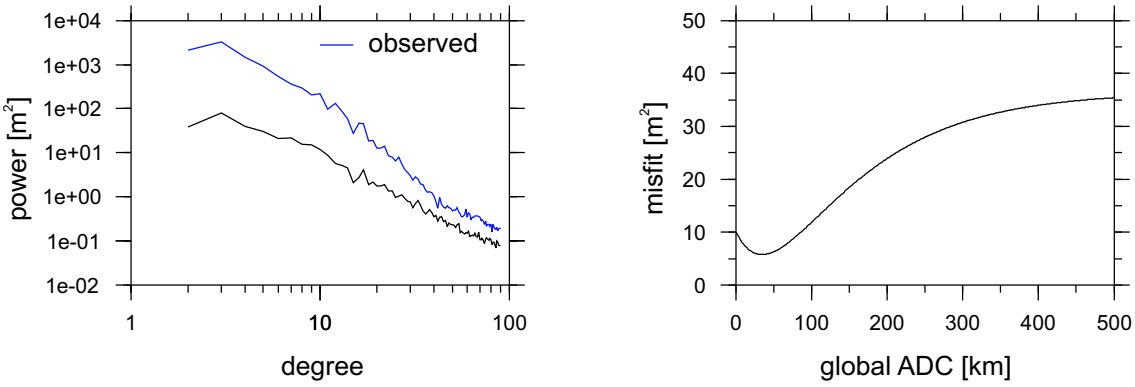

Figure 4.6: Power spectrum of the geoid induced by topography compensated in 35 km compared with the observed geoid power spectrum (left) and a misfit function for compensation in the spectral interval j=40-90 (right)

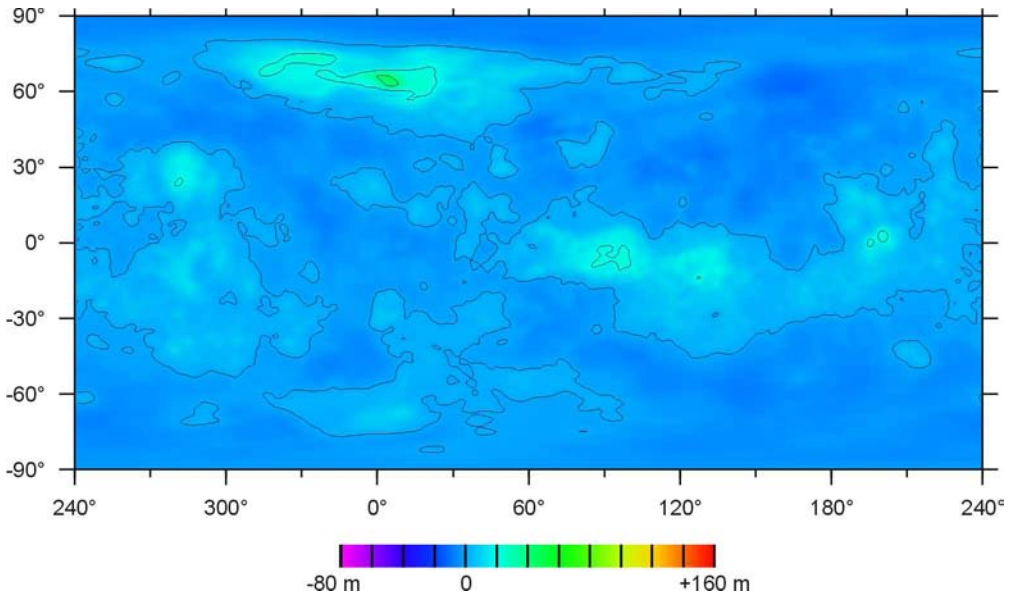

Figure 4.7: Geoid induced by topography compensated in 35 km. We can see that biggest contributions are in the tectonic or volcanic areas such as Ovda Regio, Ishtar Terra or Maat Mons but these should be taken only as minor components of the observed field

4.3 Degree ADC Method for Other Planets

Because the used method of degree ADC (as well as the corresponding method of degree admittance) is simple and in the case of Venus gives us a reasonable results we would like to see if it also has a general validity for other planets. Fortunately as can be seen on the next page this method more or less also works well for the Earth and Moon and therefore does not cast doubt on our results obtained for Venus.

For Earth the situation is similar to Venus. When we study the geoid induced by an uncompensated topography (e.g. Rožek, 2000) we obtain a field with amplitudes one order of magnitude higher than the observed one. From seismic experiments we know that Mohorovicić discontinuity is situated approximately 30 km beneath the continental surface and less than 10 km beneath the sea-floor. Looking at the degree ADC diagram (Fig. 4.8 left) we see that our results (at degrees $j > 50$ the global ADC between 15 and 25 km) are somehow averaging these values and therefore are in agreement with the observations. The admittance diagram (Fig. 4.8 right) confirms this – it also shows interesting negative admittance values for long wavelengths which are probably caused by the anticorrelating geoid and topography.

The size of the Moon is half of the size of Earth or Venus but the anomalies of the geoid are of one order of magnitude higher (Fig. 3.8). The main contribution to its gravitational potential is from subsurface mass concentrations and impact basins – moreover from the Apollo seismic experiments and mare observations we assume a near-side/far-side dichotomy where the crust of the far-side could be twice as thick as of the near-side. The uncompensated topography model predicts similar values to the observed ones suggesting that the main contribution to geoid is presumably not of dynamic origin. When we carry out the degree ADC method (Fig. 4.9 left) we find for degrees $j > 20$ a compensation depth of around 20 km which is in agreement with the latest processing of the Apollo Passive Seismic Experiment which gives a compensation depth of around 30 km. However the oscillations of ADC diagram as well as some anomaly in the admittance curve at degree j=10 (Fig. 4.9 right) signalize a strange behavior of lunar gravity and topography.

Finally we applied the methods of degree ADC and admittance to the planet Mars. Nevertheless because a strong alias effect in the geopotential model GMM-2B (and maybe also because of the major surface features – the giant Tharsis uplift and nort/south dichotomy) we are not able to determine the global ADC value. However from local values the crustal thickness $\sim$ 50 km has already been derived (Zuber et al., 2000).

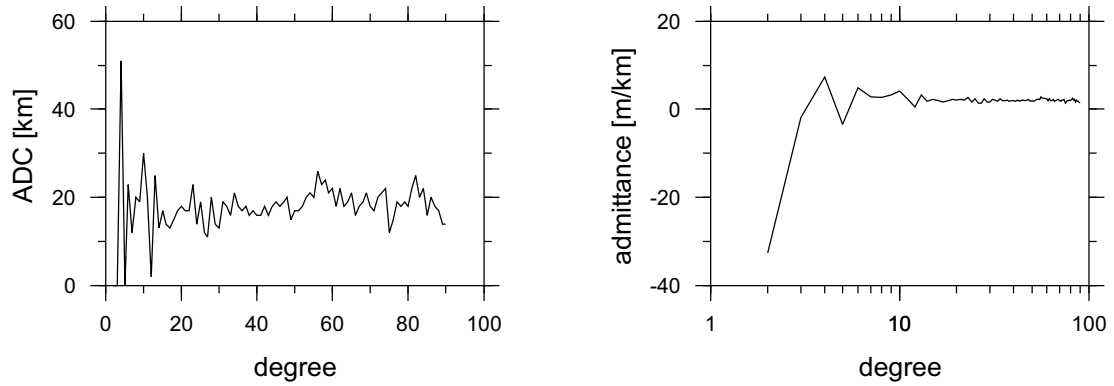

Figure 4.8: Degree ADC and admittance function in the case of Earth

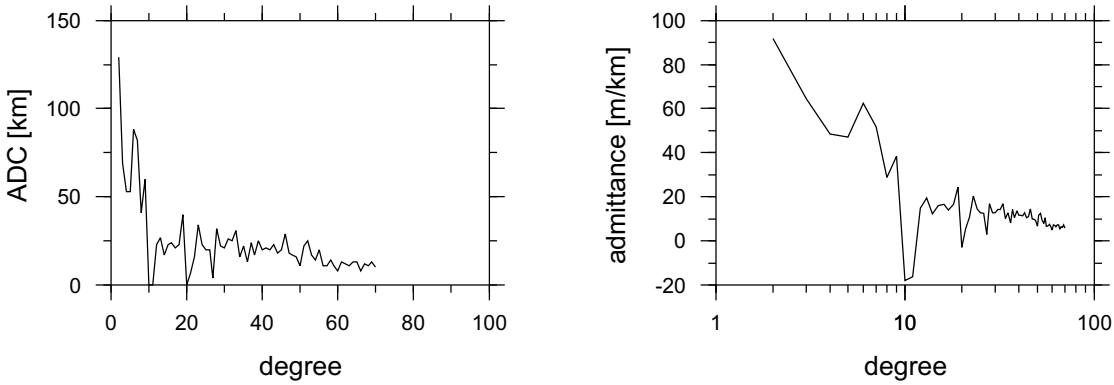

Figure 4.9: Degree ADC and admittance function in the case of Moon

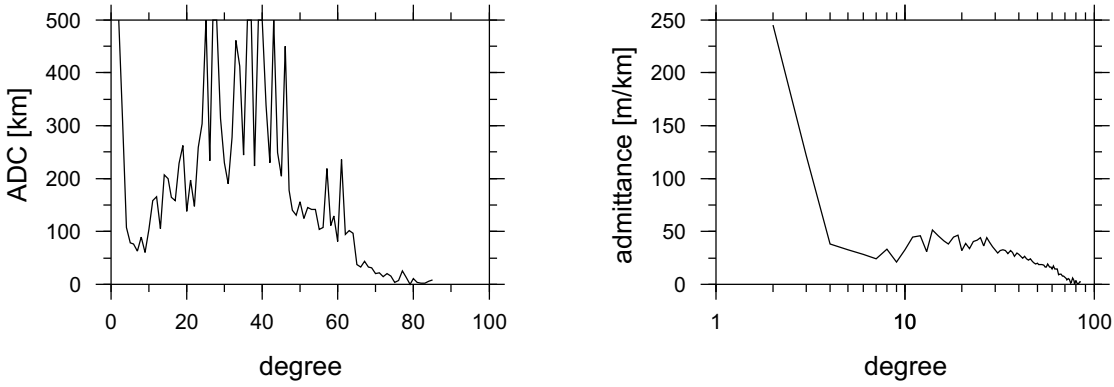

Figure 4.10: Degree ADC and admittance function in the case of Mars

Chapter 5

Dynamic Model of Geoid

In our effort to determine the mechanism providing the support of observed topography at the long-wavelength part of spectrum, we focus on the dynamic processes in the mantle, as they are supposedly still active (e.g. Schubert et al., 2001) and because their numerical modelling could give us valuable results concerning the inner structure of Venus (Kiefer and Hager, 1992; Kiefer and Peterson, 2003).

In mantle convection the common principle driving the whole process are the buoyancy forces induced by thermal (i.e. density) inhomogeneities. The relatively hot and cold parts of mantle induce the flow which is controlled by both density structure and mantle rheology.

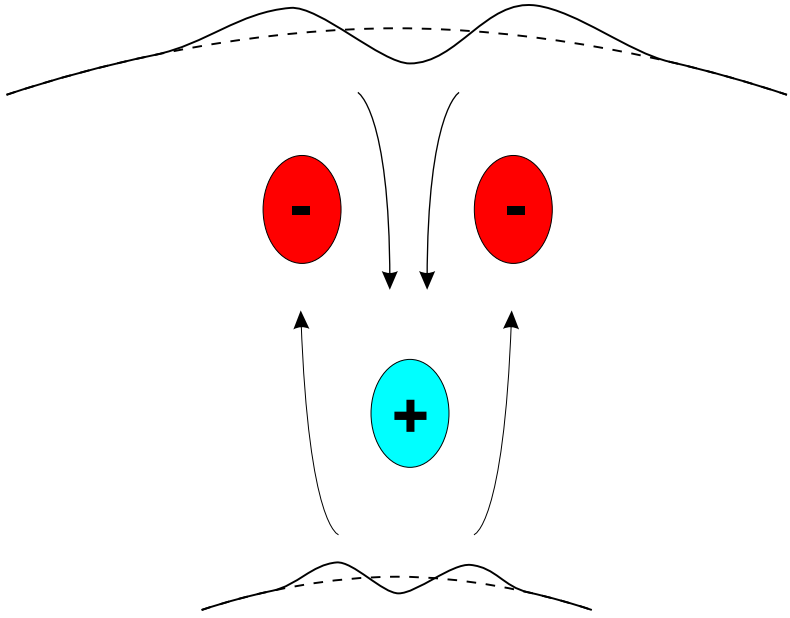

Figure 5.1: Upwellings and downwellings in the mantle induced by negative (red) and positive (blue) density anomalies. At the boundaries the buoyant forces induce non-zero stress deforming both the surface and CMB

The stress associated with this motion of mass acts on any boundary – surface, CMB – of the mantle and deforms them (schematically in Fig. 5.1). The dynamic topography predicted at the surface could be successfully compared in the case of Venus to the observed one. Moreover the uneven mass distribution beneath the surface together with the dynamic topographies at the surface and CMB induces the variations in the geopotential – which could also be compared to the long-wavelength geoid observed. By looking for a model with the highest agreement with observed data we can learn about the mantle properties.

Our work is based on the internal loading theory which has already been successfully used for forward modelling of venusian interior (Kiefer et al., 1986; Kiefer and Peterson, 2003). However our approach combines this useful tool with an inverse problem formulation and therefore our results should have a global validity and higher robustness than results from forward modelling. The extensive description of our approach is given in Appendix C. The major step done by our work was considering only 2D density variations constant with depth (i.e. $\rho = \rho(\vartheta, \varphi)$) to avoid ambiguity in the solution. Because we have no information about the density variations within the venusian mantle, we could obtain the same result (dynamic geoid or topography) for any given viscous profile by using a number of different ρ_{jm} models. Therefore to obtain a unique solution we fix the density variations at a value calculated to best fit both observed fields. Among such models we then look for those with minimal L_2 norm misfit when compared with observed data.

We have adopted two approaches to solve this nonlinear problem – the Monte Carlo method (random search in the model space) and the simulated annealing algorithm (random search with successive focusing). We consider the mantle with layered viscosity profile ($n-1$ layers with viscosity varying 10^0-10^5 and an uppermost layer with fixed viscosity 10^5). In Fig. 5.2 we can see the results for $n = 3, 4$ (the model for $n = 2$ was omitted because of general inconsistency with successive models) obtained by the Monte Carlo method (the 10 best from 1,000,000 and 2,000,000 runs respectively) superimposed with the best solutions reached through the simulated annealing algorithm (red lines).

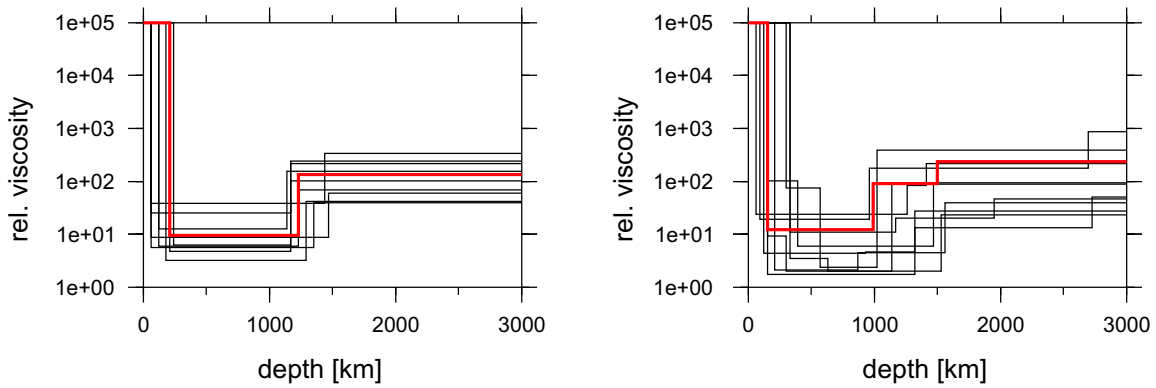

Figure 5.2: The best viscosity profiles for 3 and 4 layer models of venusian mantle. The Monte Carlo results (black lines) mark the class of possible solutions whereas for comparison between models we use single results obtained by the simulated annealing (red lines)

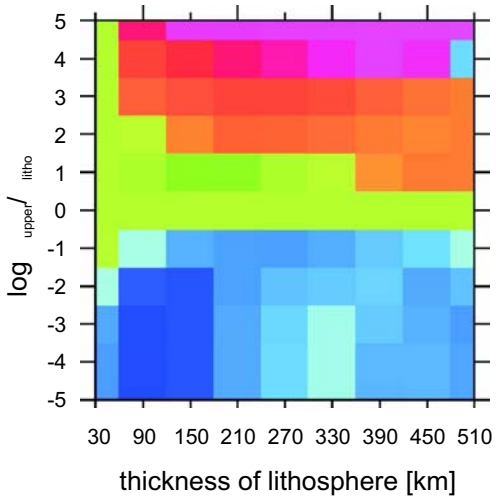

Figure 5.3: The minimum misfit for various viscosity contrasts (10^5-10^{-5}) between the upper mantle and lithosphere. The minimal values are blue and the maximal ones are red – the 2 layer (60 km) step was used

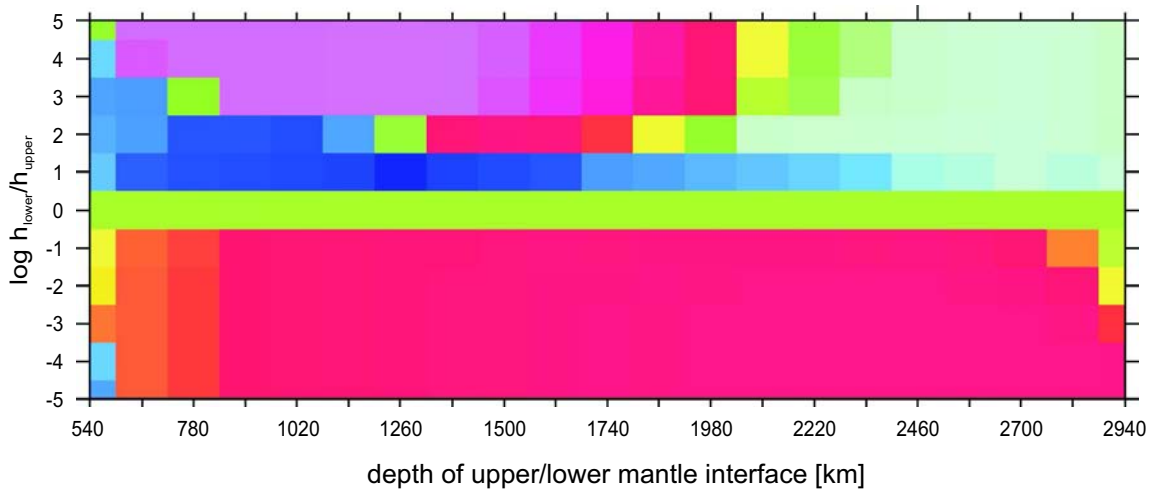

Figure 5.4: The minimum misfit for various viscosity contrasts (10^5-10^{-5}) between the lower and upper part of the mantle. The minimal values are blue whereas the maximal ones are red – the 4 layer (120 km) step was used

The number of parameters of our random search is $2n - 1$ plus the density distribution given by a set of SH coefficients ρ_{jm}. However this model vector is not a free parameter as we decided to compute its value analytically to minimize the misfit between observed and predicted values (C.28). To analyze the resolving power of our inverse problem formulation we choose the model $n = 3$. In Fig. 5.3 we can study the resolution of viscosity changes between lithosphere and upper mantle and their positions. Whereas the depth of the lithosphere seems to be located relatively well between 100-200 km, the viscosity drop connected to this remains in a wide interval. The following viscosity change (Fig. 5.4) seems on the other hand to be well detected (increase by 1-2 orders of magnitude) but can be placed at a wide interval of depths. Therefore we can assume that such an increase is not a manifestation of a low viscosity zone end but rather of a gradual viscosity rise.

In comparison to the isoviscose mantle model we can reduce, by using the various viscosity models, the misfit between the predicted and observed data to about 2/3. However, we can also consider another parameter of the agreement – the percentage of predicted data p (C.30). For our method and various viscosity profiles we can well predict about $90 - 95\%$ of both the geoid and topography. However, between individual random-search solutions the difference in p is insignificant (does not directly depend on n) which could be a consequence of strong nonlinearity of our inverse problem.

The following statements are made for the solution obtained for $n = 4$ by the simulated annealing algorithm although the difference to other results is rather minor. The comparison of power spectra and the correlation between observed and predicted quantities (Fig. 5.5) could be a valuable tool in the evaluation of our findings. The correlation between predicted and observed data is overall very good which supports the dynamic support hypothesis. The power spectra of geoids and topographies differ slightly nevertheless the predicted/observed geoid difference is noticeable around $j = 10$, where we can assume some other minor contribution to the observed geoid.

The degree admittance function was not a constrained quantity but when we compare a prediction with the observed values (Fig. 5.6) we can also see a good fit to this parameter. The predicted geoid and topography (Fig. 5.7 left) seems to have the major features corresponding well to the observed ones (same figure, at right). However, for precise spatial studies we have mathematical tools not just based on intuitive comparison – for details see Chapter 6. Despite the basic simplification in obtaining the density lateral variations inducing the mantle flow (Fig. 5.8 left) the uppwelling and downwelling structures do often coincide with the assumed mantle structure. This is not only the case of volcanic uplift sites (Atla or Beta Regiones) and major lowlands (Atalanta or Lavinia Planitias) induced presumably by ascending and descending mantle flows but maybe also of some highlands like Ovda or Thetis Regiones (Kiefer and Hager, 1992).

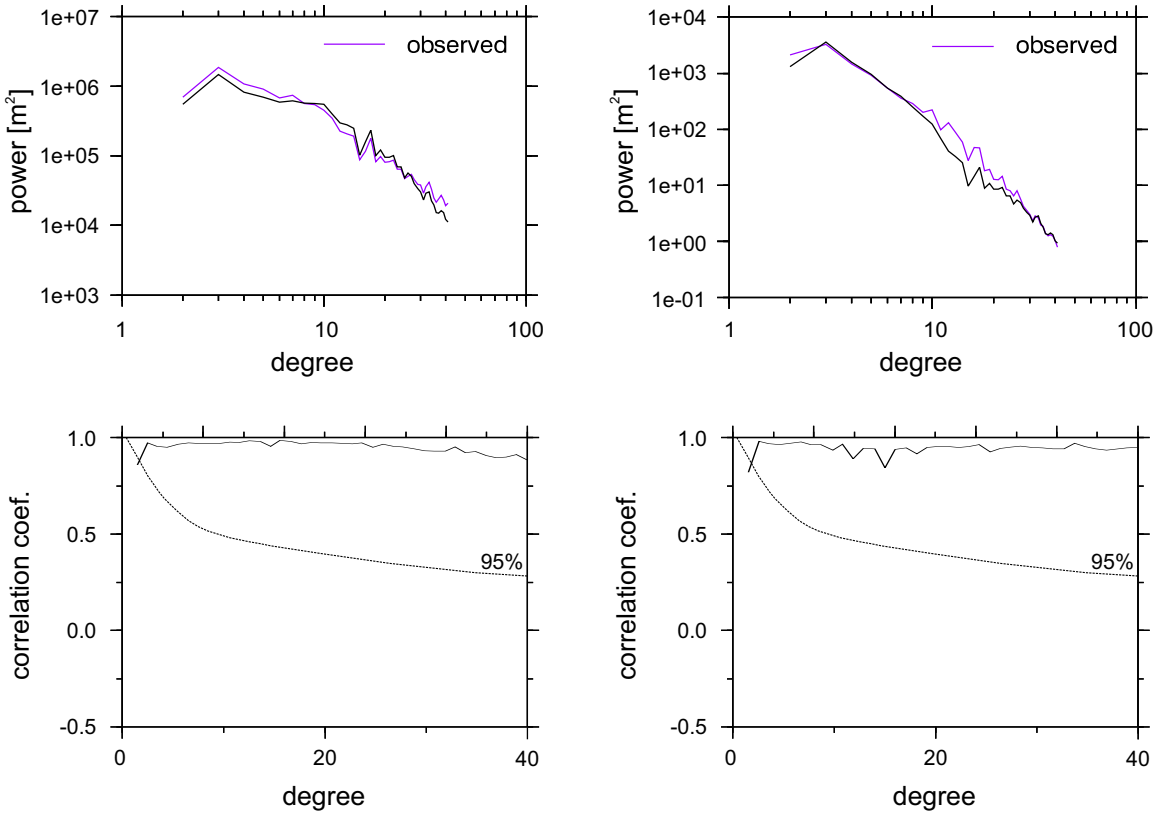

Figure 5.5: The power spectra of predicted dynamic topography (left) and geoid (right) together with observed ones and their degree correlation with observed data. Dashed lines again denote the 95% level of confidence

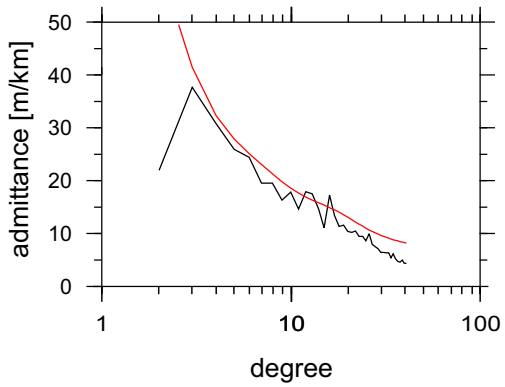

Figure 5.6: Observed degree admittance (black curve) and predicted dynamic one (red curve). Good agreement is observed approximately up to degree $j = 25$

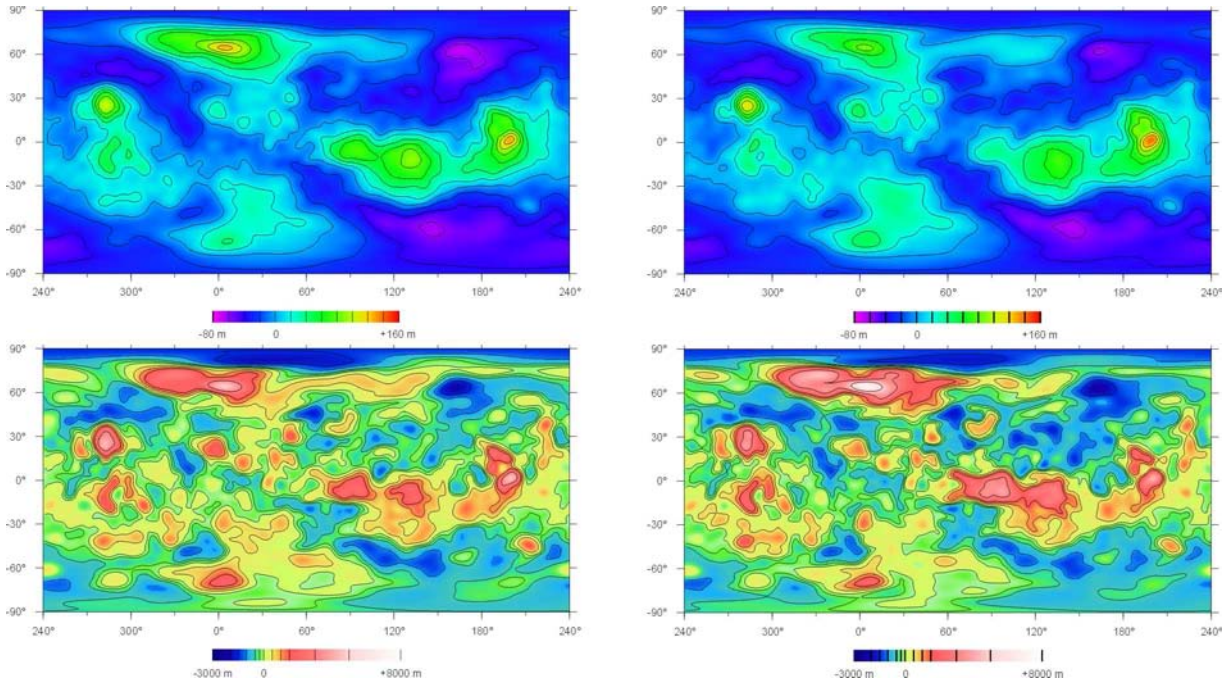

Figure 5.7: Comparison of predicted (left) and observed (right) geoid and topography for wavelengths j=2-40. The biggest difference could be seen in the regions containing tectonic features like surroundings of Ishtar Terra or Aphrodite Terra highlends

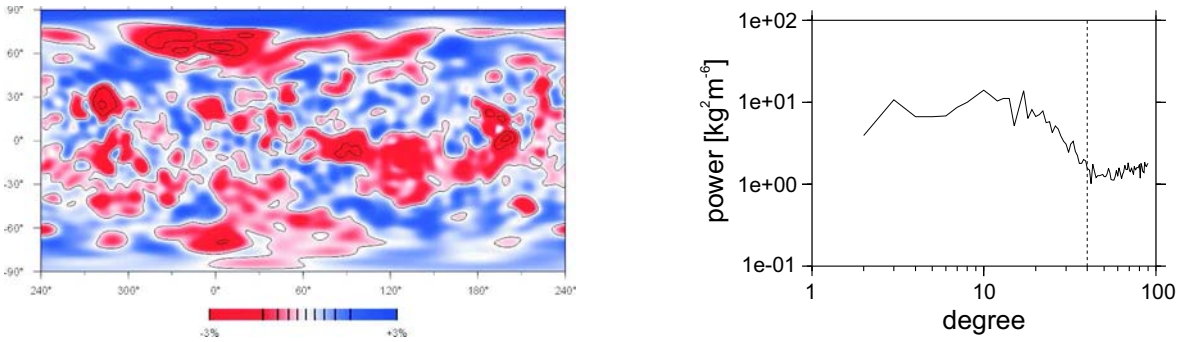

Figure 5.8: Inducing density (j=2-40) for the n=4 result obtained by the simulated annealing (left) and its power spectrum (right) – the power spectrum for $j > 40$ is also plotted here for character study (right of the dashed line)

For $n \geq 4$ the resulting viscosity profiles contain some instabilities compared to previously obtained trends (Fig. 5.2). The typical one with an inserted stiff layer (Fig. 5.9 left) seems to be generated by the nonlinear character of the inverse problem – it appears increasingly with higher n and does not have a steady shape but rather is positioning the high-viscous layer randomly. However the second characteristic one with a viscosity drop of somewhere between 80-100% in the depth of the mantle (Fig. 5.9 right) corresponds to the previous trends of uniform increase through the mantle. The presence of such low viscosity transitional zone above the core has not yet been reported which can be due a higher sensitivity of our global inverse model in comparison to the forward models – however because of the low resolution in this deep part of the mantle we cannot accept it unambiguously. But comparing our finding to the fact that Venus presumably still has a melted core which is just slowly cooling down (Stevenson et al., 1983) we may explain it naturally in the way of a transitional mantle zone above the core.

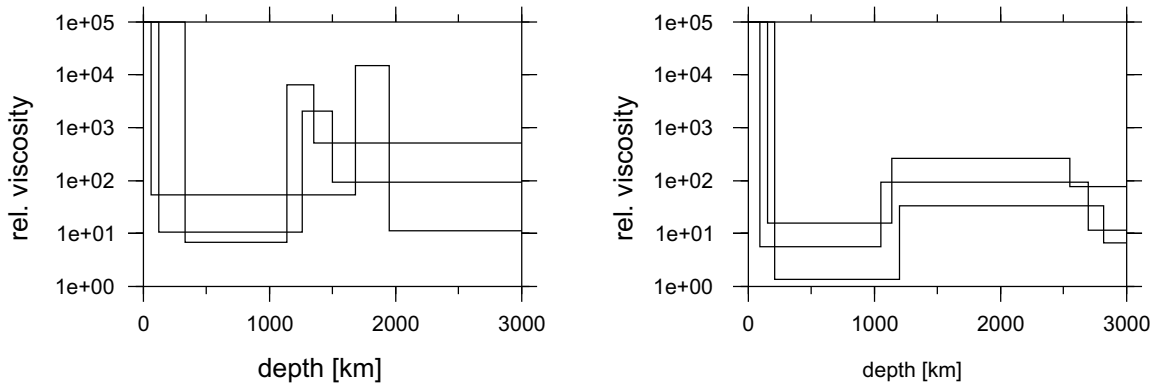

Figure 5.9: Two kinds of viscose instabilities contained in the set of results for n=4 layer model obtained by the Monte Carlo random search method

Chapter 6

Localization Analysis

When we need to study some well localized features in the gravity field (e.g volcanic rise or tectonic rift) or to detect some hidden ones (e.g. crustal thickening contributions), appropriate tools to use are the localization methods. In comparison with the spectral methods – which are for global characteristics – this approach employs the function with compact support and thus is not affected by distant-zone contributions. There are several different ways how of realizing it mathematically (see Appendix B) but for our purposes we chose the method recently presented by Kido et al., 2003 (equations B.16-B.21).

6.1 Localization of Data

Using this approach we first of all examine individually the geoid and topography of Venus (applying equation B.18). In Fig. 6.5 left we can see the localization of the geoid for long and intermediate wavelengths – at right there is the corresponding localization of topography. This can give us the first insight into the mass distribution on Venus as well as on the geoid's major features. This is the first step in data localization analysis which is needed for other studies – all diagrams show a zero-level topography contour.

This method could be used also for the empirical comparison of two fields because the localization reveals the real field's anomalies unaffected by other (global) signals. Such a comparison can also be carried out in the case of localized geoid and topography (Fig. 6.1) but in the next section we introduce a better method for such a task. Instead, we use it to validate our hypothesis of the isostatic support of topography for $j > 40$. In following figures we display a localized geoid for the wavelength $j = 40$ in the three diverse regions of Ishtar Terra, Aphrodite Terra and the surroundings of Phoebe Regio. As these regions have another nature they are obviously also in another isostatic case. Whereas the first of them (Fig. 6.2) seems to be no longer tectonically active and in isostatic equilibrium, for the other two this is most probably not the case. The region of Devana Chasma (Fig. 6.3) seems to be compensated only partially (some authors are arguing a hypothesis that this is a still an active rift – e.g. Kiefer and Peterson, 2003) whereas for the region west of Beta Regio (Fig. 6.4), where the isostasy does not work well, we have a strong presumption from coronae clustering (Squyres et al., 1993) that this could be a site of dynamic activity.

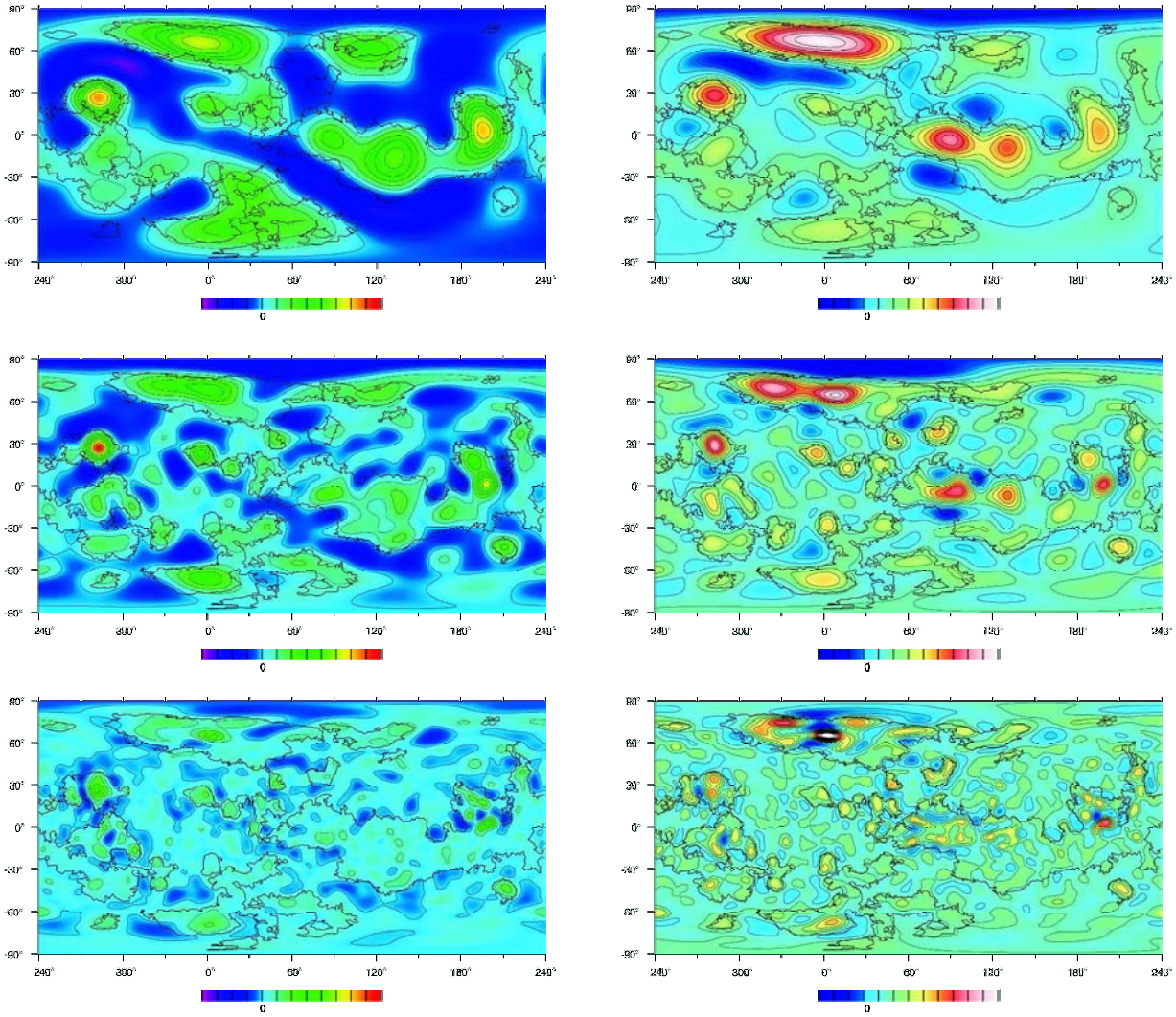

Figure 6.1: Localized geoid (left) and topography (right) for wavelengths $j = 8, 16, 32$ (respectively from top to bottom) in cylindrical projection. For shorter wavelengths the results cannot be displayed as a global view hence the regional studies are preferred. On the geoid localization diagrams we can clearly observe the volcanic rises at Atla and Beta Regiones as well as the contribution of the coronae in Eistla Regio. The localization of topography is revealing the major contributions of the venusian highlands together with Ishtar Terra and major volcanoes. At long wavelengths it apparently corresponds to the localized geoid which is proven by localized correlation studies in the next section

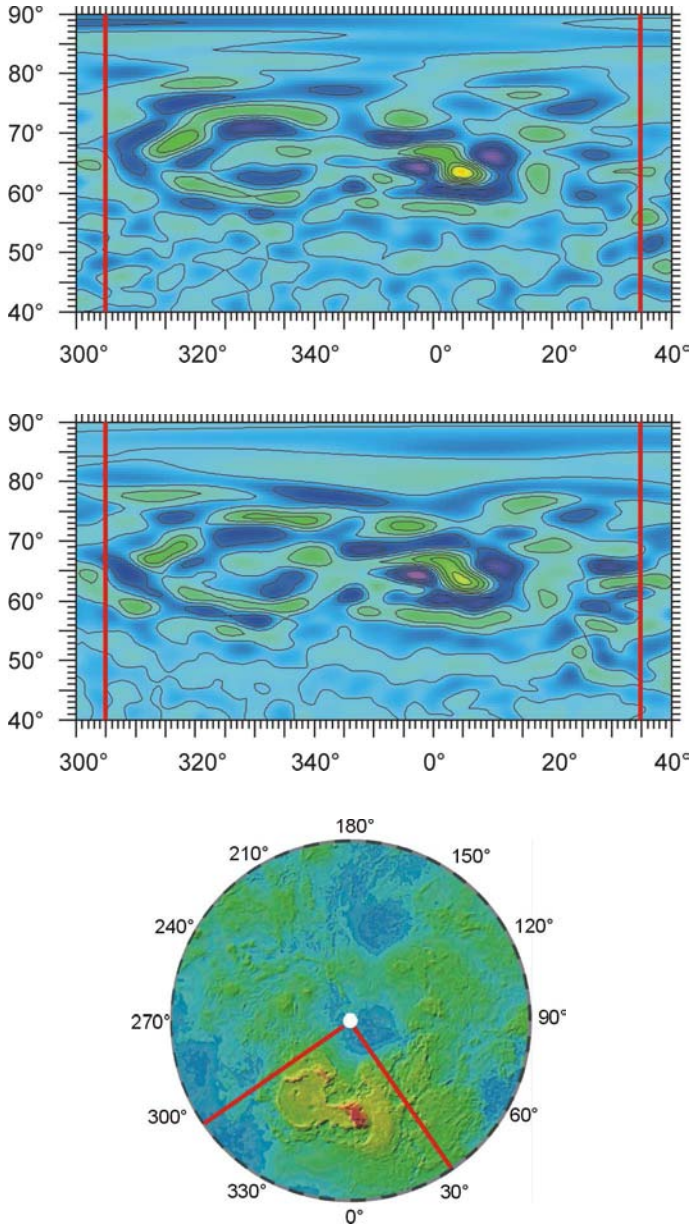

Figure 6.2: Localization of observed and predicted geoid and corresponding topographic map (respectively from top to bottom) for wavelength $j = 40$. The region of interest is in this case Ishtar Terra with the Maxwell Mountains and adjacent Lakhsmmi Planum (the red lines serve as an orientation guide – they are always in the same position)

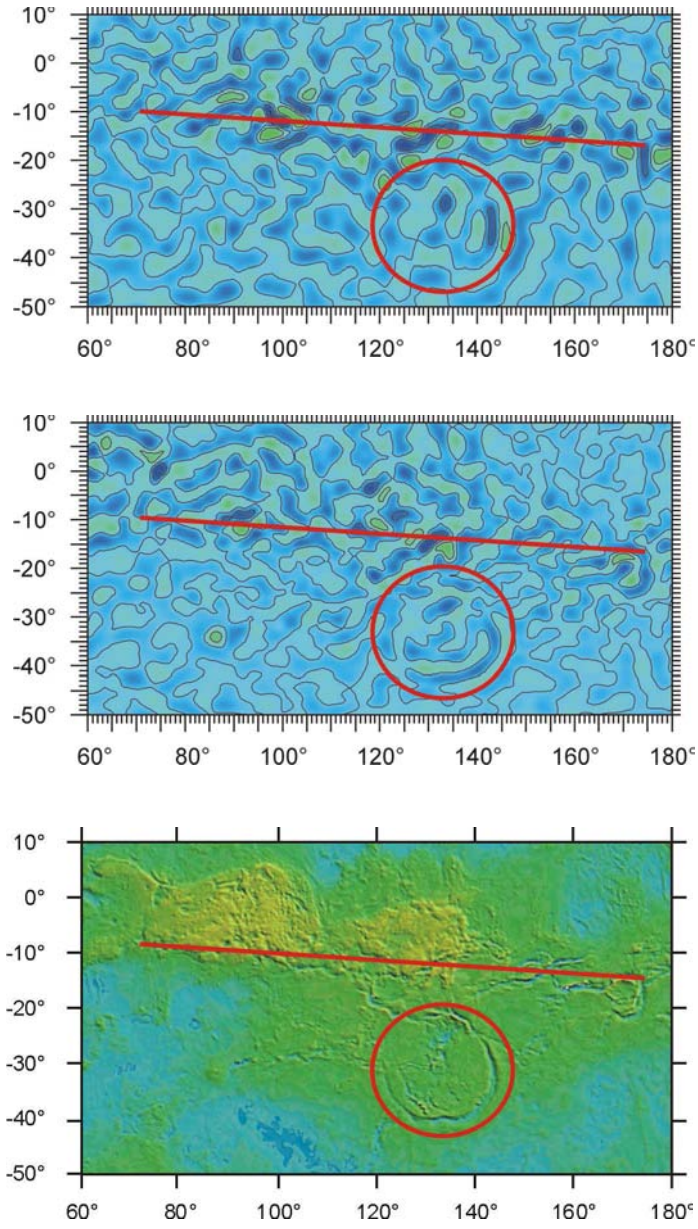

Figure 6.3: Localization of observed and predicted geoid and corresponding topographic map (respectively from top to bottom) for wavelength $j = 40$. The region of interest is in this case Phoebe Regio and close Devana Chasma (the red lines serve as an orientation guide – they are always in the same position)

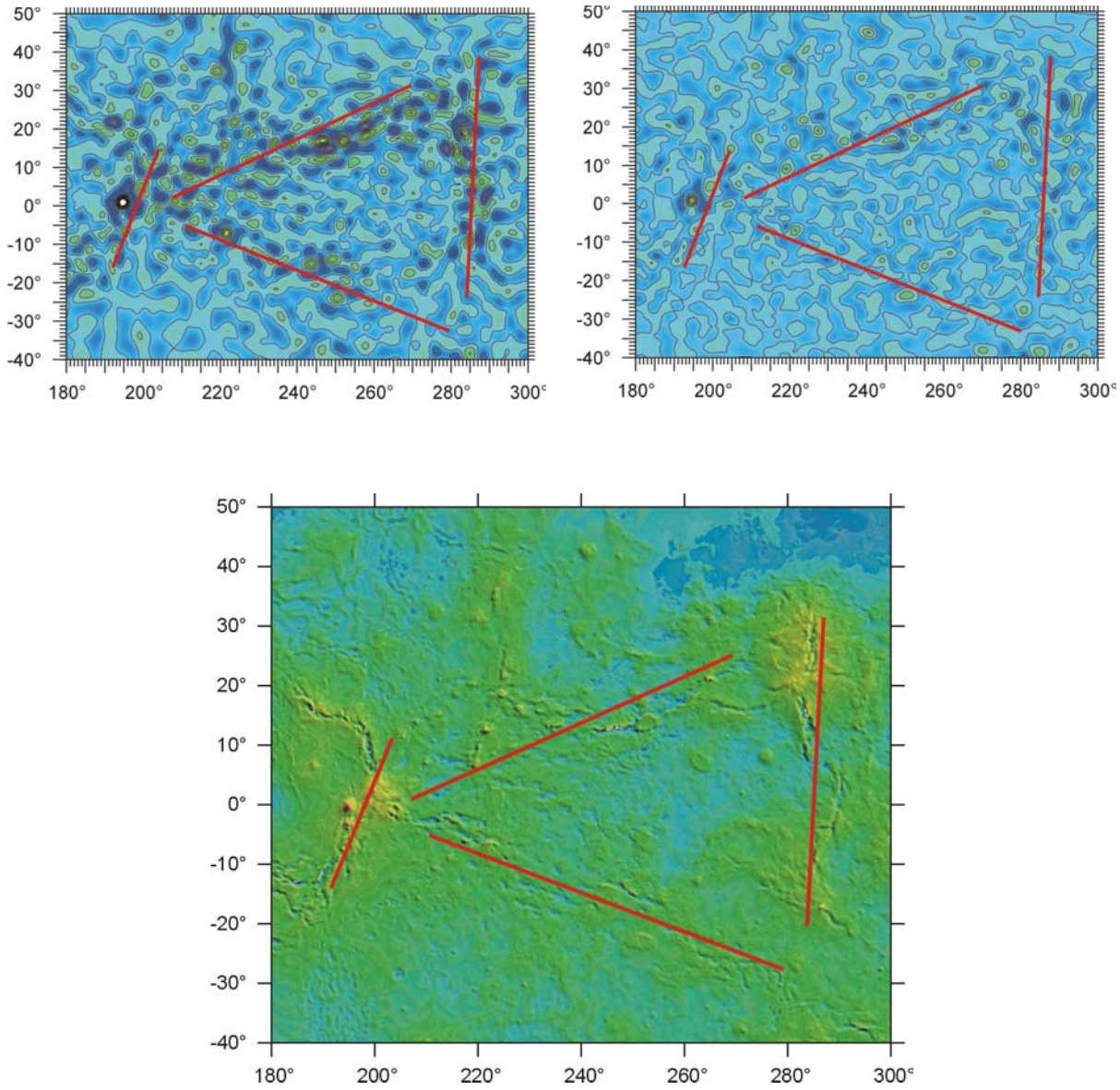

Figure 6.4: Localization of observed and predicted geoid (left and right) and corresponding topographic map (bottom) for wavelength $j = 40$. The region of interest is in this case between Beta and Atla Regiones and Phoebe Regio (the red lines serve as an orientation guide – they are always in the same position)

6.2 Localization of Correlation and Admittance

When we want to compute the degree of agreement between two fields or the transfer function (admittance) we can employ the common spectral approaches (A.13 and A.15 respectively). However this quantity could be quite laterally variable and we would like to separate the sites with higher values from those with lower one. For these purposes we can employ the localized correlation (B.19) and admittance (B.20) which come out from the localization method mentioned in the previous section.

Localized correlation between geoid and topography (Fig. 6.5 left) clearly proves an overall good correlation of the two fields on Venus, which is already known from spectral analysis (Fig. 3.6 left). Moreover we can observe certain regions of the surface which have some lower correlation for intermediate wavelengths – these specific sites mostly coincide with some complicated topographic structures. Therefore we can conclude that generally even the long-wavelength topography on Venus is a manifestation of internal dynamic processes. Studying the localized transfer function between geoid and topography (Fig. 6.5 right) we can distinguish at intermediate wavelengths several prominent surface features like highlands or volcanic raises whereas at long ones we can observe only the general lower values of admittance in the sites of plateaus and tesserae.

We can successfully link this tool to our dynamic modelling problem when we use it for the spatial comparison of the observed and predicted geoid and topography (Fig. 6.6). For this purpose we choose only wavelengths $j = 16, 32$ because of the restriction of dynamic model in spectrum and low resolving power at wavelength $l = 8$. From obtained results we can see the general good agreement between observed data and our predictions in the examined spectral interval. The sites of lower correlation correspond mainly to tectonic highlands where some more complex (not strictly dynamic) mechanisms of origin should be employed. This could be a significant disadvantage of our dynamic model, however, with the chosen simplifications (see section C.3 for discussion) we cannot overcome the basic mismatch between the observed geoid and topography (compare to Fig. 6.5 left).

Moreover if one is interested in the properties of a specific site the method of localized admittance restricted to this region could be used (for more details see again Simons et al., 1997 or Kido et al., 2003). This approach could be helpful in verification of the laterally varying properties as it shows a cross-cut through the entire selected spectral interval for the surveyed quantity at the site.

6.3 $\tilde{E}_{max}$-k_{max} Method Applied on Venus' Geoid

When we wish to examine anomalies with maximum energy (i.e. with maximum localized signal) at different scales we can employ the localization for each individual wavelength and study them separately or we can use a compositional method. In this thesis we applied to the planetary geoids the $\tilde{E}_{max}$-k_{max} method (equation B.23) which analyzes the contributions from localization at all wavelengths over a given spectral interval and displays the highest value at each grid point.

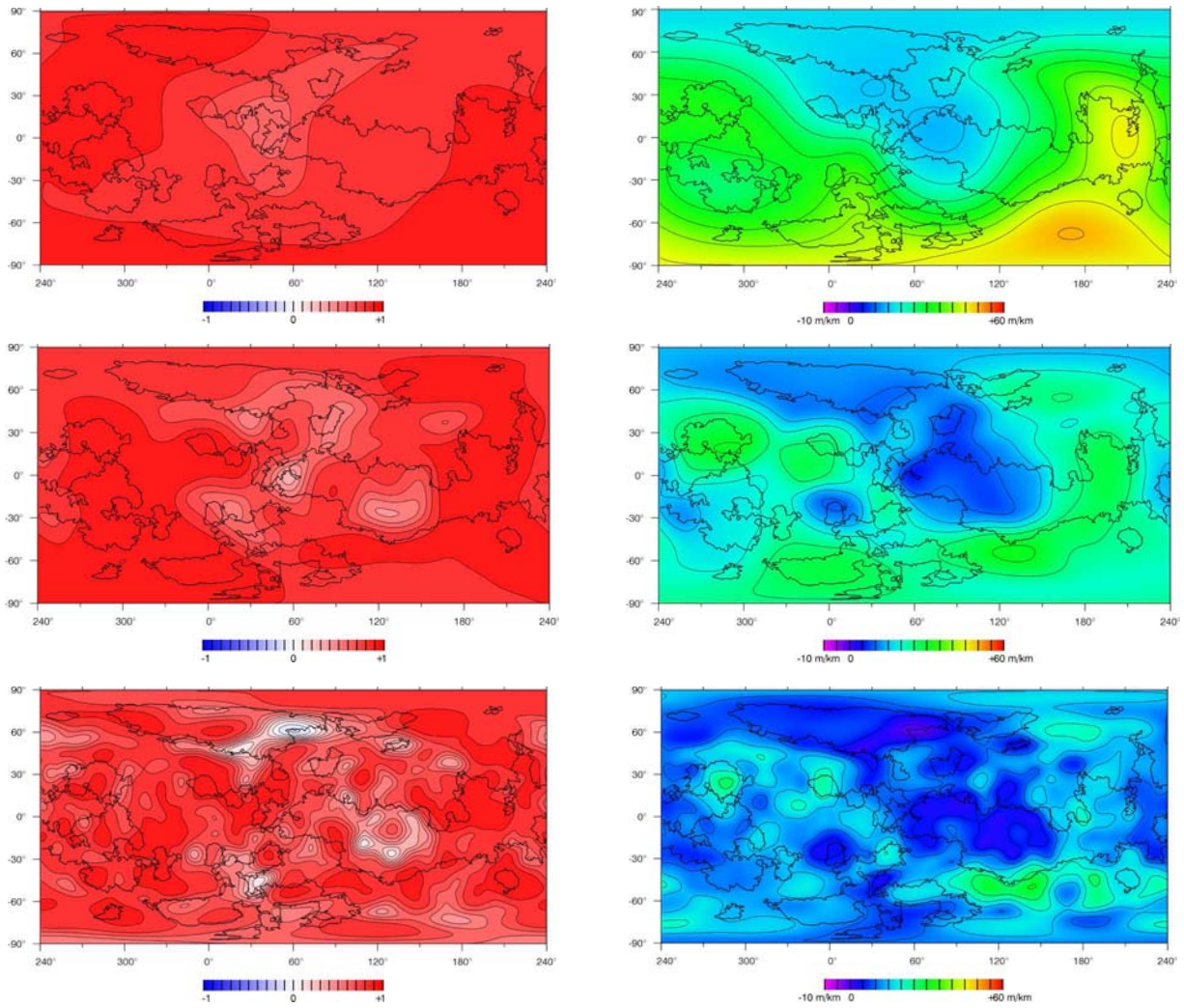

Figure 6.5: Localized correlation (left) and admittance (right) between venusian geoid and topography for wavelengths $j = 8, 16, 32$. The admittance function gives reasonable results only in sites of correlation $|C| > 0.5$ because otherwise it is not clear what the sense of the transfer function between these fields is. Despite the fact we are using another method a comparable results can be found in Simons et al., 1997

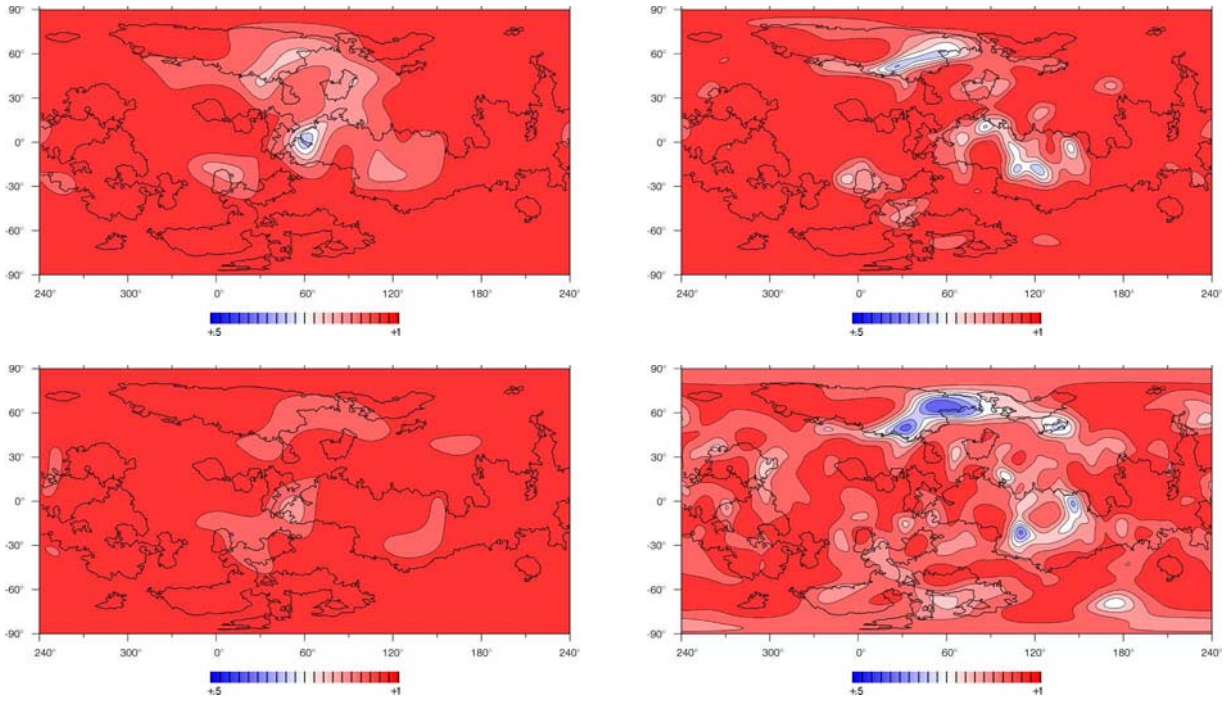

Figure 6.6: Localized correlation between the observed and predicted geoid (top) and the observe and predicted topography (bottom) for dynamic modelling at wavelengths j=8,16 (from left to right). Please note the change in color scheme from Fig. 6.5

In Fig. 6.7 and Fig. 6.8 we can see the $\tilde{E}_{max}$-k_{max} maps of the venusian geoid for long and short wavelengths respectively – for intermediate ones the result do not differ too much from these. However because of the already mentioned good correlation between the geoid and topography even at long wavelengths the signature revealed by the $\tilde{E}_{max}$ map is mainly connected to major topographic features. Surprisingly at the short wavelengths the most prominent signal is induced by volcanic rises and highlands and not by deep and long trenches (e.g. Devana Chasma or Artemis Chasma). The second part of analysis – the k_{max} map – is strongly influenced by the fact that in the regions of signal sign change even the weak short-wavelength is getting the strongest signal. However we can observe several complicated structures in Ovda and Thetis Regiones but the most prominent is located between Atla and Beta Regiones where the largest cluster of coronae is located (Squyres et al., 1993).

Some authors proposed the possibility that remanent signs of plate tectonics could be inferred by these studies or some subsurface features could be revealed but none of them were found by our research. If any such hidden structures still exist on Venus, some other way to detect them must be used, basically after obtaining new data. The most efficient way would be a multiple seismic probing of the venusian interior but other methods are also available today e.g. sonar probing.

6.4 $\tilde{E}_{max}$-k_{max} Analysis for Other Planets

As we have found the $\tilde{E}_{max}$-k_{max} method useful in detailed survey of the venusian geoid we can apply it also on the gravity fields of other terrestrial planets.

In the case of Earth a similar analysis done by means of wavelet transform was carried out by Vecsey et al., 2003. Therefore our findings just confirm their results for regions not far from the equator. However our technique enable us also to examine the polar and subpolar regions. In Fig. 6.9 we can see the analysis for long wavelengths which is dominated by Greenland-Iceland, New Guinea and South America positive anomalies and by Asian, Antarctic and North American depressions. The Hawaiian and African hotspot contributions also appear. On the other hand Fig. 6.10 shows many features easily connected to surface or subsurface features e.g. the middle-oceanic ridge in the Atlantic and other sea-flour structures, Iceland's hotspot signature, the Baltic sea depression and Spitzbergen volcanic signal, the Canadian depression etc.

For the Moon the situation is less complicated because of the presumed end of dynamic processes in the lunar mantle. Hence all the phenomena on the $\tilde{E}_{max}$-k_{max} maps should have an origin in observed topographical (e.g. craters, basins) or subsurface (mascons) features. Special attention should be given to the mascons (positive signals in the center of depressions – short for ***mas***s ***con***centrations) as they are signs of complicated geological structure initiated most likely by giant impacts. In Fig. 6.11 the mascons connected to Mare Imbrum, Mare Serenitatis, Mare Crisium and Mare Nectaris really dominate the near-side whereas on the far-side is the major feature the South Pole-Aitken basin with a negative signal. However besides smaller craters and mare anomalies, one adjacent to the irregular Mare Marginis appears (circled). This is very promising for new research as this area could be an old impact basin (Wilhelms, 1987) covered by subsequent tectonic activity. In Fig. 6.12 only small-scale features mainly connected to the basin and crater rims are displayed – this offers a promising tool for localization of new mascons (Konopliv et al., 2001) in upcoming geoid models. The insufficient regularization of the used gravity model is obvious here on the far-side.

The martian geoid is dominated by a bipolar structure created by the assumed single-cell mantle dynamics (e.g. Harder and Christensen, 1996) which has most probably already ceased. Therefore the long-wavelength analysis in Fig. 6.13 shows these two main features together with some smaller contributions from topographic structures like Elysium Mons, Isidis Planitia or Hellas basin. However in Fig. 6.14 we can observe a complicated signal surrounding Olympus Mons and Valles Marineris and also some sign-changing signal (circled) south of Elysium Mons. The latter is probably induced by the unusual topographic structure observed here but some others connected to martian crust-dichotomy or ancient shore-line may be found through more detailed research on new gravity maps being obtained by current space missions.

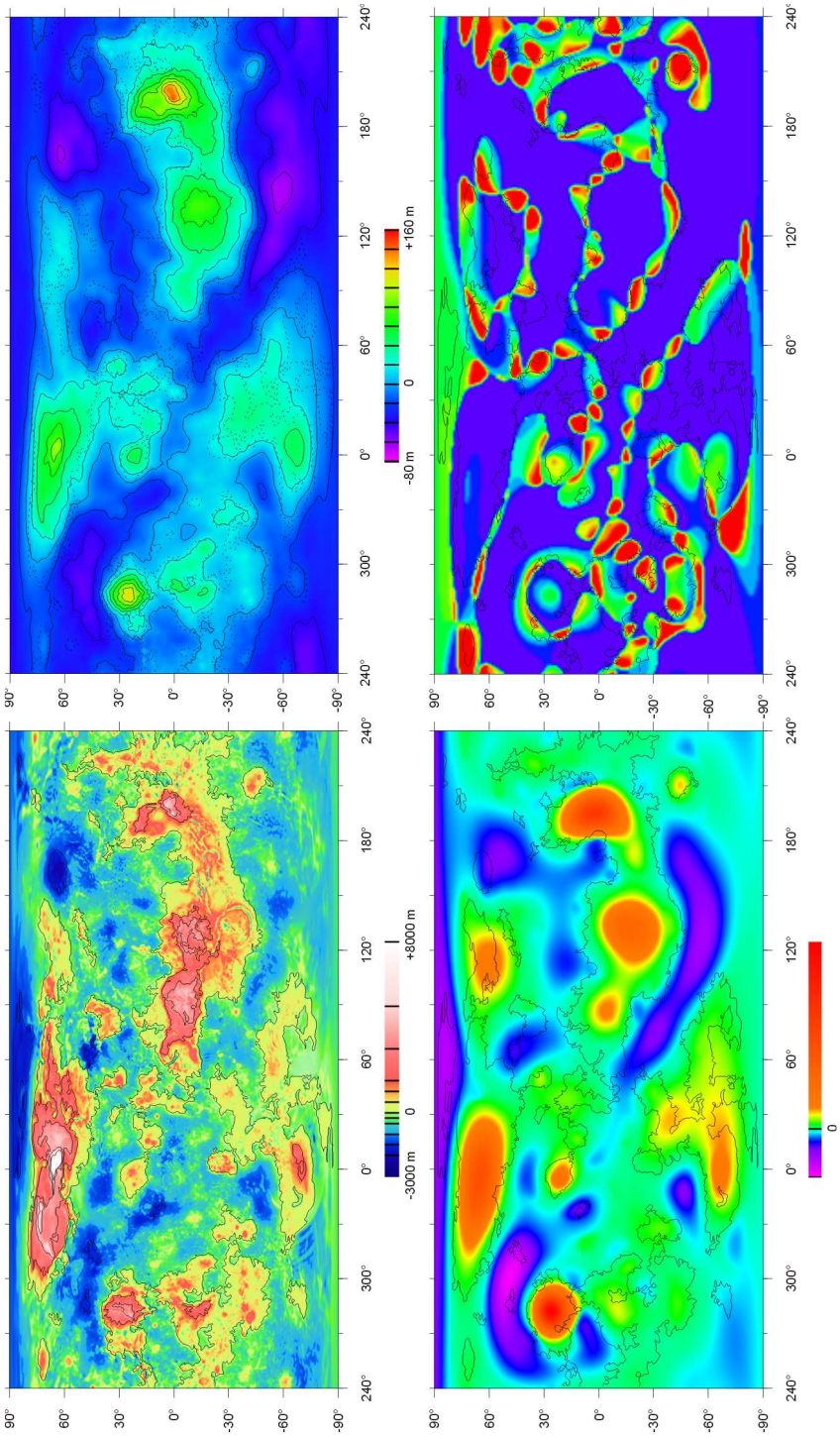

Figure 6.7: At top, the topography and geoid of Venus, at bottom the E_{max} and k_{max} maps of the geoid for j_w=08-16. We can clearly observe the dominant dynamic part of the geoid which coincides with major topographic masses

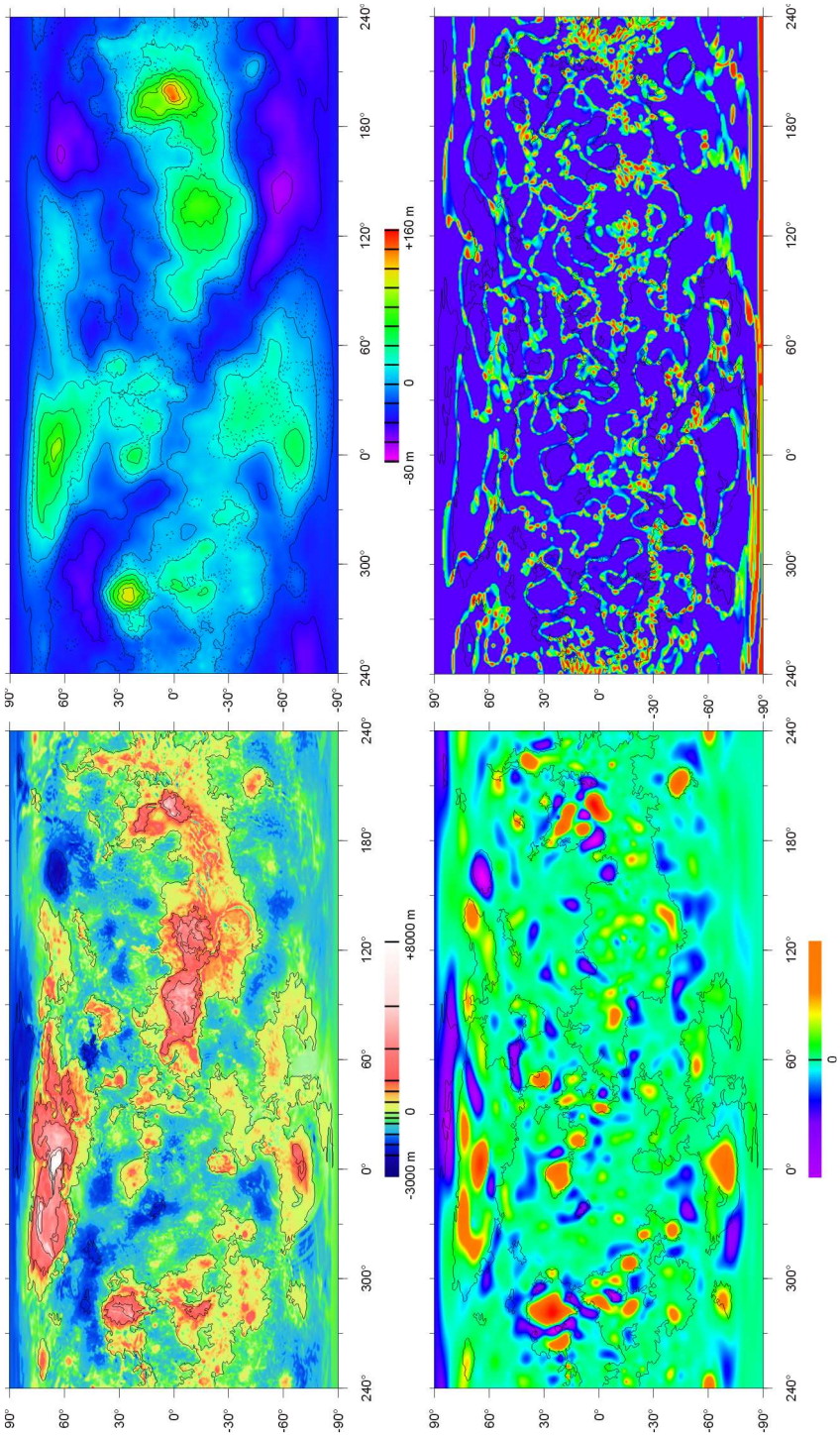

Figure 6.8: At top, the topography and geoid of Venus, at bottom the E_{max} and k_{max} maps of the geoid for j_w=32-64. Even with a small scale we can see good agreement between both fields and coronae clustering in equatorial region between Atla and Beta Regiones

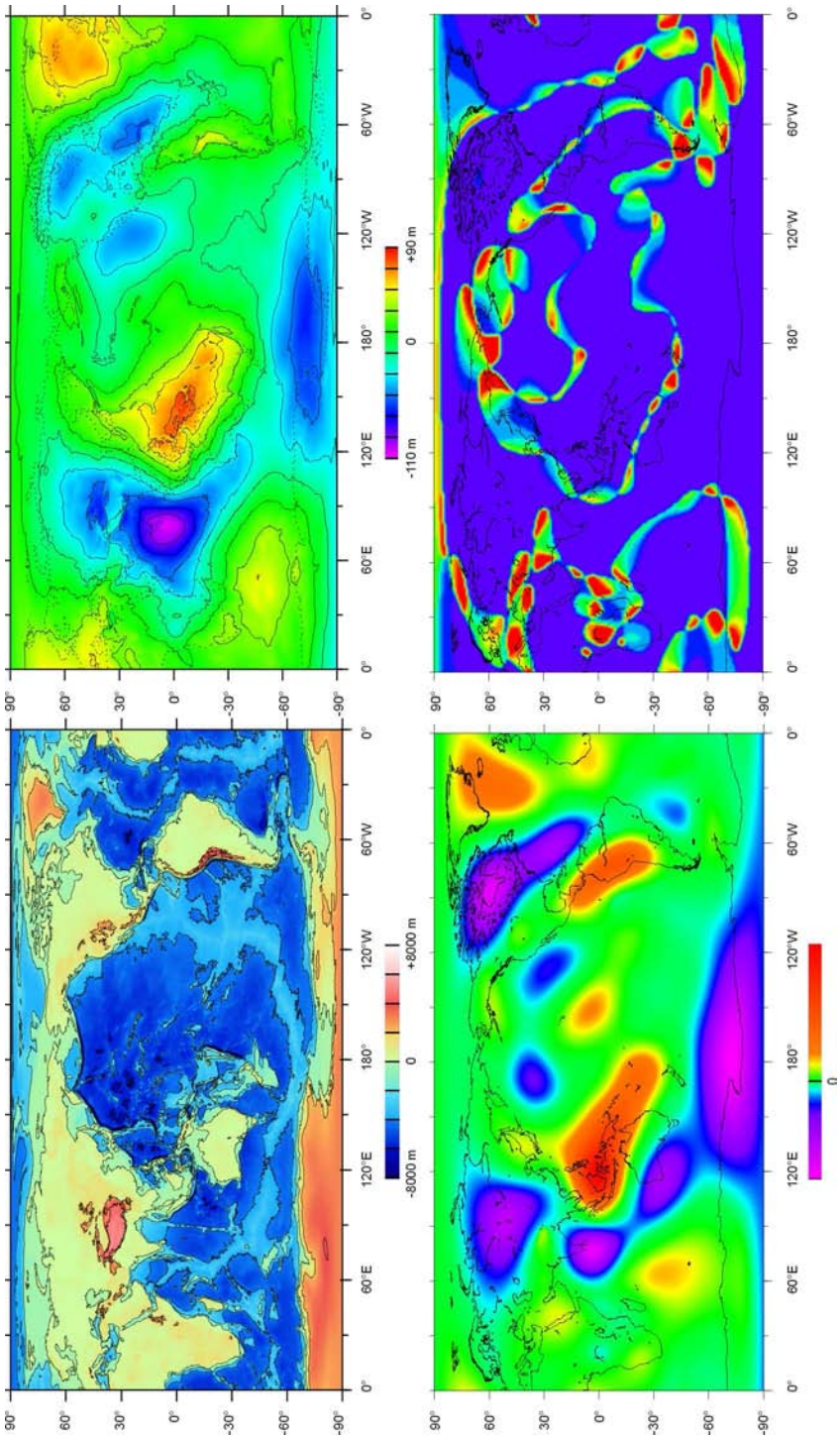

Figure 6.9: At top, the topography and geoid of Earth, at bottom the E_{max} and k_{max} maps of the geoid for j_w=08-16. In this case the contribution of dynamic processes is even more evident than in the case of Venus because of the mismatch with the continental masses

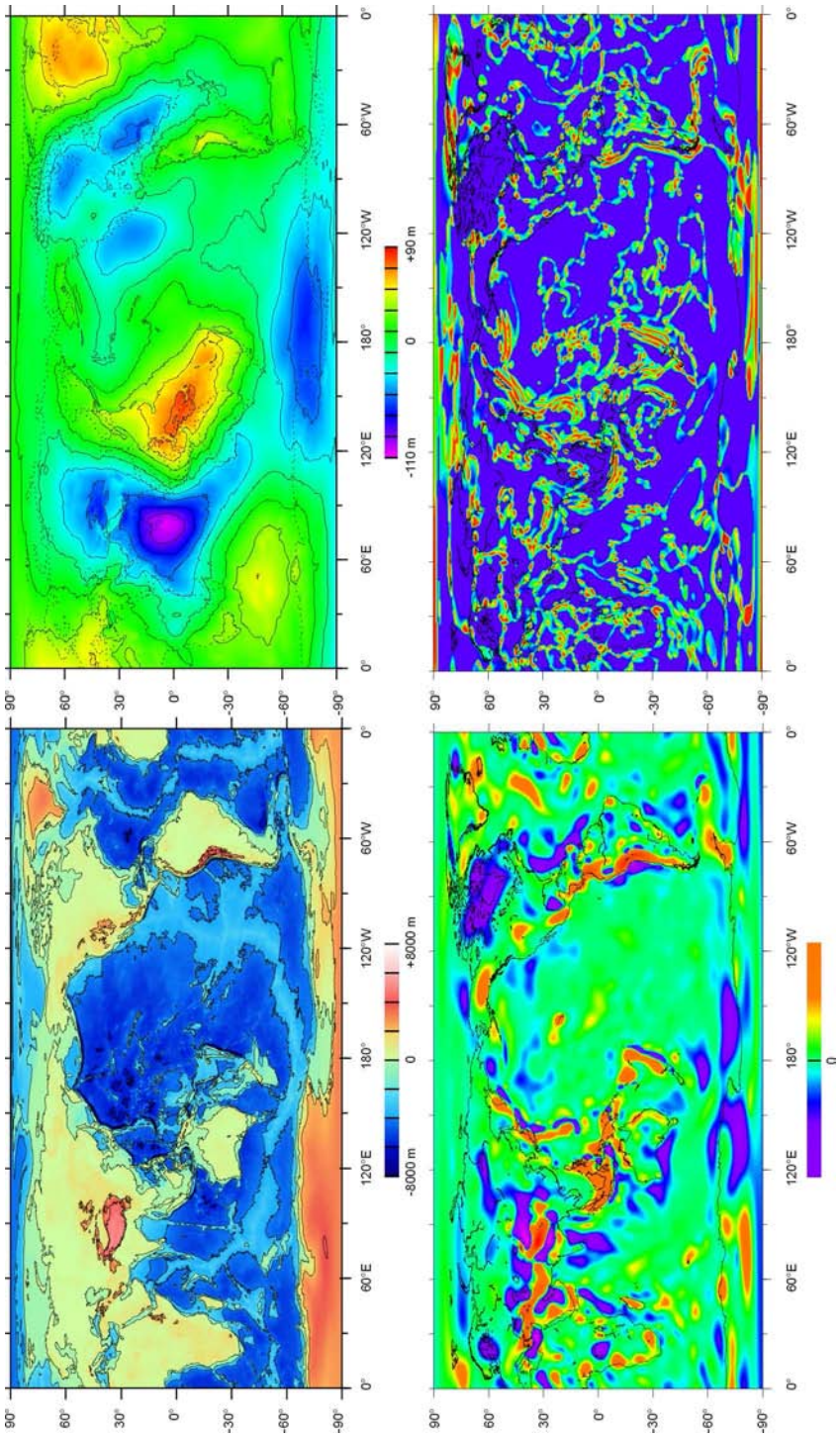

Figure 6.10: At top, the topography and geoid of Earth, at bottom the E_{max} and k_{max} maps of the geoid for j_w=32-64. Most contributions can be assigned to the prominent surface or oceanic topographic or tectonic structures

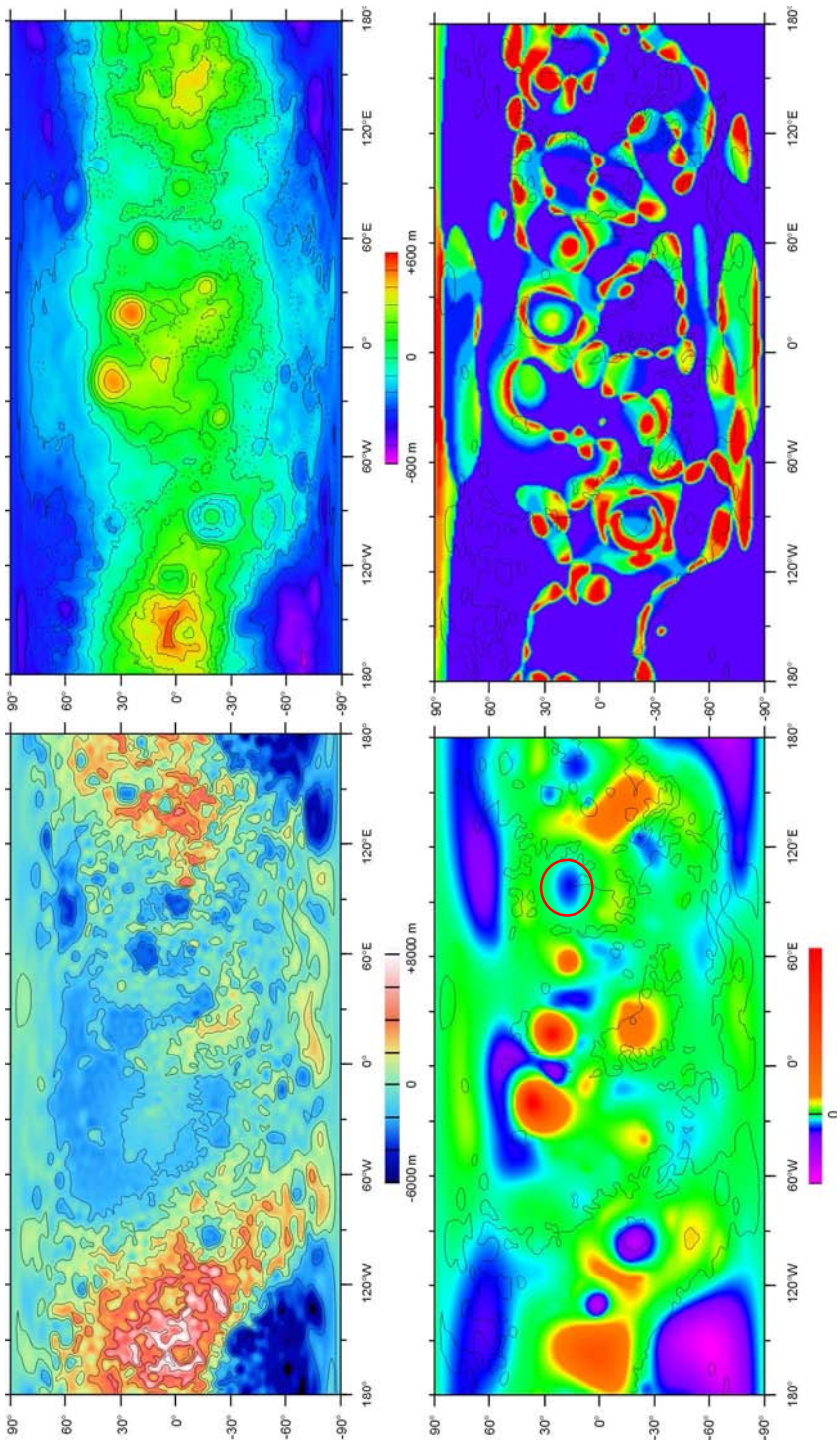

Figure 6.11: At top, the topography and geoid of the Moon, at bottom the E_{max} and k_{max} maps of the geoid for j_w=08-16. We can observe mainly topographic and mascons' signal however a prominent anomaly not directly connected to these could be found (circled)

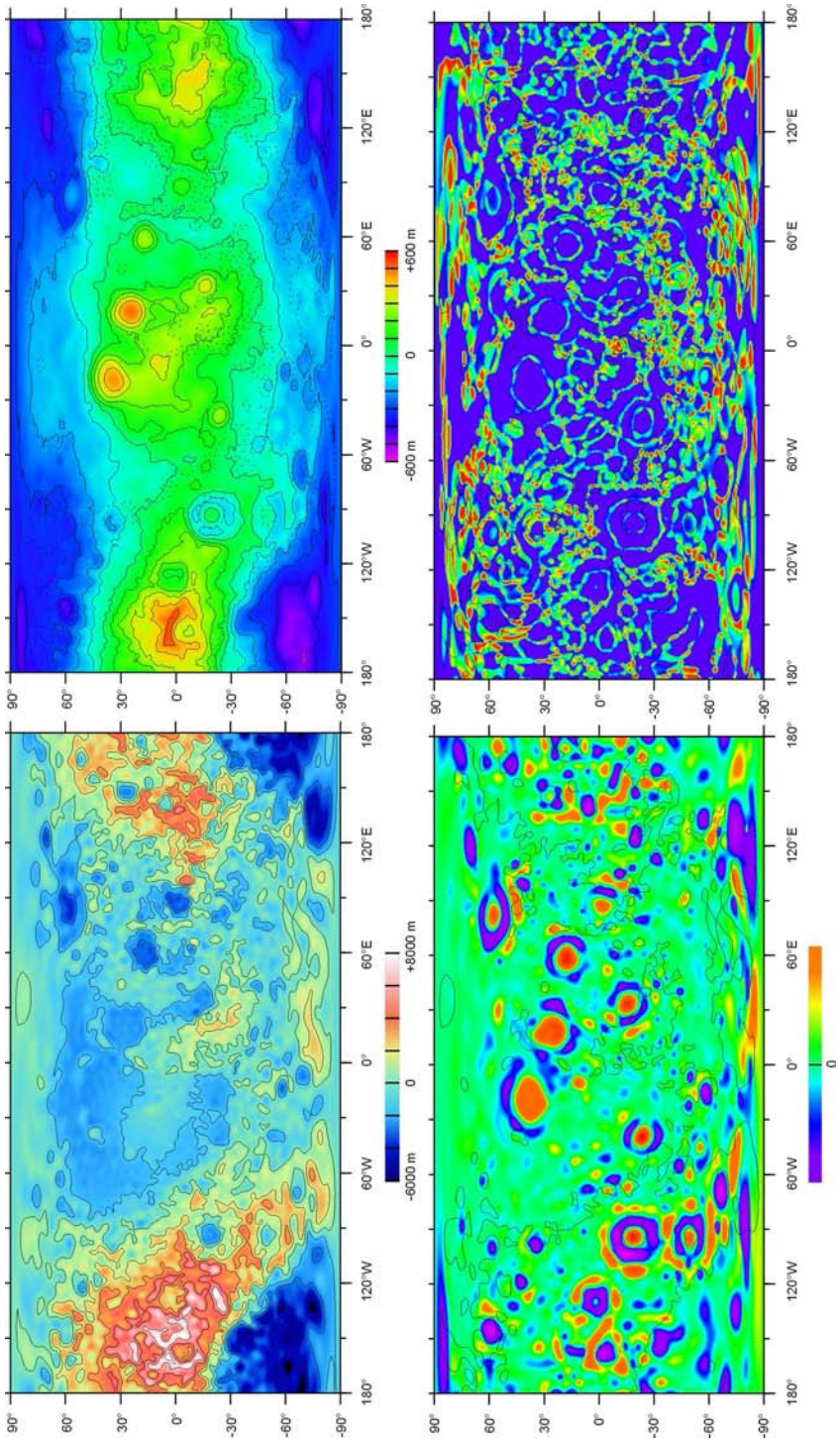

Figure 6.12: At top, the topography and geoid of the Moon, at bottom the E_{max} and k_{max} maps of the geoid for j_w=32-64. Here the mascons' signal is dominant with clearly observable rims of mare basins and major craters

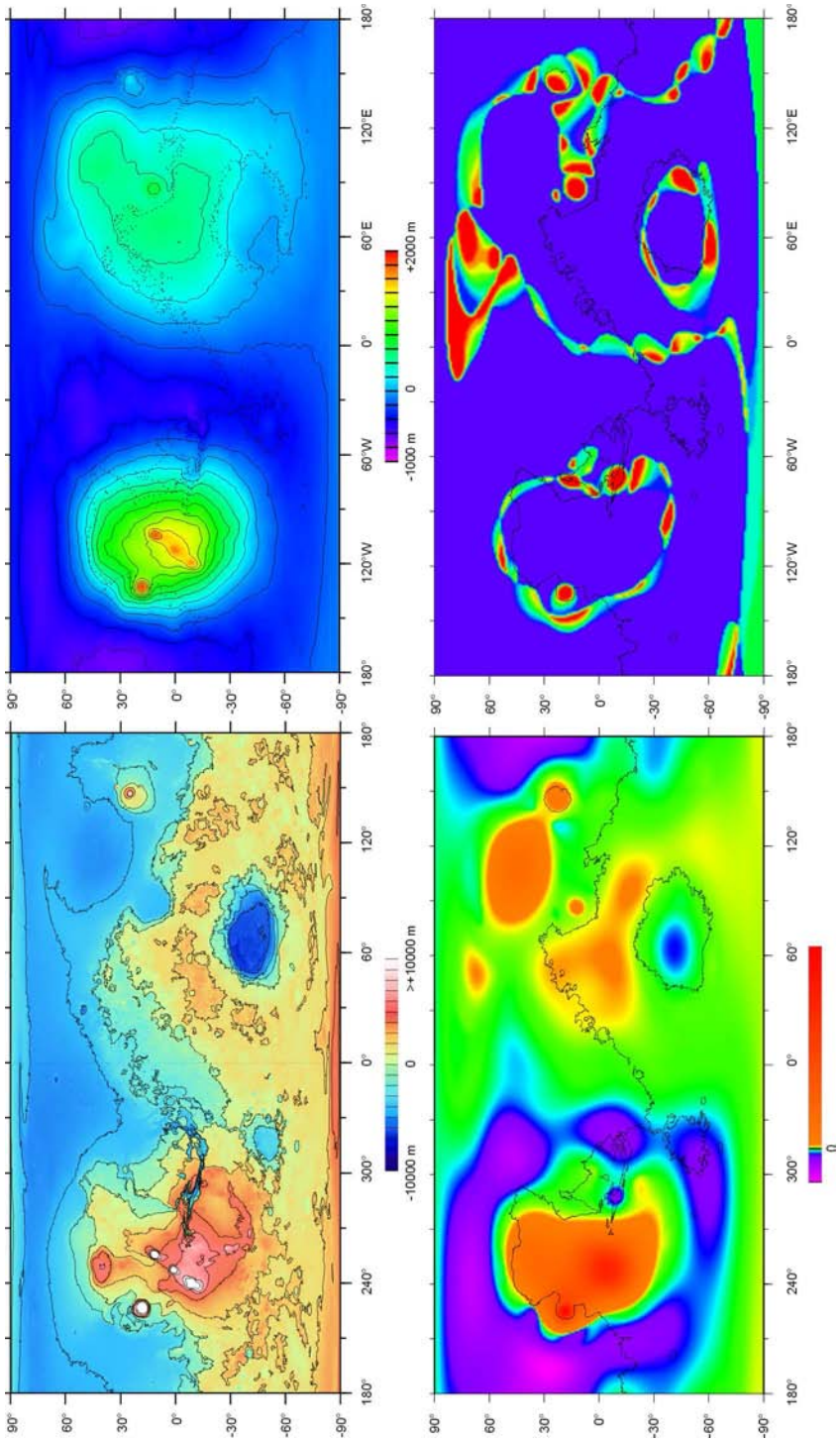

Figure 6.13: At top, the topography and geoid of Mars, at bottom the E_{max} and k_{max} maps of the geoid for j_w=08-16. Here the dominance by Tharsis and Utopia Planitia is obvious however some complex signal of other structures is observed

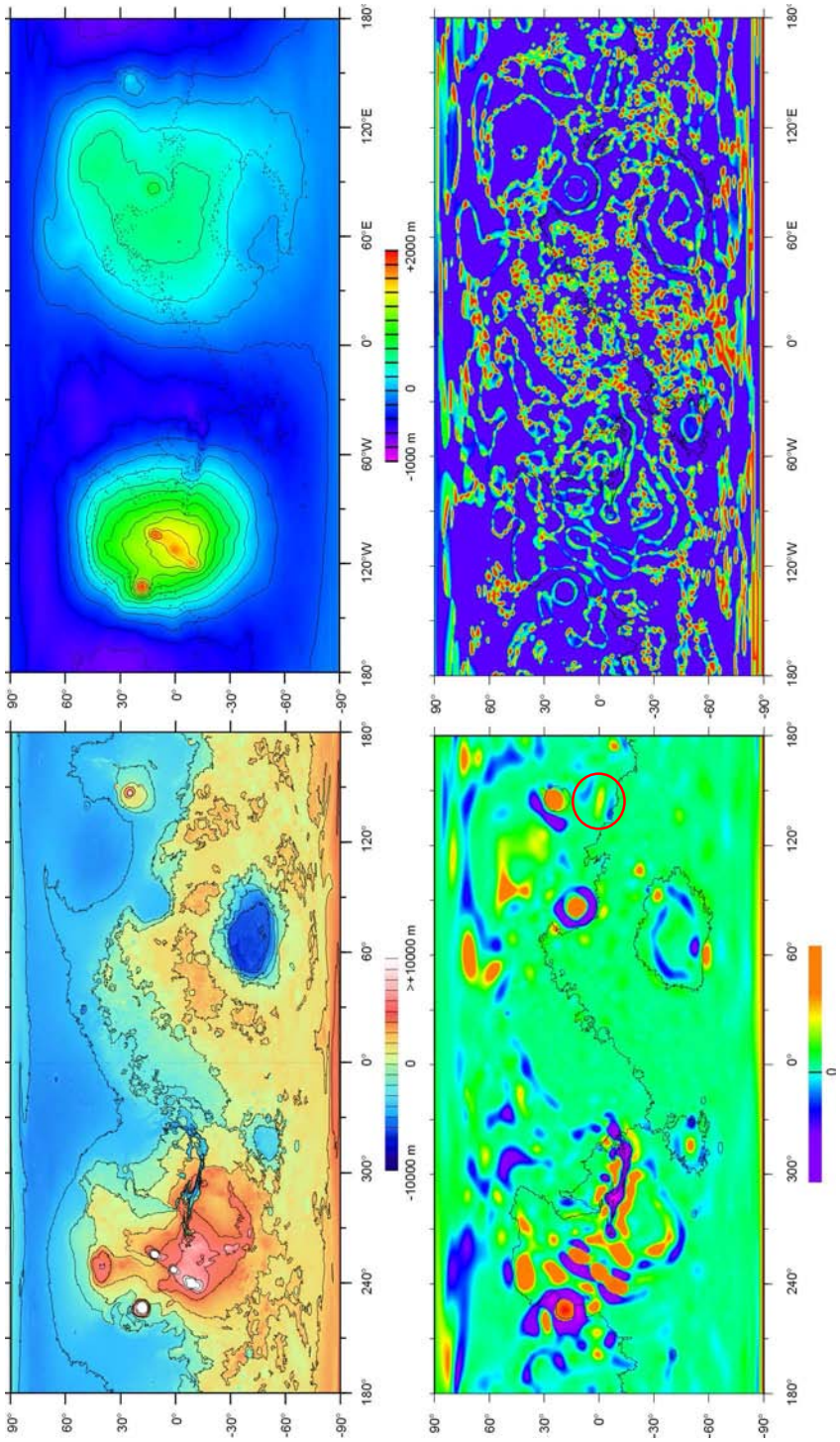

Figure 6.14: In upper part the topography and geoid of Mars, in lower one E_{max} and k_{max} maps of geoid for j_w=32-64. We can examine the signal of well known tectonic and impact features together with some not yet well-known (circled)

Chapter 7

Discussion of Results

Our research was done on global planetary scale and thus results obtained by the used inverse method should tell us important facts about general tendencies of Venus' structure. However lack of any direct observational data from the venusian interior can put our findings into question – so an appropriate final step is to compare and discuss them with the results of forward models mainly performed previously by others.

Our analysis of the crustal structure is based on global data and so the individual site examination could differ slightly from a derived average compensation depth of 35 km. However even local admittance studies (Simons et al., 1997) are in agreement with our findings and predict for exclusive locations like Beta Regio, Niobe Planitia or Lakshmi Planum very close values of crustal thickness. The earlier estimates of a global value (Arkani-Hamed, 1996) could differ slightly because of the use of older gravity and topography models. Also the localization of the observed and predicted geoid done in the previous section (Fig. 6.2) confirms that, in the case of no longer active regions at Venus, the inferred compensation depth could well predict the observed data.

On the other hand for the long and intermediate wavelengths the dynamic flow model of Venus' mantle predicts a geoid and topography in very close agreement with the observed values as noted earlier by several authors (Kiefer et al., 1986; Phillips, 1990; Simons et al., 1997). So the inverse problem based on this technique could gives us important answers about the mantle rheology. The test of resolution of our inverse problem formulation confirms that we can detect some major subsurface features, though with certain limits in obtaining the unambiguous values.

The three main results obtained (stiffer lithosphere overlaying the mantle, lack of the low-viscosity zone – LVZ – and a gradual increase of viscosity through the mantle by order 1-1.5 magnitude) are in agreement not only with papers dealing with Venus' interior but also with some authors studying general states of convection in the case of systems with missing mobile plate tectonics. A viscosity contrast by at least 3 orders of magnitude from the lithosphere to the rest of the mantle and a lack of LVZ in a site of some major plumes were shown by a regional modelling (Kiefer and Hager, 1991; Kiefer and Hager, 1992) and also indicated by some global convection studies (Dubuffet et al., 2000; Stein and Hansen, 2003). A common implication from these findings is that venusian rheology

is dryer, which is caused mainly by the early water escape (Donahue and Hodges, 1992) and therefore the plate tectonics could not evolve without an underlaying LVZ. Some others however (e.g. Simons et al., 1997), are assuming that a determination of the presence of an LVZ on Venus is out of our current knowledge. The viscosity increase through the mantle used to sometimes be neglected (Venus's mantle is then handled as isoviscose) and sometimes interpreted as a upper/lower mantle boundary – but our results do not indicate such a sharp contrast, rather we explain it in terms of a monotonous viscosity rise.

The question of lithospheric thickness remains only partially answered because the dynamic predictions are based on long wavelengths and are not very sensitive to shallow viscosity structures. But the basic result is between 100-200 km which corresponds also with an isostasy compensation model for the whole spectrum j=2-90 which gives ADC around 165 km. This is in agreement with some of the estimates of lithospheric thickness (e.g. Nimmo and McKenzie, 1998) despite some other authors (e.g. Solomatov and Moresi, 1996) putting the bottom of the lithosphere at depths 200-400 km. It's not clear if this parameter could be definitely derived from our present knowledge for example by regional modelling (see discussion in Nimmo and McKenzie, 1998) or if we have to wait until some in-situ seismological measurements are done.

Also interesting for our investigation is the correspondence between the inducing density perturbation power spectrum for wavelengths j=2-40 (Fig. 5.8 right) and observed tomography power spectrum (e.g. Čížková et al., 1996). The linear tendency on the logarithmic scale at intermediate wavelengths also appears in the averaged horizontal power spectra of temperature from time-dependent convection of Newtonian fluid (Larsen et al., 1995). The similarity to our results brakes up around degree 40 (Fig. 5.8, right of the dashed line) which is also the interface between dynamic and isostatic theory use. From that we can also conclude a the suitability of our dynamic flow model.

Chapter 8

Conclusions

In our search for a geoid generated primarily by dynamic processes in the mantle of Venus we have to first separate the contribution of isostatic support of topography. For this the isostatic hypothesis seems to predict the observed data successfully and both inverse problem formulations used (for degree apparent depth of compensation and fitting the degree admittance function) are steady and give the same results. However the obtained apparent depth of compensation 35 km is only an averaged global approximation, the local crustal thickness can vary from that significantly.

Our work seems to exploit the theme of dynamic support of topography which has already been taken by many others. Nevertheless the unknown density distribution limits such models and they can answer only questions regarding basic mantle properties. Our density approximation of only lateral variations constant with depth is one of the possible ways to overcome these difficulties. The inverse problem based on such a density model and internal loading theory appears to be steady for small number of free parameters, as their number increase, the solution gets less robust. Hence the major obtained results:

- the existence of a stiff lithosphere with a viscosity higher by several orders of magnitude than the underlaying mantle
- the absence of a narrow low viscosity zone (similar to Earth's asthenosphere) beneath the lithosphere
- the gradual increase of viscosity through the mantle by 1-1.5 orders of magnitude

have an importance as a guiding solution showing the general trends in Venus' mantle. All of these findings were already introduced by other authors but never before by means of a well defined inverse problem and all together. Our contribution is therefore the confirmation of these results and the compilation of them into a coherent model. For better resolution of the rheology of the deep mantle another approach, following new data, would be necessary.

The use of localization methods appears to be another efficient tool in comparing and analyzing spatial geophysical fields. For our purposes it has been the way to overcome the disadvantages of the global character of the spherical harmonic approach and can be used for both field analysis and local-spectral studies. The E_{max}-k_{max} method combines

both the spatial analytic and the synthetic approaches and despite certain mathematical disadvantages seems to be a valuable tool in the examination of planetary gravity fields.

As mentioned in the previous paragraph, our effort to determine the subsurface structure and mantle rheology is strongly limited by the unknown density distribution beneath the venusian surface. The current knowledge of Venus' geophysics, the collected data and their analysis cannot give us a satisfactory answer to this problem, and so we see the importance of future space missions focused on detailed geophysical exploration for the sake of better understanding planetary formation and evolution.

Appendix A

Spherical Harmonics

In many geophysical problems we need to describe spherical fields by means of scale-varying global functions. A very useful tool is to employ spherical harmonic (SH) functions which create an orthogonal basis on the sphere. Within this basis we can evaluate either scalar, vector or tensor fields to an appropriate set of coefficients and use it to express some PDE problems as a set of ODE which are easier to solve.

A.1 Scalar Spherical Harmonics

Similar to Fourier decomposition of a continuous signal into a series, the spherical scalar function can be evaluated by the summation of coefficients multiplied by the appropriate basis functions (e.g. Jones, 1985; Varshalovich et al., 1988):

$$f(\vartheta,\varphi)=\sum_{j=0}^{\infty}\sum_{m=-j}^{j}A_{jm}Y_{jm}(\vartheta,\varphi) \tag{A.1}$$

for 2D function f or in the 3D case:

$$f(r,\vartheta,\varphi)=\sum_{j=0}^{\infty}\sum_{m=-j}^{j}A_{jm}(r)Y_{jm}(\vartheta,\varphi), \tag{A.2}$$

where ϑ and φ are the colatitude and longitude respectively, A_{jm} and $A_{jm}(r)$ the appropriate SH coefficients. The basis functions $Y_{jm}(\vartheta,\varphi)$ are defined as follows:

$$\begin{aligned} Y_{jm}(\vartheta,\varphi) &= (-1)^m N_{jm} P_{jm}(\cos\vartheta)e^{im\varphi} \qquad j\geq 0 \quad m\geq 0 & \text{(A.3)}\\ Y_{jm}(\vartheta,\varphi) &= (-1)^m Y^{*}_{j|m|}(\vartheta,\varphi) \qquad\qquad j\geq 0 \quad m<0, & \text{(A.4)} \end{aligned}$$

where the asterisk means complex conjugation, the normalization factor N_{jm} is given by

$$N_{jm}=\left[\frac{(2j+1)}{4\pi}\frac{(j-m)!}{(j+m)!}\right]^{\frac{1}{2}} \tag{A.5}$$

and the P_{jm} in our definition of spherical harmonics are the associated Legendre functions derived from Legendre polynomials P_j:

$$P_{jm}(\cos\vartheta) = (1-\cos^2\vartheta)^{\frac{m}{2}}\frac{d^m P_j(\cos\vartheta)}{d(\cos\vartheta)^m} = \sin^m\vartheta\frac{d^m P_j(\cos\vartheta)}{d(\cos\vartheta)^m} \quad (A.6)$$

$$P_j(x) = \frac{1}{2^j j!}\frac{d^j}{dx^j}(x^2-1)^j. \quad (A.7)$$

Moreover if the function $f \in C^2$ (i.e. the function has a continuous derivative) the series A.1 (resp. A.2) is uniformly convergent and therefore:

$$\lim_{j\to\infty}|f_{jm}| = 0 \quad (A.8)$$

The definitions of spherical harmonics used (A.3 and A.4) satisfy the orthonormality conditions (the δ symbols stands for the Kronecker function $\delta_{jm} = 1$ for the case $j = m$, otherwise it is equal to zero):

$$\int_0^{2\pi}\int_0^{\pi} Y_{jm}(\vartheta,\varphi)Y^*_{kl}(\vartheta,\varphi)\sin\vartheta d\vartheta d\varphi = \delta_{jk}\delta_{ml}. \quad (A.9)$$

To evaluate coefficients A_{jm} – similarly for $A_{jm}(r)$ – we use the decomposition by a dot product of scalar field with the basis functions Y_{jm}:

$$A_{jm} = \int_0^{2\pi}\int_0^{\pi} f(\vartheta,\varphi)Y^*_{jm}(\vartheta,\varphi)\sin\vartheta\, d\vartheta\, d\varphi \quad (A.10)$$

In the case that $f(\vartheta,\varphi)$ is a real function we can evaluate A_{jm}, $m < 0$ using the symmetry from equation A.4 in relation A.10:

$$A_{j,-m} = (-1)^m A^*_{jm}. \quad (A.11)$$

A.1.1 Applications

To calculate $|f_j|^2$ – the power spectra of SH coefficients – to estimate the contribution of different wavelength features we use the following expression or, in the case of a real function f, its symmetric modification according to equation A.11.

$$|f_j|^2 = \sum_{m=-j}^{j} f_{jm}f^*_{jm}. \quad (A.12)$$

Another useful tool to investigate the global characteristic is a degree-correlation function c_j, which gives the information about the similarity between two SH fields (e.g. between geoid g_{jm} and topography t_{jm}) at various scales:

$$c_j = \frac{\sum_{m=-j}^{j} g_{jm}t^*_{jm}}{\sqrt{\sum_{m=-j}^{j} g_{jm}g^*_{jm}}\sqrt{\sum_{m=-j}^{j} t_{jm}t^*_{jm}}}. \quad (A.13)$$

If we want to evaluate a transfer degree-ratio between two SH fields we can use the admittance function a_j, which represents the part of the field correlated with the other one – whereas the uncorrelated part is represented by u_{jm} (e.g. SCHUBERT ET AL., 2001):

$$g_{jm} = a_j t_{jm} + u_{jm} \tag{A.14}$$

$$a_j = \frac{\sum_{m=-j}^{j} t_{jm} g^*_{jm}}{\sum_{m=-j}^{j} t_{jm} t^*_{jm}}. \tag{A.15}$$

Considering Newton's gravity law the gravity signal at point $\boldsymbol{r}$ of mass distributed inside the sphere Ω' could be evaluated in the form of the gravitational potential $V(\boldsymbol{r})$:

$$V(\boldsymbol{r}) = \kappa \int_{\Omega'} \frac{\rho(\boldsymbol{r}')}{|\boldsymbol{r} - \boldsymbol{r}'|} \, d\Omega'. \tag{A.16}$$

In geophysics, rather than with the geopotential, we work with the geoid, though these terms are nearly equivalent. The geoid height at any point on the surface located at (ϑ, φ) is then given (considering a local gravity acceleration g_0) by the following equation:

$$g(\vartheta, \varphi) = \frac{V(\vartheta, \varphi)}{g_0(\vartheta, \varphi)}. \tag{A.17}$$

For our purposes we need to transform an equation A.16 into a SH form hence we must first transform the density ρ and the relative vector $\frac{1}{|\boldsymbol{r}-\boldsymbol{r}'|}$ terms:

$$\rho(\boldsymbol{r}') = \sum_{j=0}^{\infty} \sum_{m=-j}^{j} \rho_{jm}(r') Y_{jm}(\vartheta', \varphi') \tag{A.18}$$

$$\frac{1}{|\boldsymbol{r} - \boldsymbol{r}'|} = \frac{4\pi}{r} \sum_{k=0}^{\infty} \sum_{l=-k}^{k} \frac{1}{2k+1} \left(\frac{r'}{r}\right)^k Y^*_{kl}(\vartheta', \varphi') Y_{kl}(\vartheta, \varphi), \quad r \geq r' \tag{A.19}$$

which allow us to write equation A.16 in the form:

$$\begin{aligned} V(\boldsymbol{r}) &= \kappa \int_{\Omega'} \sum_{j,m} \sum_{k,l} \frac{4\pi}{r} \frac{1}{2k+1} \left(\frac{r'}{r}\right)^k \rho_{jm}(r') Y_{jm}(\vartheta', \varphi') Y^*_{kl}(\vartheta', \varphi') \times \\ &\times Y_{kl}(\vartheta, \varphi) r'^2 \sin\vartheta' d\vartheta' d\varphi' dr'. \end{aligned} \tag{A.20}$$

Using orthonormality relation A.9 we can simplify the previous equation into:

$$V(\boldsymbol{r}) = \frac{4\pi\kappa}{r} \sum_{j=0}^{\infty} \sum_{m=-j}^{j} \frac{1}{2j+1} \int_{r_1'}^{r_2'} \left(\frac{r'}{r}\right)^j \rho_{jm}(r') Y_{jm}(\vartheta, \varphi) r'^2 dr'. \tag{A.21}$$

When we want to apply the derived formula A.21 to the geopotential measured at the surface of planet then $r = R$ (the planetary radius) and we obtain:

$$V(\boldsymbol{r}) = \frac{4\pi\kappa}{R}\sum_{j=0}^{\infty}\sum_{m=-j}^{j}\frac{1}{2j+1}\Big[\int_0^R\Big(\frac{r'}{R}\Big)^j\rho_{jm}(r')r'^2dr'\Big]Y_{jm}(\vartheta,\varphi). \tag{A.22}$$

Because we want to get a SH series in the form

$$V(\boldsymbol{r}) = \sum_{j=0}^{\infty}\sum_{m=-j}^{j}V_{jm}(R)Y_{jm}(\vartheta,\varphi), \tag{A.23}$$

we must define V_{jm} in the following form

$$V_{jm}(R) = \frac{4\pi\kappa}{R}\frac{1}{2j+1}\int_0^R\Big(\frac{r'}{R}\Big)^j\rho_{jm}(r')r'^2dr'. \tag{A.24}$$

If we want to evaluate the geopotential contribution of density anomalies caused by topography undulations at given radius ($r' = R_1$) – e.g. at the surface or at MOHO – which could be evaluated as $\rho_{jm}(r') = t_{jm}\Delta\rho\,\delta_{R_1}$, where t_{jm} are SH coefficients of this topography, $\Delta\rho$ is the density contrast and $\delta_{R_1} = 0$ other than at the given depth. Thus we obtain

$$V_{jm}(R) = \frac{4\pi\kappa}{R}\frac{1}{2j+1}\Big(\frac{R_1}{R}\Big)^j t_{jm}\Delta\rho R_1^2 = \frac{4\pi\kappa R}{2j+1}\Big(\frac{R_1}{R}\Big)^{j+2}t_{jm}\Delta\rho \tag{A.25}$$

$$V_{jm}(R) = \frac{4\pi\kappa R}{2j+1}t_{jm}\Delta\rho, \qquad \text{at the surface } R_1 = R. \tag{A.26}$$

Dealing with a topography compensation we need to set the isostasy by the inverse topography s_{jm} at the depth h with amplitudes proportional to density contrast ratio $\frac{\Delta\rho_{surf}}{\Delta\rho_{MOHO}}$:

$$s_{jm} = -t_{jm}\frac{\Delta\rho_{surf}}{\Delta\rho_{MOHO}}, \tag{A.27}$$

therefore the gravitational potential from the compensated surface topography t_{jm} (the sum of the equation A.25 for $R_1 = R, R-h$) with the density contrast $\Delta\rho \doteq \rho_{surf}$ is:

$$V_{jm} = \frac{4\pi\kappa R}{2j+1}\Big(1 - \Big(\frac{(R-h)}{R}\Big)^{j+2}\Big)t_{jm}\Delta\rho. \tag{A.28}$$

If we want then to calculate the least-square misfit function between two SH fields (e.g. between observed and predicted geoid) we will use the following formula

$$S^2 = \sum_{j=0}^{jmax}\sum_{m=-j}^{j}(g_{jm}^{pred} - g_{jm}^{obs})(g_{jm}^{pred} - g_{jm}^{obs})^*. \tag{A.29}$$

However, for some geophysical purposes we may need to express a gravity field instead in the form of a geoid in the form of free-air gravity. This is defined as a radial acceleration at the geoid level (usually measured in mGals):

$$a(R) = \frac{\partial V(r)}{\partial r}\Big|_{r=R}. \tag{A.30}$$

This equation is easy to transform into SH form by considering an appropriate definition of the Earth geopotential

$$V(r,\vartheta,\varphi) = \sum_{j=0}^{\infty}\sum_{m=-j}^{j}\left(\frac{R}{r}\right)^{j+1} V_{jm}(R)Y_{jm}(\vartheta,\varphi). \tag{A.31}$$

Putting A.31 relation into A.30 we obtain

$$V_{jm}(r) = \left(\frac{R}{r}\right)^{j+1} V_{jm}(R) \tag{A.32}$$

$$\frac{\partial V_{jm}(r)}{\partial r} = (j+1)\frac{R^{j+1}}{r^{j+2}} V_{jm}(R) \tag{A.33}$$

$$a_{jm}(R) = \frac{j+1}{R} V_{jm}. \tag{A.34}$$

In the satellite geodesy there are conventional equations for SH expansion of the topography (A.35) and the geopotential (A.36) mostly set by Kaula, 1966:

$$T(\vartheta,\varphi) = R\sum_{j=2}^{\infty}\sum_{m=0}^{j} P_{jm}(\cos\varphi)(C^t_{jm}\cos m\vartheta + S^t_{jm}\sin m\vartheta) \tag{A.35}$$

$$V(\vartheta,\varphi) = \frac{GM}{R} + \frac{GM}{R}\sum_{j=2}^{\infty}\sum_{m=0}^{j} P_{jm}(\cos\varphi)(C^v_{jm}\cos m\vartheta + S^v_{jm}\sin m\vartheta), \tag{A.36}$$

where C^t_{jm}, S^t_{jm} and C^v_{jm}, S^v_{jm} are the corresponding fully normalized SH trigonometric coefficients. Re-normalizing these trigonometric coefficients for un-normalized exponential SH coefficients A_{jm} suitable for use in A.1 or A.2 is simple:

$$A^t_{j0} = R\sqrt{4\pi}(C^t_{jm}) \qquad A^t_{jm} = (-1)^m R\sqrt{2\pi}(C^t_{jm} + iS^t_{jm}) \tag{A.37}$$

$$A^v_{j0} = \frac{GM}{R}\sqrt{4\pi}(C^v_{jm}) \qquad A^v_{jm} = (-1)^m\frac{GM}{R}\sqrt{2\pi}(C^v_{jm} + iS^v_{jm}), \tag{A.38}$$

where GM, R and g_0 are constants needed to evaluate either the topography or gravitational field – for the proper values of the parameters known today (those for Venus, Earth, Moon and Mars) see table 3.1. When using trigonometric coefficients it is common to write the power spectra equation A.12 in a form (e.g. Arkani-Hamed, 1996)

$$RMS_j = \sqrt{\frac{\sum_{m=0}^{j}(C^2_{jm} + S^2_{jm})}{2j+1}} \tag{A.39}$$

A.2 Vector Spherical Harmonics

When considering a vector spherical field we need a proper basis for its description. Instead of using Cartesian $(\boldsymbol{e}_x, \boldsymbol{e}_y, \boldsymbol{e}_z)$ or spherical $(\boldsymbol{e}_r, \boldsymbol{e}_\vartheta, \boldsymbol{e}_\varphi)$ unit vectors we use so called cyclic unit vectors $\boldsymbol{e}_\mu$ $(\mu = -1, 0, 1)$, which are constructed in the following way

$$\boldsymbol{e}_1 = -\frac{1}{\sqrt{2}}(\boldsymbol{e}_x + i\boldsymbol{e}_y) \tag{A.40}$$

$$\boldsymbol{e}_0 = \boldsymbol{e}_z \tag{A.41}$$

$$\boldsymbol{e}_{-1} = \frac{1}{\sqrt{2}}(\boldsymbol{e}_x - i\boldsymbol{e}_y) \tag{A.42}$$

and have these properties

$$\boldsymbol{e}_\mu^* = (-1)^\mu \boldsymbol{e}_{-\mu} \tag{A.43}$$

$$\boldsymbol{e}_\mu^* \cdot \boldsymbol{e}_{\mu'} = (-1)^\mu \boldsymbol{e}_{-\mu} \cdot \boldsymbol{e}_{\mu'} = \delta_{\mu\mu'}. \tag{A.44}$$

The scalar spherical harmonic series from the previous section could be adapted to the vector case by adding one dimension to the used basis functions. Therefore the 2D or 3D (respectively) vector functions can be written in the form:

$$\boldsymbol{f}(\vartheta, \varphi) = \sum_{j=0}^{\infty} \sum_{m=-j}^{j} \sum_{l=|j-1|}^{j+1} A_{jm}^l \, \boldsymbol{Y}_{jm}^l(\vartheta, \varphi) \tag{A.45}$$

$$\boldsymbol{f}(r, \vartheta, \varphi) = \sum_{j=0}^{\infty} \sum_{m=-j}^{j} \sum_{l=|j-1|}^{j+1} A_{jm}^l(r) \, \boldsymbol{Y}_{jm}^l(\vartheta, \varphi), \tag{A.46}$$

where $\boldsymbol{Y}_{jm}^l$ are the vector spherical harmonic functions. This vector canonic basis – which is in fact a tensor basis A.58 for a case k=1 (this is omitted in the superscript, could be written also as $\boldsymbol{Y}_{jm}^{l1}$) – is defined in the following way (see e.g. Edmonds, 1960):

$$\boldsymbol{Y}_{jm}^l(\vartheta, \varphi) = \sum_{\mu=-1}^{1} \sum_{\nu=-l}^{l} C_{l\nu 1\mu}^{jm} Y_{l\nu}(\vartheta, \varphi) \boldsymbol{e}_\mu \tag{A.47}$$

where $C_{l\nu 1\mu}^{jm}$ are Clebsh-Gordan coefficients (e.g. Varshalovich et al., 1988). Alternatively the vector spherical harmonic functions could be defined by use of the spherical basis $(\boldsymbol{e}_r, \boldsymbol{e}_\vartheta, \boldsymbol{e}_\varphi)$:

$$\sqrt{j(2j+1)}\, \boldsymbol{Y}_{jm}^{j-1}(\vartheta, \varphi) = jY_{jm}(\vartheta, \varphi)\boldsymbol{e}_r + \frac{\partial Y_{jm}(\vartheta, \varphi)}{\partial \vartheta}\boldsymbol{e}_\vartheta + \frac{1}{\sin\vartheta}\frac{\partial Y_{jm}(\vartheta, \varphi)}{\partial \varphi}\boldsymbol{e}_\varphi \tag{A.48}$$

$$\sqrt{j(j+1)}\, \boldsymbol{Y}_{jm}^{j}(\vartheta, \varphi) = i\frac{1}{\sin\vartheta}\frac{\partial Y_{jm}(\vartheta, \varphi)}{\partial \varphi}\boldsymbol{e}_\vartheta - i\frac{\partial Y_{jm}(\vartheta, \varphi)}{\partial \vartheta}\boldsymbol{e}_\varphi \tag{A.49}$$

$$\sqrt{(j+1)(2j+1)}\, \boldsymbol{Y}_{jm}^{j+1}(\vartheta, \varphi) = -(j+1)Y_{jm}(\vartheta, \varphi)\boldsymbol{e}_r + \frac{\partial Y_{jm}(\vartheta, \varphi)}{\partial \vartheta}\boldsymbol{e}_\vartheta + \frac{1}{\sin\vartheta}\frac{\partial Y_{jm}(\vartheta, \varphi)}{\partial \varphi}\boldsymbol{e}_\varphi. \tag{A.50}$$

The appropriate SH coefficients f^l_{jm} (resp. $f^l_{jm}(r)$) can be derived by a modification of equation A.10 in the sense of term A.45:

$$f^l_{jm} = \int_0^{\pi} \int_0^{2\pi} \boldsymbol{f}(\vartheta,\varphi) \cdot \boldsymbol{Y}^{l\ *}_{jm}(\vartheta,\varphi) \sin\vartheta \, d\vartheta d\varphi. \tag{A.51}$$

Because of the symmetries of Clebsh-Gordan coefficients we can again evaluate both $\boldsymbol{Y}^l_{j,-m}$ and therefore even $f^l_{j,-m}$ by using the terms with $m \geq 0$:

$$\boldsymbol{Y}^l_{j,-m} = (-1)^{j+m+l+1} \boldsymbol{Y}^{l\ *}_{jm} \tag{A.52}$$

$$f^l_{j,-m} = (-1)^{j+m+l+1} f^{l\ *}_{jm} \tag{A.53}$$

Such basis functions defined by term A.47 (resp. by equations A.48-A.50) satisfy the condition of orthonormality:

$$\int_0^{\pi} \int_0^{2\pi} \boldsymbol{Y}^{l_1}_{j_1 m_1}(\vartheta,\varphi) \cdot \boldsymbol{Y}^{l_2\ *}_{j_2 m_2}(\vartheta,\varphi) \sin\vartheta \, d\vartheta d\varphi = \delta_{j_1 j_2} \delta_{m_1 m_2} \delta_{l_1 l_2}. \tag{A.54}$$

Moreover it could be shown that the field on the sphere can be separated into a *toroidal* part which describes only horizontal changes ($\nabla . v_T = 0$ and $v_T . e_r = 0$) and a *spheroidal* part ($(\nabla . \times v_S) . e_r = 0$ – when we deal with the non-divergence field i.e. $\nabla . v = 0$ then this part is called *poloidal*). The $f^{j\pm1}_{jm}$ coefficients then represent the spheroidal and f^j_{jm} the toroidal part of the field $\boldsymbol{f}$ (e.g. Matas, 1995).

A.3 Tensor Spherical Harmonics

If we have a spherical field of tensor quantity we can adapt the cyclic basis (A.40-A.42) to obtain a tensor orthogonal one:

$$\boldsymbol{E}_{k\lambda} = \sum_{\mu=-1}^{1} \sum_{\nu=-1}^{1} C^{k\lambda}_{1\mu 1\nu} \boldsymbol{e}_\mu \boldsymbol{e}_\nu. \tag{A.55}$$

With an appropriate basis function we can again write a series for SH expansion of a spherical field – this time the 2D or 3D tensor one:

$$\boldsymbol{F}(\vartheta,\varphi) = \sum_{j=0}^{\infty} \sum_{m=-j}^{j} \sum_{l=|j-1|}^{j+1} \sum_{k=0}^{2} A^{lk}_{jm} \boldsymbol{Y}^{lk}_{jm}(\vartheta,\varphi) \tag{A.56}$$

$$\boldsymbol{F}(r,\vartheta,\varphi) = \sum_{j=0}^{\infty} \sum_{m=-j}^{j} \sum_{l=|j-1|}^{j+1} \sum_{k=0}^{2} A^{lk}_{jm}(r) \boldsymbol{Y}^{lk}_{jm}(\vartheta,\varphi) \tag{A.57}$$

where the spherical harmonic functions $\boldsymbol{Y}^{kl}_{jm}$ are defined (e.g. Varshalovich et al., 1988) by:

$$\boldsymbol{Y}^{lk}_{jm}(\vartheta,\varphi) = \sum_{\mu=-l}^{l} \sum_{\nu=-k}^{k} C^{jm}_{l\nu k\mu} Y_{l\nu}(\vartheta,\varphi) \boldsymbol{E}_{k\mu}, \tag{A.58}$$

and again satisfy the orthogonality relation:

$$\int_0^{\pi}\int_0^{2\pi} \boldsymbol{Y}_{j_1m_1}^{l_1k_1}(\vartheta,\varphi) : \boldsymbol{Y}_{j_2m_2}^{l_2k_2\,*}(\vartheta,\varphi)\sin\vartheta\, d\vartheta d\varphi = \delta_{j_1j_2}\delta_{m_1m_2}\delta_{l_1l_2}\delta_{k_1k_2}, \tag{A.59}$$

where : operator denotes the double-dot product (for second order tensors with components A_{ij} and B_{ij} is defined as $\boldsymbol{A} : \boldsymbol{B} = \sum\sum A_{ij}B_{ij}$). Moreover such an orthonormal basis has a straight-forward interpretation: the coefficients F_{jm}^{l0} represents the trace of the tensor function, F_{jm}^{l1} stands for the antisymmetric and F_{jm}^{l2} for the symmetric deviatoric part of the tensor function $\boldsymbol{F}$. The evaluation of these coefficients is again only a modification of previous relations A.10 and A.51:

$$f_{jm}^{lk} = \int_0^{\pi}\int_0^{2\pi} \boldsymbol{F}(\vartheta,\varphi) : \boldsymbol{Y}_{jm}^{lk\,*}(\vartheta,\varphi)\sin\vartheta\, d\vartheta d\varphi. \tag{A.60}$$

A.4 Operations with Spherical Harmonics

In this section various products of spherical harmonics and others operations are listed – some of them are used in Appendix C, others could be useful in dealing with differential equations in the form of SH expansions. Most of the formulae are from Varshalovich et al., 1988; Matas, 1995 and the rest came from Čadek, personal communication.

Products of spherical harmonic

$$\begin{aligned}
Y_{j_1m_1}Y_{j_2m_2} &= \frac{\Pi_{j_1j_2}}{\sqrt{4\pi}}\sum_{jm}\frac{1}{\Pi_j}C_{j_10j_20}^{j0}C_{j_1m_1j_2m_2}^{jm}Y_{jm} \\
Y_{j_1m_1}\,\boldsymbol{Y}_{j_2m_2}^{l_2} &= \frac{\Pi_{j_1j_2l_2}}{\sqrt{4\pi}}\sum_{jml}(-1)^{j+l+1}\,C_{j_10\;l_20}^{l0}\,C_{j_1m_1\;j_2m_2}^{jm}\begin{Bmatrix} j & j_1 & j_2 \\ l_2 & 1 & l\end{Bmatrix}\boldsymbol{Y}_{jm}^{l} \\
\boldsymbol{Y}_{j_1m_1}^{l_1}\cdot\boldsymbol{Y}_{j_2m_2}^{l_2} &= (-1)^{j_2+l_2}\frac{\Pi_{j_1j_2l_1l_2}}{\sqrt{4\pi}}\sum_{jm}\frac{1}{\Pi_j}\,C_{l_10\;l_20}^{j0}\,C_{j_1m_1\;j_2m_2}^{jm}\begin{Bmatrix} j_1 & j_2 & j \\ l_2 & l_1 & 1\end{Bmatrix}Y_{jm} \\
\boldsymbol{Y}_{j_1m_1}^{l_1}\times\boldsymbol{Y}_{j_2m_2}^{l_2} &= \frac{i\sqrt{3}}{\sqrt{2\pi}}\,\Pi_{j_1j_2l_1l_2}\sum_{jml}C_{l_10\;l_20}^{l0}\,C_{j_1m_1\;j_2m_2}^{jm}\begin{Bmatrix} j & j_1 & j_2 \\ l & l_1 & l_2 \\ 1 & 1 & 1\end{Bmatrix}\boldsymbol{Y}_{jm}^{l} \\
\boldsymbol{Y}_{j_1m_1}^{l_1}\,\boldsymbol{Y}_{j_2m_2}^{l_2} &= \frac{\Pi_{j_1j_2l_1l_2}}{\sqrt{4\pi}}\sum_{jmln}\Pi_n\,C_{l_10\;l_20}^{l0}\,C_{j_1m_1\;j_2m_2}^{jm}\begin{Bmatrix} j & l & n \\ j_l & l_1 & 1 \\ j_2 & l_2 & 1\end{Bmatrix}\boldsymbol{Y}_{jm}^{ln} \\
\boldsymbol{Y}_{j_1m_1}^{l_1n_1} : \boldsymbol{Y}_{j_2m_2}^{l_2n_2} &= \delta_{n_1n_2}(-1)^{j_2+l_2}\frac{\Pi_{j_1j_2l_1l_2}}{\sqrt{4\pi}}\sum_{jm}\frac{1}{\Pi_j}\,C_{l_10\;l_20}^{j0}\,C_{j_1m_1\;j_2m_2}^{jm}\begin{Bmatrix} n_1 & l_1 & j_1 \\ j & j_2 & l_2\end{Bmatrix}Y_{jm}
\end{aligned}$$

$$\boldsymbol{Y}^{l_1}_{j_1m_1} \cdot \boldsymbol{Y}^{l_2n_2}_{j_2m_2} = (-1)^{n_2+1} \frac{\Pi_{j_1j_2l_1l_2n_2}}{\sqrt{4\pi}} \sum_{jml} C^{l0}_{l_10\ l_20}\, C^{jm}_{j_1m_1\ j_2m_2} \left\{ \begin{array}{ccc} j & j_1 & j_2 \\ l & l_1 & l_2 \\ 1 & 1 & n_2 \end{array} \right\} \boldsymbol{Y}^{l}_{jm}$$

$$\boldsymbol{Y}^{l_1n_1}_{j_1m_1} \cdot \boldsymbol{Y}^{l_2}_{j_2m_2} = (-1)^{n_1+1} \frac{\Pi_{j_1j_2l_1l_2n_1}}{\sqrt{4\pi}} \sum_{jml} C^{l0}_{l_10\ l_20}\, C^{jm}_{j_1m_1\ j_2m_2} \left\{ \begin{array}{ccc} j & j_1 & j_2 \\ l & l_1 & l_2 \\ 1 & n_1 & 1 \end{array} \right\} \boldsymbol{Y}^{l}_{jm}$$

where the $\Pi_{j_1j_2\ldots j_n} = \prod_{i=1}^{n} \sqrt{2j_i+1}$, the term $\{^{j_1\ j_2\ j}_{l_1\ l_2\ l}\}$ stands for 6-j Wigner symbol whereas the similar one constituted of 3 lines for 9-j Wignal symbol. The definitions of these symbols are given e.g. in VARSHALOVICH ET AL., 1988 and their properties are handled later in this section.

FORMULAE FOR PRODUCTS OF A UNIT RADIAL VECTOR AND SPHERICAL TENSORS

$$\boldsymbol{e}_r Y_{jm} = \frac{1}{\sqrt{2j+1}} \left(\sqrt{j}\ \delta_{l,j-1} - \sqrt{j+1}\ \delta_{l,j+1}\right)\ \boldsymbol{Y}^{l}_{jm}$$

$$\boldsymbol{e}_r \cdot \boldsymbol{Y}^{l}_{jm} = \frac{1}{\sqrt{2j+1}} \left(\sqrt{j}\ \delta_{l,j-1} - \sqrt{j+1}\ \delta_{l,j+1}\right) Y_{jm}$$

$$\boldsymbol{e}_r \cdot \boldsymbol{Y}^{ln}_{jm} = (-1)^{j+l}\ \sqrt{2n+1}\ \left[\sqrt{l+1} \left\{ \begin{array}{ccc} l & n & j \\ 1 & l+1 & 1 \end{array} \right\} \boldsymbol{Y}^{l+1}_{jm} - \sqrt{l} \left\{ \begin{array}{ccc} l & n & j \\ 1 & l-1 & 1 \end{array} \right\} \boldsymbol{Y}^{l-1}_{jm}\right]$$

$$\boldsymbol{e}_r \cdot \boldsymbol{Y}^{j0}_{jm} = \frac{1}{\sqrt{3(2j+1)}} (\sqrt{j+1}\ \boldsymbol{Y}^{j+1}_{jm} - \sqrt{j}\ \boldsymbol{Y}^{j-1}_{jm})$$

$$\boldsymbol{e}_r \cdot \boldsymbol{Y}^{j-2,2}_{jm} = \sqrt{\frac{j-1}{2j-1}}\ \boldsymbol{Y}^{j-1}_{jm}$$

$$\boldsymbol{e}_r \cdot \boldsymbol{Y}^{j-1,2}_{jm} = \sqrt{\frac{j-1}{2(2j+1)}}\ \boldsymbol{Y}^{j}_{jm}$$

$$\boldsymbol{e}_r \cdot \boldsymbol{Y}^{j,2}_{jm} = \sqrt{\frac{j(2j-1)}{2.3.(2j+1)(2j+3)}}\ \boldsymbol{Y}^{j+1}_{jm} - \sqrt{\frac{(j+1)(2j+3)}{2.3.(2j+1)(2j-1)}}\ \boldsymbol{Y}^{j-1}_{jm}$$

$$\boldsymbol{e}_r \cdot \boldsymbol{Y}^{j+1,2}_{jm} = -\sqrt{\frac{j+2}{2(2j+1)}}\ \boldsymbol{Y}^{j}_{jm}$$

$$\boldsymbol{e}_r \cdot \boldsymbol{Y}^{j+2,2}_{jm} = -\sqrt{\frac{j+2}{2j+3}}\ \boldsymbol{Y}^{j+1}_{jm}$$

$$(\mathbf{v}\cdot\boldsymbol{e}_r)\boldsymbol{e}_r=\sum_{jm}\frac{1}{\sqrt{2j+1}}\times$$

$$\left\{\left[jv_{jm}^{j-1}-\sqrt{j(j+1)}v_{jm}^{j+1}\right]\boldsymbol{Y}_{jm}^{j-1}-\left[\sqrt{j(j+1)}v_{jm}^{j-1}-(j+1)v_{jm}^{j+1}\right]\boldsymbol{Y}_{jm}^{j+1}\right\}$$

$$\mathbf{v}-(\mathbf{v}\cdot\boldsymbol{e}_r)\boldsymbol{e}_r=\sum_{jm}v_{jm}^{j}\boldsymbol{Y}_{jm}^{j}+$$

$$\sum_{jm}\frac{1}{2j+1}\left\{\left[(j+1)v_{jm}^{j-1}+\sqrt{j(j+1)}v_{jm}^{j+1}\right]\boldsymbol{Y}_{jm}^{j-1}+\left[\sqrt{j(j+1)}v_{jm}^{j-1}+jv_{jm}^{j+1}\right]\boldsymbol{Y}_{jm}^{j+1}\right\}$$

Differential operators acting on spherical tensors

$$\Delta\left[f(r)Y_{jm}\right]=\left[\frac{d^2f(r)}{dr^2}+\frac{2}{r}\frac{df(r)}{dr}-\frac{j(j+1)f(r)}{r^2}\right]Y_{jm}$$

$$\nabla\left[f(r)Y_{jm}\right]=\frac{1}{\sqrt{2j+1}}\left[\sqrt{j}\left(\frac{d}{dr}+\frac{j+1}{r}\right)f(r)\,\boldsymbol{Y}_{jm}^{j-1}-\sqrt{j+1}\left(\frac{d}{dr}-\frac{j}{r}\right)f(r)\,\boldsymbol{Y}_{jm}^{j+1}\right]$$

$$\nabla\left[f(r)\,\boldsymbol{Y}_{jm}^{l}\right]=(-1)^{j+l+1}\sum_{k}\sqrt{2k+1}\sqrt{l}\begin{Bmatrix}1&1&k\\j&l-1&l\end{Bmatrix}\left(\frac{d}{dr}+\frac{l+1}{r}\right)f(r)\,\boldsymbol{Y}_{jm}^{l-1,k}+$$

$$+(-1)^{j+l}\sum_{k}\sqrt{2k+1}\sqrt{l+1}\begin{Bmatrix}1&1&k\\j&l+1&l\end{Bmatrix}\left(\frac{d}{dr}-\frac{l}{r}\right)f(r)\,\boldsymbol{Y}_{jm}^{l+1,k}$$

$$\nabla\cdot f(r)\,\boldsymbol{Y}_{jm}^{l}=\frac{1}{\sqrt{2j+1}}\left[\sqrt{j}\left(\frac{d}{dr}-\frac{j-1}{r}\right)\delta_{l,j-1}-\sqrt{j+1}\left(\frac{d}{dr}+\frac{j+2}{r}\right)\delta_{l,j+1}\right]f(r)Y_{jm}$$

$$\nabla\times f(r)\,\boldsymbol{Y}_{jm}^{l}=-i\sqrt{6}(-1)^{j+l}\sqrt{l+1}\begin{Bmatrix}l&j&1\\1&1&l+1\end{Bmatrix}\left(\frac{l}{r}-\frac{d}{dr}\right)f(r)\,\boldsymbol{Y}_{jm}^{l+1}-$$

$$-i\sqrt{6}(-1)^{j+l}\sqrt{l}\begin{Bmatrix}l&j&1\\1&1&l-1\end{Bmatrix}\left(\frac{l+1}{r}+\frac{d}{dr}\right)f(r)\,\boldsymbol{Y}_{jm}^{l-1}$$

$$\Delta\left[f(r)\,\boldsymbol{Y}_{jm}^{l}\right]=\left[\frac{d^2f(r)}{dr^2}+\frac{2}{r}\frac{df(r)}{dr}-\frac{l(l+1)f(r)}{r^2}\right]\boldsymbol{Y}_{jm}^{l}$$

$$\Delta\left[f(r)\,\boldsymbol{Y}_{jm}^{ln}\right]=\left[\frac{d^2f(r)}{dr^2}+\frac{2}{r}\frac{df(r)}{dr}-\frac{l(l+1)f(r)}{r^2}\right]\boldsymbol{Y}_{jm}^{ln}$$

$$\nabla \cdot \left[f(r)\, \boldsymbol{Y}^{lk}_{jm} \right] = (-1)^{j+l} \sqrt{2k+1} \times$$

$$\left[\sqrt{l+1} \left\{ \begin{array}{ccc} 1 & l & l+1 \\ j & 1 & k \end{array} \right\} \left(\frac{\mathrm{d}}{\mathrm{d}r} - \frac{l}{r} \right) f(r)\, \boldsymbol{Y}^{l+1}_{jm} - \sqrt{l} \left\{ \begin{array}{ccc} 1 & l & l-1 \\ j & 1 & k \end{array} \right\} \left(\frac{\mathrm{d}}{\mathrm{d}r} + \frac{l+1}{r} \right) f(r)\, \boldsymbol{Y}^{l-1}_{jm} \right]$$

Clebsch-Gordan coefficients

More on the definition of Clebsch-Gordan coefficients and related Wigner symbols could be found again in Varshalovich et al., 1988 or [i8]. Here we will be dealing just with the properties most useful to our purpose.

◇ Symmetries of Clebsch-Gordan coefficients

$$C^{jm}_{j_1 m_1\ j_2 m_2} = (-1)^{j+j_1+j_2}\ C^{j,-m}_{j_1,-m_1\ j_2,-m_2} = (-1)^{j+j_1+j_2}\ C^{jm}_{j_2 m_2\ j_1 m_1}$$

$$\begin{aligned}
C^{jm}_{j_1 m_1\ j_2 m_2} &= (-1)^{j_1+m_1}\ \frac{\Pi_j}{\Pi_{j_2}}\ C^{j_2,-m_2}_{j_1 m_1\ jm} \\
C^{jm}_{j_1 m_1\ j_2 m_2} &= (-1)^{j_1+m_1}\ \frac{\Pi_j}{\Pi_{j_2}}\ C^{j_2 m_2}_{jm\ j_1,-m_1} \\
C^{jm}_{j_1 m_1\ j_2 m_2} &= (-1)^{j_2+m_2}\ \frac{\Pi_j}{\Pi_{j_1}}\ C^{j_1,-m_1}_{j,-m\ j_2 m_2} \\
C^{jm}_{j_1 m_1\ j_2 m_2} &= (-1)^{j_2+m_2}\ \frac{\Pi_j}{\Pi_{j_1}}\ C^{j_1 m_1}_{j_2,-m_2\ jm}
\end{aligned}$$

◇ Values of coefficients for a special choice of indices

$$\begin{aligned}
C^{j0}_{j_1 0\ j_2 0} &= 0 \quad \text{if} \quad j_1 + j_2 + j_3 \quad \text{is odd} \\
C^{j+1,0}_{j0\ 10} &= \sqrt{\frac{j+1}{2j+1}} \\
C^{j-1,0}_{j0\ 10} &= -\sqrt{\frac{j}{2j+1}} \\
C^{jm}_{j_1 m_1\ 00} &= \delta_{jj_1}\delta_{mm_1} \\
C^{00}_{j_1 m_1\ j_2 m_2} &= \frac{(-1)^{j_1+m_1}}{\Pi_{j_1}}\ \delta_{j_1 j_2}\delta_{m_1,-m_2} \\
C^{jj}_{j_1 j_1\ j_2 j_2} &= \delta_{j_1+j_2,j}
\end{aligned}$$

◇ Sums of Clebsch-Gordan coefficients

$$\sum_{m_1 m_2} C^{jm}_{j_1 m_1\ j_2 m_2}\, C^{j'm'}_{j_1 m_1\ j_2 m_2} = \delta_{jj'}\delta_{mm'}$$

$$\sum_{m m_1} C^{jm}_{j_1 m_1\ j_2 m_2}\, C^{jm}_{j_1 m_1\ j_3 m_3} = \frac{\Pi_j}{\Pi_{j_2}}\, \delta_{j_2 j_3}\delta_{m_2 m_3}$$

$$\sum_{n_1 n_2 n_3} C^{j_3 m_3}_{l_1 n_1\ l_2 n_2}\, C^{j_1 m_1}_{l_3 n_3\ l_2 n_2}\, C^{l_3 n_3}_{l_1 n_1\ j_2 m_2} = (-1)^{j_1+l_2+l_3}\, \Pi_{j_3 l_3}\, C^{j_1 m_1}_{j_2 m_2\ j_3 m_3} \left\{ \begin{array}{ccc} l_1 & l_2 & j_3 \\ j_1 & j_2 & l_3 \end{array} \right\}$$

$$\sum_{n_1 n_2 n_3 n_4} C^{j_1 m_1}_{l_1 n_1\ l_2 n_2}\, C^{j_2 m_2}_{l_3 n_3\ l_4 n_4}\, C^{j_3 m_3}_{l_3 n_3\ l_1 n_1}\, C^{j_4 m_4}_{l_4 n_4\ l_2 n_2} =$$

$$(-1)^{j+j_1+j_2}\, \Pi_{j_1 j_2 j_3 j_4} \sum_{jm} C^{jm}_{j_1 m_1\ j_2 m_2}\, C^{jm}_{j_3 m_3\ j_4 m_4} \left\{ \begin{array}{ccc} l_2 & l_1 & j_1 \\ l_4 & l_3 & j_2 \\ j_4 & j_3 & j \end{array} \right\}$$

◇ Clebsch-Gordan coefficients and 3-j Wigner symbols

$$\begin{aligned} C^{jm}_{j_1 m_1\ j_2 m_2} &= (-1)^{j_1+j_2+m}\, \Pi_j \begin{pmatrix} j_1 & j_2 & j \\ m_1 & m_2 & -m \end{pmatrix} \\ \begin{pmatrix} j_1 & j_2 & j \\ m_1 & m_2 & -m \end{pmatrix} &= \frac{(-1)^{j+m}}{\Pi_j}\, C^{jm}_{j_1,-m_1\ j_2,-m_2} \end{aligned}$$

6-j Wigner symbols

◇ Values of 6-j symbols for a special choice of indices

$$\begin{aligned} \left\{ \begin{array}{ccc} j_1 & j_2 & j \\ l_1 & l_2 & 0 \end{array} \right\} &= \frac{(-1)^{j_1+j_2+j}}{\Pi_{j_1 j_2}}\, \delta_{j_1 l_2}\delta_{j_2 l_1} \\ \left\{ \begin{array}{ccc} j & 2 & j-2 \\ 1 & j-1 & 1 \end{array} \right\} &= \frac{1}{\sqrt{5(2j-1)}} \\ \left\{ \begin{array}{ccc} j & 2 & j+2 \\ 1 & j+1 & 1 \end{array} \right\} &= \frac{1}{\sqrt{5(2j+3)}} \\ \left\{ \begin{array}{ccc} j & j & 2 \\ 1 & 1 & j-1 \end{array} \right\} &= \sqrt{\frac{(j+1)(2j+3)}{2.3.5.j(2j-1)(2j+1)}} \end{aligned}$$

$$\left\{ \begin{array}{ccc} j & j & 2 \\ 1 & 1 & j+1 \end{array} \right\} = \sqrt{\frac{j(2j-1)}{2.3.5.(2j+3)(j+1)(2j+1)}}$$

$$\left\{ \begin{array}{ccc} j & 1 & j \\ 2 & j+1 & 1 \end{array} \right\} = -\sqrt{\frac{j+2}{2.5.(j+1)(2j+1)}}$$

$$\left\{ \begin{array}{ccc} j & 1 & j \\ 2 & j-1 & 1 \end{array} \right\} = -\sqrt{\frac{j-1}{2.5.j(2j+1)}}$$

$$\left\{ \begin{array}{ccc} j & j & 1 \\ 1 & 1 & j+1 \end{array} \right\} = \sqrt{\frac{j}{2.3.(j+1)(2j+1)}}$$

$$\left\{ \begin{array}{ccc} j & j & 1 \\ 1 & 1 & j-1 \end{array} \right\} = -\sqrt{\frac{j+1}{2.3.j(2j+1)}}$$

9-j Wigner symbols

◇ Values of 9-j symbols for a special choice of indices

$$\left\{ \begin{array}{ccc} 0 & j & j \\ l & k_1 & k_2 \\ l & k_3 & k_4 \end{array} \right\} = \frac{(-1)^{j+l+k_2+k_3}}{\Pi_{jl}} \left\{ \begin{array}{ccc} k_4 & k_2 & j \\ k_1 & k_3 & l \end{array} \right\}$$

Appendix B

Spectral-spatial Methods

Frequent geophysical task is to display features of physical fields but only at a certain scale. For this purpose harmonic analysis could be used when the degree corresponds to a desired size. But this approach is complicated by the global character of harmonic functions – since the value at any place in the reconstructed field (e.g. topography of the required wavelength at the north pole) is influenced by the rest of the field's contributions to a given spherical harmonic coefficient.

B.1 Continuous Wavelet Transform

Another possible way to solve this problem is to employ a continuous wavelet transform, which a method is widely discussed by Daubechies, 1992; Torrence and Compo, 1998; Vecsey, 2002 et al. This method is based on the convolution of the wavelet function $\psi_0(a)$ (where a is a desired scale) – which is well localized in both the space and spectrum – with the given physical field, and enables us to display just the local anomalies of the size corresponding to the scale of the wavelet. For the wavelet we can use any odd (better resolution of edges) or even (better space resolution) function (Vecsey, 2002) but it must satisfy the condition of admissibility and unit energy of the whole space:

$$\int_{-\infty}^{\infty} \psi_0(\eta) d\eta = 0 \tag{B.1}$$

$$\int_{-\infty}^{\infty} |\psi_0(\eta)|^2 d\eta = 1, \tag{B.2}$$

where equation B.1 keeps the wavelet transform unaffected by the mean of analyzed function and equation B.2 provides the normalization of resulting wavelet transform. For our purposes we use the so-called Mexican Hat (second derivative of the Gaussian) as the wavelet function for both 1D and 2D. This wavelet is isotropic – and therefore detects the features from all directions with the same width and weight – and well localized in space which is necessary to obtain the good space resolution.

For displaying results (scalograms) we need an additional dimension for scale – this is not a problem in the case of 1D but for the 2D wavelet transform we have to choose between 3D diagrams (which are difficult to display) and slices showing one certain scale. In this work we use the second method and show several slices for certain distinguished scales.

B.1.1 1D Wavelets

In the case of 1D signal analysis we can use the wavelet transform (B.3) to display contributions of different frequencies to the original data. This method can be a useful tool for such things as a time-series study (Vecsey and Matyska, 2001) or raw-data analysis (Turcotte et al., 2002). For displaying results the time/period scalograms or a superposition of wavelet transform with the gradual offset are suitable. When dealing with a Cartesian signal we can separate high-significance data from the white or red noise by using a cone of influence (Torrence and Compo, 1998; Vecsey, 2002). Below is the definition of the 1D wavelet transform and its spectrum:

$$\Psi_f(a,b) = a^{-\frac{1}{2}} \int_{-\infty}^{\infty} f(x)\psi_0^*(\frac{x-b}{a})\,dx \tag{B.3}$$

$$\hat{\Psi}_f(a,\omega) = a^{\frac{1}{2}} \hat{f}(x)\hat{\psi}_0^*(a\omega), \tag{B.4}$$

where b is the position of the wavelet transform, $f(x)$ is the analyzed function, asterisk denotes the complex conjunction, hat the Fourier transform and ω is the frequency in Fourier space. Because of the homogeneity of the signal $f(x)$ we can convert the wavelet transform (B.3) into a Fourier space (B.4) and vice versa – this is a very efficient way of computing as it rapidly decreases the computational time.

B.1.2 2D Wavelets

For a 2D wavelet transform (B.5) on the Cartesian domain we use a transformation similar to the 1D case but enhanced to another dimension. Such an extension could be carried out even for more dimensions (e.g. studying 3D structures – see Bergeron et al., 1999) but then the computational requirements increase and displaying the results becomes more difficult. As well as in the previous case a transform into Fourier space (B.6) is again very favorable and spares a lot of computational time. The definition of the 2D wavelet transform and its spectrum is as follows:

$$\Psi_f(a,\boldsymbol{b}) = a^{-1} \int_0^{L_x}\int_0^{L_y} f(\boldsymbol{x})\psi_0^*(\frac{\boldsymbol{x}-\boldsymbol{b}}{a})\,d\boldsymbol{x}^2 \tag{B.5}$$

$$\hat{\Psi}_f(a,\boldsymbol{k}) = a\hat{f}(\boldsymbol{k})\hat{\psi}_0^*(a\boldsymbol{k}), \tag{B.6}$$

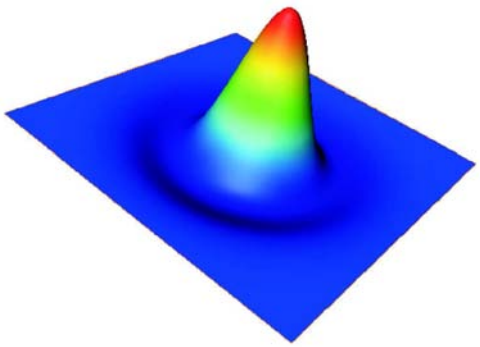

Figure B.1: 2D Mexican Hat wavelet function

where $\boldsymbol{k}$ is the wavevector in the Fourier space. An often used 2D wavelet is the Mexican Hat (Fig. B.1), which is defined on the Cartesian domain as a second derivative of the Gaussian normal function centered at the origin and dependant only on the radial vector $\boldsymbol{r} = \boldsymbol{r}(x, y)$:

$$\psi_0(\boldsymbol{r}) = \frac{1}{\sqrt{2\pi}}\left(\frac{\partial^2}{\partial x^2} + \frac{\partial^2}{\partial y^2}\right)e^{-\frac{1}{2}|\boldsymbol{r}|^2} = \frac{1}{\sqrt{2\pi}}(2 - |\boldsymbol{r}|^2)e^{-\frac{1}{2}|\boldsymbol{r}|^2} \tag{B.7}$$

B.2 2D Spherical Localization

When we apply the method of a 2D wavelet transform to data fields on the sphere (e.g. gravity, topography etc.) transformed by a cylindrical projection to Cartesian coordinates, only regional studies should be considered. But when we need to analyze whole spherical data sets we obtain a distortion increasing with latitude (e.g. Vecsey et al., 2003). A solution to this problem is to substitute a wavelet transform by another transformation defined on a sphere. It employs wavelets or other localized functions with a spherical correction (Fig. B.2) which in the Euclidian limit gives the 2D wavelet transform as mentioned in previous section. Several different approaches have been suggested (Antoine et al., 2002; Michel, 2002) but they are usually very mathematically complicated and are rarely employed by geophysical community. Therefore some easier methods have been proposed – here two which are widely used in the planetary sciences are outlined.

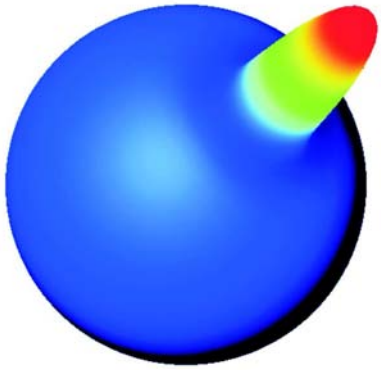

Figure B.2: 2D Mexican Hat with the spherical correction

B.2.1 Spectral Approach

The general principle of the localization is (as well as in the case of the wavelet transform) based on the convolution of an analyzed field $A(\Omega)$ with a window function $W(\Omega)$ on the sphere Ω. The first possible method was presented by Simons et al., 1997 and it is realized purely in the spectral domain by operations with spherical harmonic (SH) coefficients (equations B.8-B.11). However one must remember that the following sequence of obtaining the localized field is only for a certain window-scale and window-position – for another scale or position of the window function on the sphere some other set of SH coefficient is obtained. In the following terms the normalization and phase convention are the same as in e.g. Varshalovich et al., 1988:

$$\Psi(\Omega) = W(\Omega)A(\Omega) = \sum_{jm} \psi_{jm} Y_{jm}(\Omega) \tag{B.8}$$

$$\psi_{jm} = \int A(\Omega) W(\Omega) Y^*_{jm}(\Omega)\, d\Omega \tag{B.9}$$

$$\psi_{jm} = \sum_{j_1 m_1 j_2 m_2} a^*_{j_1 m_1} w^*_{j_2 m_2} \xi_{j_1 j_2 l} \begin{pmatrix} j_1 & j_2 & j \\ 0 & 0 & 0 \end{pmatrix} \begin{pmatrix} j_1 & j_2 & j \\ m_1 & m_2 & m \end{pmatrix} \tag{B.10}$$

$$\xi_{j_1 j_2 \dots j_n} = \sqrt{\frac{(2j_1+1)(2j_2+1)\dots(2j_n+1)}{4\pi}} \tag{B.11}$$

where a_{jm}, w_{jm} and ψ_{jm} are respectively SH coefficients of analyzed field, window function and obtained localized field; $\left(\begin{smallmatrix} j_1 & j_2 & j \\ 0 & 0 & 0 \end{smallmatrix}\right)$ and $\left(\begin{smallmatrix} j_1 & j_2 & j \\ m_1 & m_2 & m \end{smallmatrix}\right)$ are the Wigner 3-j symbols defined e.g. by Varshalovich et al., 1988. Using the ψ_{jm} and γ_{jm} coefficients of two localized fields we can construct the cross-covariance coefficient (B.12), RMS amplitude of Ψ (B.13), the correlation between Ψ and Γ (B.14) and the transfer function (admittance) (B.15):

$$\sigma^2_{\Psi\Gamma}(j) = \sum_m \psi_{jm}\gamma^*_{jm} \tag{B.12}$$

$$S_j(\Omega) = \sqrt{\frac{\sigma^2_{\Psi\Psi}(\Omega)}{2j+1}} \tag{B.13}$$

$$r_j(\Omega) = \frac{\sigma^2_{\Psi\Gamma}(\Omega)}{\sqrt{\sigma^2_{\Psi\Psi}(\Omega)\sigma^2_{\Gamma\Gamma}(\Omega)}} \tag{B.14}$$

$$F_j(\Omega) = \frac{\sigma^2_{\Psi\Gamma}(\Omega)}{\sigma^2_{\Psi\Psi}(\Omega)}. \tag{B.15}$$

B.2.2 Spatial Approach

Another approach to a spherical localization is based on spatial computation and was presented by Kido et al., 2003. The main advantages of this method are its computational simplicity and an option to process only a selected interval instead of the whole spherical surface, which is essential when we desire to work with high resolution or short wavelengths. Therefore we choose this system (B.16-B.17) for our calculations in Chapter 6 with parameters used by the authors. As a window function we apply the spherical wavelet-like function $F_{j_w,\sigma,\vartheta_0,\varphi_0}(\vartheta,\varphi)$ centered in (ϑ_0,φ_0) with wavelength j_w and optional parameter σ, which controls the width of the wavelet-like function:

$$F_{j_w,\sigma,\vartheta_0,\varphi_0}(\vartheta,\varphi) = j_w^2 \exp\Big(-\Big(\frac{j_w\xi}{2\sigma}\Big)^2\Big)\Big[J_0(j_w\xi)\frac{\xi}{\sin\xi} - \exp(-\sigma^2)\Big] \tag{B.16}$$

$$\cos\xi = \cos\vartheta_0\cos\vartheta + \sin\vartheta_0\sin\vartheta\cos(\phi_0-\phi). \tag{B.17}$$

where ξ is the angular distance to the center of the wavelet-like function (ϑ_0,φ_0) and J_0 is the Bessel function of order zero (the resulting function is very close to Mexican hat wavelet mentioned in the previous section). Using these definitions we can evaluate the transformed field $\tilde{A}$ (B.18), the correlation between two fields (in our case G and T i.e. geoid and topography respectively) (B.19) and the admittance between these fields (B.20) – both of which are using the appropriate window (B.21) which also acts as a weighting function if we understand this problem as a least square fit.

$$\tilde{A}_{j_w,\sigma}(\vartheta_0,\varphi_0) = \frac{1}{4\pi}\int_0^{2\pi}\int_0^{\pi} A(\vartheta,\varphi)F_{j_w,\sigma,\vartheta_0,\varphi_0}(\vartheta,\varphi)\sin\vartheta\,d\vartheta\,d\varphi \tag{B.18}$$

$$C_{j_w,\sigma}(\vartheta_0,\varphi_0) = \frac{\int_\Omega W_{j_w,\sigma}(\xi)\tilde{T}(\varphi,\vartheta)\tilde{G}(\varphi,\vartheta)d\Omega}{\sqrt{\int_\Omega W_{j_w,\sigma}(\xi)\tilde{T}^2(\varphi,\vartheta)\,d\Omega\ \int_\Omega W_{j_w,\sigma}(\xi)\tilde{G}^2(\varphi,\vartheta)\,d\Omega}} \tag{B.19}$$

$$Z_{j_w,\sigma}(\vartheta_0,\varphi_0) = \frac{\int_\Omega W_{j_w,\sigma}(\xi)\tilde{T}(\varphi,\vartheta)\tilde{G}(\varphi,\vartheta)d\Omega}{\int_\Omega W_{j_w,\sigma}(\xi)\tilde{T}^2(\varphi,\vartheta)\,d\Omega} \tag{B.20}$$

$$W_{j_w,\sigma}(\xi) \;=\; \exp\left[-\left(\frac{j_w\xi}{2\sigma}\right)^2\right] \tag{B.21}$$

The localized geoid and topography analysis are progressive tools in looking for the local geophysical mechanisms (e.g. crustal thickness by SIMONS ET AL., 1997 or elastic lithosphere thickness by MCGOVERN ET AL., 2002) whereas the spatial correlation and admittance maps can examine a lateral variation of geoid/topography relations (e.g. estimations of different generating mechanisms by KIDO ET AL., 2003). They can also help us in the future to improve new spherical harmonic models of the geoid which would be the basis for a better determination of the topographical elevation (KONOPLIV ET AL., 1999 and RAPPAPORT ET AL., 1999).

B.3 Compositional Methods

One of the disadvantages in the localization of geophysical fields is the difficulty displaying the 2D analysis results and the redundant information contained in CWT. Hence a method combining the advantages of a localization approach with synthetic processing is needed – in this thesis we employed a modification of the E_{max}-k_{max} method (BERGERON ET AL., 1999) for spherical fields:

$$E_{max}(\vartheta,\varphi) \;=\; \max_{\langle j_{w1},j_{w2}\rangle} |\psi_{j_w,\sigma}(\vartheta,\varphi)|^2 \tag{B.22}$$

$$\tilde{E}_{max}(\vartheta,\varphi) \;=\; \max_{\langle j_{w1},j_{w2}\rangle} |\psi_{j_w,\sigma}(\vartheta,\varphi)|^2 \cdot \operatorname{sgn}\, \psi_{j_w,\sigma}(\vartheta,\varphi). \tag{B.23}$$

This technique simply analyzes the observed data on a given interval $\langle j_{w1}, j_{w2}\rangle$ by means of localization and registers the highest value of the transformed field for each grid point (E_{max} B.22 or $\tilde{E}_{max}$ B.23, if we take into an account the sign of signal) and the corresponding wavelength j_w – these quantities are then displayed in new 2D maps.

Appendix C

Dynamic Modelling

The aim of dynamic modelling in our work is to predict a rheology of the venusian mantle. Because we do not have any information about the density structure, phase transitions, layering nor geochemical composition we have to find an adequate method which can incorporate the only known quantities – gravitational potential and topography. Therefore we will try to predict the observed data by means of the internal loading theory which was already successfully used earlier for research on Earth (e.g. Čadek et al., 1997) and also on Venus (e.g. Kiefer and Peterson, 2003).

C.1 Governing Equations

The mantle flow in our model is controlled only by the density structure of the venusian mantle (which controls the buoyancy forces) and its viscous profile. The basic set of equations must then incorporate the continuity equation, the equation of motion and the rheology equation. For our purpose we consider several simplifications (neglecting of the self-gravitation and compressibility of newtonian material) but despite that we can still use this model to predict the venusian geoid and topography with high accuracy (Kiefer et al., 1986). Hence the equations of flow are handled in the following form:

$$\nabla \cdot \tau + \rho\, \boldsymbol{g} = 0 \tag{C.1}$$

$$\nabla \cdot \boldsymbol{v} = 0 \tag{C.2}$$

$$\tau = -\boldsymbol{I}p + \eta(\nabla \boldsymbol{v} + \nabla^T \boldsymbol{v}), \tag{C.3}$$

where τ is the stress tensor, ρ stands for the density, $\boldsymbol{g}$ for the normal gravity acceleration, $\boldsymbol{v}$ for the flow velocity, p for the hydrostatic pressure and η for the viscosity. However because the internal structure of Venus is not known we keep $\boldsymbol{g}$ constant trough the whole model. The geoid and topography induced by the flow described by equations C.1-C.3 does not generally depend on the absolute values of viscosity and therefore our results can reveal only relative viscosity contrasts.

C.2 Parametrization and Numerical Solution

The governing equations are solved for the whole mantle, i.e. in the spherical layer between surface and core-mantle boundary. At both boundaries we employ the free slip condition C.4 (because of zero tangential stress) and zero vertical velocity C.5 (because no material is penetrating trough the surface nor CMB) as reasoned by e.g. KÝVALOVÁ, 1994:

$$\boldsymbol{v} \cdot \boldsymbol{e}_r = 0 \tag{C.4}$$

$$\tau \cdot \boldsymbol{e}_r - [(\tau \cdot \boldsymbol{e}_r) \cdot \boldsymbol{e}_r]\, \boldsymbol{e}_r = 0. \tag{C.5}$$

Now we have to choose the numerical method to work with these mathematical terms. As shown in Appendix A, a very reasonable way to do that is to employ the spherical harmonics. By using them we can express all the scalar (A.2), vector (A.46) and tensor (A.57) quantities by terms containing only appropriate coefficients and harmonic functions. Because the terms are not coupled together through different orders we can separate them into individual equations for every degree and order. Thus we can rewrite boundary conditions (C.4 and C.5) into:

$$\sqrt{j}\, v_{jm}^{j-1}(r) - \sqrt{j+1}\, v_{jm}^{j+1}(r) = 0 \tag{C.6}$$

$$\frac{j+1}{2j+1}\sqrt{\frac{j-1}{2j-1}}\,\tau_{jm}^{j-2,2}(r) - \frac{1}{2j+1}\sqrt{\frac{j(j+1)(j+2)}{2j+3}}\,\tau_{jm}^{j+2,2}(r) - \sqrt{\frac{3(j+1)}{2(2j-1)(2j+1)(2j+3)}}\,\tau_{jm}^{j2}(r) = 0, \tag{C.7}$$

the equation of motion (C.1) into a set of two equations:

$$-\sqrt{\frac{j}{3(2j+1)}}\left(\frac{d}{dr} + \frac{j+1}{r}\right)\tau_{jm}^{j0}(r) + \sqrt{\frac{j-1}{2j-1}}\left(\frac{d}{dr} - \frac{j-2}{r}\right)\tau_{jm}^{j-2,2}(r) - \sqrt{\frac{(j+1)(2j+3)}{6(2j-1)(2j+1)}}\left(\frac{d}{dr} + \frac{j+1}{r}\right)\tau_{jm}^{j2}(r) = -f_{jm}^{j-1}(r) \tag{C.8}$$

$$\sqrt{\frac{j+1}{3(2j+1)}}\left(\frac{d}{dr} - \frac{j}{r}\right)\tau_{jm}^{j0}(r) + \sqrt{\frac{j(2j-1)}{6(2j+3)(2j+1)}}\left(\frac{d}{dr} - \frac{j}{r}\right)\tau_{jm}^{j2}(r) - \sqrt{\frac{j+2}{2j+3}}\left(\frac{d}{dr} + \frac{j+3}{r}\right)\tau_{jm}^{j+2,2}(r) = -f_{jm}^{j+1}(r), \tag{C.9}$$

the continuity equation (C.2) into:

$$\sqrt{\frac{j}{2j+1}}\left(\frac{d}{dr} - \frac{j-1}{r}\right)v_{jm}^{j-1}(r) - \sqrt{\frac{j+1}{2j+1}}\left(\frac{d}{dr} + \frac{j+2}{r}\right)v_{jm}^{j+1}(r) = 0, \tag{C.10}$$

and the constitutive relation (C.3) into three equations:

$$\tau_{jm}^{j-2,2}(r) - 2\eta\sqrt{\frac{j-1}{2j-1}}\left(\frac{d}{dr}+\frac{j}{r}\right)v_{jm}^{j-1}(r) = 0 \qquad \text{(C.11)}$$

$$\tau_{jm}^{j2}(r) + 2\eta\sqrt{\frac{(j+1)(2j+3)}{6(2j-1)(2j+1)}}\left(\frac{d}{dr}-\frac{j-1}{r}\right)v_{jm}^{j-1}(r) -$$

$$-2\eta\sqrt{\frac{j(2j-1)}{6(2j+3)(2j+1)}}\left(\frac{d}{dr}+\frac{j+2}{r}\right)v_{jm}^{j+1}(r) = 0 \qquad \text{(C.12)}$$

$$\tau_{jm}^{j+2,2}(r) + 2\eta\sqrt{\frac{j+2}{2j+3}}\left(\frac{d}{dr}-\frac{j+1}{r}\right)v_{jm}^{j+1}(r) = 0. \qquad \text{(C.13)}$$

However these terms describe only the spheroidal part of the governing equations – there is no toroidal flow in the mantle with only radial viscosity structure (e.g. Ricard and Vigni, 1989). Therefore the corresponding terms v_{jm}^{j}, $\tau_{jm}^{j-1,2}$ and $\tau_{jm}^{j+1,2}$ are identically equal to zero. Now we have a set of 6 equations for 6 unknown quantities $v_{jm}^{j-1}(r)$, $v_{jm}^{j+1}(r)$, $\tau_{jm}^{j-2,2}(r)$, $\tau_{jm}^{j2}(r)$, $\tau_{jm}^{j0}(r)$ and $\tau_{jm}^{j+2,2}(r)$ for each degree and order. We will solve this problem for $j \geq 2$ because we are interested mainly in the explanation of observed local geoid and topographic features rather than in the center-of-mass/center-of-figure offset. In equations C.8 and C.9 the terms $f_{jm}^{j-2,2}$ and $f_{jm}^{j-2,2}$ denote the SH coefficients of buoyancy force:

$$f_{jm}^{j-1} = -g\rho_{jm}\sqrt{\frac{j}{2j+1}} \qquad f_{jm}^{j+1} = g\rho_{jm}\sqrt{\frac{j+1}{2j+1}}. \qquad \text{(C.14)}$$

If we have a solution of this set of equations we can easily calculate the amplitudes of the dynamic topography t. When we start with the term for hydrostatic equilibrium at the top/bottom boundary ($-$ and $+$ sign respectively) we quickly obtain the result:

$$\mp(\tau\cdot\boldsymbol{e}_r)\cdot\boldsymbol{e}_r = \Delta\rho g_0 t \qquad \Rightarrow \qquad t = \mp\frac{(\tau\cdot\boldsymbol{e}_r)\cdot\boldsymbol{e}_r}{\Delta\rho g_0}. \qquad \text{(C.15)}$$

Transforming this result into the spherical harmonic form gives:

$$t_{jm}(r) = \mp\frac{1}{\Delta\rho g_0}\Big(\frac{1}{\sqrt{3}}\tau_{jm}^{j\,0}(r) - \sqrt{\frac{j(j-1)}{(2j+1)(2j-1)}}\tau_{jm}^{j-2,2} -$$

$$- \sqrt{\frac{(j+1)(j+2)}{(2j+1)(2j+3)}}\tau_{jm}^{j+2,2} + \sqrt{\frac{2j(j+1)}{3(2j-1)(2j+3)}}\tau_{jm}^{j,2}\Big). \qquad \text{(C.16)}$$

The dynamically generated geopotential is then generated by contributions from surface and CMB topography (we can use terms A.26 and A.25 respectively) and from the uneven mass distribution in the mantle:

$$V_{jm} = V_{jm}^{surf} + V_{jm}^{mantle} + V_{jm}^{CMB} \qquad \text{(C.17)}$$

$$V_{jm}^{mantle} = \frac{4\pi\kappa R}{2j+1}\int_{R_{CMB}}^{R_{surf}}\left(\frac{r'}{R}\right)^{j+2}\rho_{jm}(r')\,dr' \qquad \text{(C.18)}$$

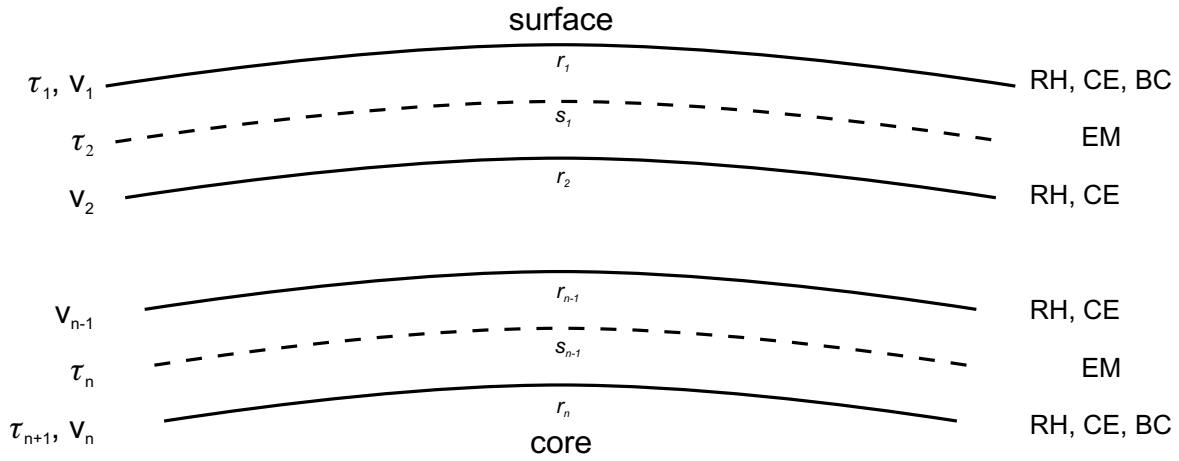

Figure C.1: The alternating scheme for finite difference method – at every layer boundary we calculate τ and at every center of layer $\boldsymbol{v}$ by using the appropriate equations. RH in the description stands for rheological equation (C.3), CE for continuity equations (C.2), BC for boundary conditions (C.4, C.5) and EM for the equation of motion (C.1)

To solve all these differential equations we use the spherical harmonic approach for ϑ, φ coordinates and for the r coordinate we employ the method of finite differences. We divide the mantle into $n-1$ layers and the derivatives in these equations then become:

$$\frac{df}{dr}(r_1) \simeq \frac{1}{h}(f_1 - f_2) \tag{C.19}$$

$$\frac{df}{dr}(r_i) \simeq \frac{1}{2h}(f_{i-1} - f_i) \quad i = 2, \ldots, n-1 \tag{C.20}$$

$$\frac{df}{dr}(r_n) \simeq \frac{1}{h}(f_{n-1} - f_n), \tag{C.21}$$

where h is the semi-thickness of the particular layer (from its boundary to its center). The computational grid does not have all quantities defined at common layer boundaries but we rather use the alternating scheme because of its numerical stability (Kývalová, 1994). This defines the components of stress tensor τ at layer boundaries, whereas the components of velocity $\boldsymbol{v}$ are evaluated at their centers. At the uppermost and lowermost boundaries we group both τ and $\boldsymbol{v}$ together because the boundary conditions need them to be evaluated (see Fig. C.1).

When we divide the mantle into $n-1$ layers we have n boundaries but at the surface and CMB we also need to evaluate boundary conditions. Therefore we have $6n+2$ equations and by appropriate positioning we can obtain the band-matrix which is easy to solve e.g. by FORTRAN numerical libraries (Numerical Recipes etc.). The response functions for constant viscosity trough the mantle (Fig. C.2) show the contributions of load corresponding to the layer thickness at every single layer for both gravitational potential and topography.

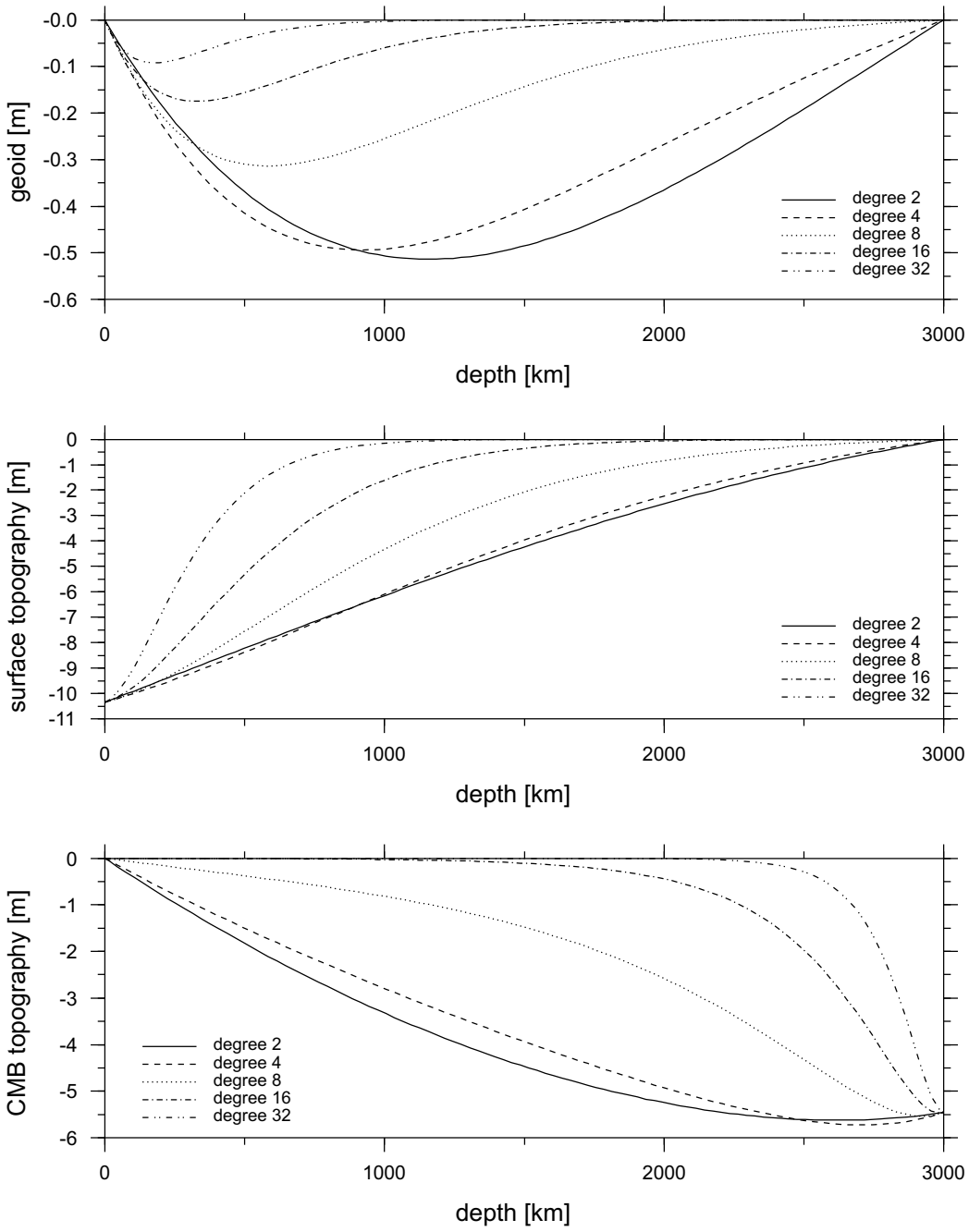

Figure C.2: The response functions for venusian geoid (top) and topography (middle for surface and bottom for CMB) at degrees j=2,4,8,16,32. The depth of the mantle is set to the assumed 3,000 km and the viscosity is handled as a constant. For this model (100 layers) the load corresponds to the layer thickness. The amplitude of the dynamic topography at appropriate boundary could be then evaluated analytically as $-h/\Delta\rho$, where h is the parametric layer thickness and $\Delta\rho$ stands for the density contrast (at upper boundary 2,900 and at CMB 5,500 kg·m^{-3})

C.3 Inverse Problem

As we have a definition of the forward problem we can model the dynamic geoid and topography for a given 3D density structure and 1D viscosity profile. Because of the results nonlinear dependency on viscosity such an inverse problem could be solved only by appropriate numerical methods such as the Monte Carlo random search, a genetic algorithm or simulated annealing method (see review in TARANTOLA, 1987 or MATAS, 1995). These techniques are computationally demanding and could give us a broad spectrum of differing results.

Nevertheless we can divide the algorithm into the two-step inversion – in each round of search we first choose the viscosity by some previously mentioned technique and then derive the density structure which produce the smallest L_2 norm difference between the observed and predicted data. To obtain a unique solution we consider only lateral density variations, thus the mantle model should have a plume-like character – this is only a kind of mathematical representation which should not be confused with the real unknown venusian mantle structure. However, it could be proved (KIEFER ET AL., 1986) that such a mantle flow model does not have a high sensitivity to the exact density distribution.

For the linear problem in step two we can calculate the analytical solution by the minimization of the least-square misfit between the observed and predicted data. This specific misfit function we define as:

$$S^2(\rho,\eta) = \sum_{j=0}^{jmax}\sum_{m=-j}^{j} S_{jm}^2(\rho,\eta) \tag{C.22}$$

$$S_{jm}^2(\rho,\eta) = \frac{(t_{jm}^{pred}-t_{jm}^{obs})(t_{jm}^{pred}-t_{jm}^{obs})^*}{\sigma_j^2} + (g_{jm}^{pred}-g_{jm}^{obs})(g_{jm}^{pred}-g_{jm}^{obs})^*, \tag{C.23}$$

where asterisk denotes the complex conjunction, g_{jm}^{pred} and g_{jm}^{obs} respectively predicted and observed spherical harmonic coefficient of gravitational potential (the same for topography) and σ_j^2 is a degree *a priori* weighting function whose purpose is to balance power signals from topography and the geoid:

$$\sigma_j^2 = \frac{\sum_{m=-j}^{j} t_{jm}^{obs} t_{jm}^{obs*}}{\sum_{m=-j}^{j} g_{jm}^{obs} g_{jm}^{obs*}}. \tag{C.24}$$

Because g_{jm}^{pred} and t_{jm}^{pred} are linearly dependent on density, we can decompose them into a density term ρ_{jm} (we can omit the r dependency because there are only lateral variances) and response functions g_j, t_j (neither C.16 nor C.17 are dependant on m) which are depth integrals of a full-mantle load (unit mass and given viscosity structure) response functions:

$$t_{jm}^{pred} = \rho_{jm} t_j(\eta) \tag{C.25}$$

$$g_{jm}^{pred} = \rho_{jm} g_j(\eta), \tag{C.26}$$

where the best ρ_{jm} for the given viscosity profile is uniquely given by the derivative of a misfit function equal to zero – then we can analytically find the solution:

$$\frac{\partial S_{jm}^2}{\partial \rho_{jm}} = 0 \tag{C.27}$$

$$\rho_{jm} = \frac{\frac{t_j t_{jm}^{obs}}{\sigma_j^2} + g_j g_{jm}^{obs}}{\frac{t_j t_j}{\sigma_j^2} + g_j g_j}. \tag{C.28}$$

When we look at the case where the topography is of purely dynamic origin (100% dynamic support) we can use only the equation C.25 and then the resulting term for density then becomes very simple. However we do not consider these modifications because the obtained gravitational potential has low both spectral and spatial correlation with the observed data and moreover solely the dynamic support of the topography for selected broad spectral intervals is unrealistic – more desired is to divide the modelling error equally between predicted geoid and topography.

Finally to evaluate the level of overall agreement between the observed and predicted gravitational potential spectra we can examine the correlation (C.29) or percentage of fitted data quantity (C.30) for every obtained result. These can give us a valuable information about quality of our models.

$$c = \frac{\sum\limits_{jm} g_{jm}^{pred} g_{jm}^{obs*}}{\sqrt{\sum\limits_{jm} g_{jm}^{pred} g_{jm}^{pred*}} \sqrt{\sum\limits_{jm} g_{jm}^{obs} g_{jm}^{obs*}}} \tag{C.29}$$

$$p = 1 - \frac{||g^{pred} - g^{obs}||^2}{||g^{obs}||^2} \tag{C.30}$$

Bibliography

[1] Arkani-Hamed J. (1996): Analysis and interpretation of the surface topography and gravitational potential of Venus. *J. Geophys. Res.* **101**, 4711-4724.

[2] Antoine J.-P., Demanet L., Jacques L., Vandergheynst P. (2002): Wavelets on the sphere: implementation and approximations. *Appl. Comput. Harmon. Anal.* **13** 3, 177-200.

[3] Bergeron S. Y., Vincent A. P., Yuen D. A., Tranchant B. J. S., Tchong C. (1999): Viewing seismic velocity anomalies with 3-D continuous Gaussian wavelets. *Geophys. Res. Lett.* **26** (15), 2,311-2,314.

[4] Bindschadler D. L., Schubert G., Kaula W. M (1990): Mantle flow tectonics and the origin of Ishtar Terra, Venus. *Geophys. Res. Lett.* **17**, 1,345-1,348.

[5] Čadek O., Čížková H., Yuen D. A. (1997): Can long-wavelength dynamical signatures be compatible with layered mantle convection? *Geophys. Res. Lett.* **24** (16), 2,091-2,094.

[6] Čížková H., Čadek O., Yuen D. A., Zhou H. W. (1996): Slope of the geoid spectrum and constraints on mantle viscosity stratification. *Geophys. Res. Lett.* **23** (21), 3,063-3,066.

[7] Daubechies I. (1992): Ten Lectures on Wavelets. SIAM, Phila, PA.

[8] de Pater I., Lissauer J. J. (2001): Planetary Sciences. Cambridge University Press, Cambridge.

[9] Donahue T. M., Hodges R. (1992): Past and present water budget on Venus. *J. Geophys. Res.* **97**, 6,093-6,091.

[10] Donahue T. M. (1999): New analysis of hydrogen and deuterium escape from Venus. *Icarus* **141** (2), 226-235.

[11] Dubuffet F., Rabinowicz M., Monnereau M. (2000): Multiple scales in mantle convection. *Earth Planet. Sci. Let.* **178**, 351-366.

[12] Edmonds A. R. (1960): Angular Momentum in Quantum Mechanics. Princeton University Press, Princeton.

[13] Forte A. M., Mitovica J. X. (2001): Deep mantle high-viscosity flow and thermochemical structure inferred from seismic and geodynamic data. *Nature* **410**, 1,049-1,056.

[14] Grimm R. E., Phillips R. J. (1991): Gravity anomalies, compensation mechanisms, and the geodynamics of western Ishtar Terra, Venus. *J. Geophys. Res.* **96**, 8,305-8,324.

[15] Grinspoon D. H. (1993): Implications of the high D/H ration for the sources of water in Venus atmosphere. *Nature* **363**, 428-431.

[16] Gurnett D. A., Zarka P., Manning R., Kurth W. S., Hospodarsky G. B., Averkamp T. F., Kaiser M. L., and Farrell W. M. (2001): Non-detection at Venus of high-frequency radio signals characteristic of terrestrial lightning. *Nature* **409**, 313-315.

[17] Harder H., Christensen U. (1996): A one-plume model of Martian mantle convection. *Nature* **380**, 507-509.

[18] Hunten D. M., Colin L., Donahue T. M., Moroz V. I., Eds. (1983): Venus. Univ. of Arizona Press, Tucson.

[19] Jones M. N. (1985): Spherical Harmonics and tensors for Classical Field Theory. John Wiley, New York.

[20] Kaula W. M. (1966): Theory of Satellite Geodesy. Blaisdell Publication Company, Waltham MA.

[21] Kaula W. M. (1994): The tectonics of Venus. *Phil. Trans. Roy. Soc. London* **349**, 345-355.

[22] Kido M., Yuen D. A., Vincent A. P. (2003): Continuous wavelet-like filter for a spherical surface and its appplication to localized aadmittance function on Mars. *Phys. Earth Planet. Inter.* **135**, 1-16.

[23] Kiefer W. S., Richards M. A., Hager B. H., Bills B. G. (1986): A dynamic model of Venus's gravity field. *Geophys. Res. Lett.* **13**, 14-17.

[24] Kiefer W. S., Hager B. H. (1991): A mantle plumes model for the equatorial highlands of Venus. *J. Geophys. Res.* **96**, 20,947-20,966.

[25] Kiefer W. S., Hager B. H. (1992): Geoid anomalies and dynamic topography from convection in cylindrical geometry: application to mantle plumes on Earth and Venus. *J. Geophys. R.* **108**, 198-214.

[26] Kiefer W. S., Petersen K. (2003): Mantle and crustal structure in Phoebe Regio and Devana Chasma. *Geophys. Res. Lett.* **30** (1), 1,005-1,009.

[27] Konopliv A. S., Yoder C. F. (1996): Venusian k_2 tidal love number from Magellan and PVO tracking data. *Geophys. Res. Lett.* **23**, 1,857-1,860.

[28] Konopliv A. S., Banerdt W. B., Sjogren W. L. (1999): Venus Gravity: 180th Degree and Order Model. *Icarus* **139**, 3-18.

[29] Konopliv A. S., Asmar S. W., Carranza E., Sjogren W. L., Yuan D. N. (2001): Recent Gravity Models as a Result of the Lunar Prospector Mission *Icarus* **150**, 1-18.

[30] Kývalová H. (1994): Phase Transitionals and Earth Mantle Dynamics. UK MFF, Praha (*in Czech*).

[31] Larsen T. B., Yuen D. A. , Malevsky A. V., Smedsmo J. L. (1995): Dynamics of thermal convection with Newtonian temperature-dependent viscosity at high Rayleigh number. *Phys. Earth Planet. Int.* **89**, 9-33.

[32] Lemoine F. G., Smith D. E., Rowlands D. D., Zuber M. T., Neumann G. A., Chinn D. S. (2001): An improved solution of the gravity field of Mars (GMM-2B) from Mars Global Surveyor. *J. Geophys. Res.* **106** (E10), 23,359-23,376.

[33] Matas J. (1995): Mantle Viscosity and Density Structures – Comparison of Various Inverse Problem Formulations. UK MFF, Praha.

[34] McGovern P. J., Solomon S. C., Smith D. E., Zuber M. T., Simons M., Wieczorek M. A., Phillips R. J., Neumann G.A., Aharonson O., Head J. W. (2002): Localized gravity/topography admittance and correlation spectra on Mars: Implications for regional and global evolution. *J. Geophys. Res.* **107**, 19-35.

[35] McKenzie D. (1994): The relationship between topography and gravity on Earth and Venus. *Icarus* **112**, 55-88.

[36] McKenzie D., Nimmo F. (1997): Elastic thickness estimates for Venus from line of sight accelerations. *Icarus* **130**, 198-216.

[37] McKinnon W. B., Zahnle K. J., Ivanov B. A., Melosh H. J. (1997): Cratering on Venus: Models and observations. In *Venus II: Geology, geophysics, atmosphere and solar wind enviroment*, pp. 1,245-1,287. The University of Arizona Press, Tuscon.

[38] Michel V. (2002): Scale continuous, scale discretized, and scale discreate harmonic wavelets for the outher and inner space and their application to an inverse problem in geomathematics. *Appl. Comput. Harmon. Anal.* **12**, 77-99.

[39] Namiki N., Solomon S. C. (1994): Impact crater densities on volcanoes and coronae on Venus: Implications for volcanic resurfacing. *Science* **265**, 929-933.

[40] Nimmo F., McKenzie D. (1998): Volcanism and Tectonics on Venus. *Annu. Rev. Eart Planet Sci.* **26**, 23-51.

[41] Nimmo F. (2002): Why does Venus lack a magnetic field? *Geology* **30** (11), 987-990.

[42] Phillips R. J. (1990): Convection-driven tectonics on Venus. *J. Geophys. Res.* **95**, 1,301-1,316.

[43] Phillips L. J., McComas D. J. (1991): The magnetosheath and magnetotail of Venus. *Space Sci. Rev.* **55**, 1-80.

[44] Rappaport N. J., Konopliv A. S., Kucinskas A. B. (1999): An Improved 360 Degree and Order Model of Venus Topography. *Icarus* **139**, 19-31.

[45] Ratcliff J. T., Tackley P. J., Schubert G., Zebib A. (1997): Transitions in thermal convection with strongly variable viscosity. *Phys. Earth Planet Int.* **102**, 201-212.

[46] Ricard Y., Vigni C. (1989): Mantle dynamics with induced plate tectonics. *J. Geophys. Res.* **94**, 17,543-17,559.

[47] Rožek D. (2000): The geoid prediction for the intermediate wavelengths. UK MFF, Praha (*in Czech*).

[48] Sandwell D. T, Johnson C. L., Bilotti F., Suppe J.(1997): Driving forces for limited tectonics on Venus. *Icarus* **129**, 232-244.

[49] Schaber G., Strom R. G., Moore H. J., Soderblom L. A., Kirk R. L., Chadwick D. J., Dawson D. D., Gaddis, L. R., Boyce J. M., Russell J. (1992): Geology and distribution of impact craters on Venus: What are they telling us? *J. Geophys. Res.* **97**, 13,257-13,301.

[50] Schubert G. (1979): Subsolidus convection in the mantles of terrestrial planets. *Ann. Rev. Earth Planet. Sci.* **7**, 289-342.

[51] Schubert G., Spohn T., Reynolds R. T. (1986): Thermal histories, compositions and internal structures of the moons of the solar system. In *Satellites*, pp. 224-292. The University of Arizona Press, Tuscon.

[52] Schubert G., Solomatov V. S., Tackely P. J., Turcotte D. L. (1997): Mantle convection and the thermal evolution of Venus. In *Venus II: Geology, geophysics, atmosphere and solar wind enviroment*, pp. 1,245-1,287. The University of Arizona Press, Tuscon.

[53] Schubert G., Turcotte D. L., Olson P. (2001): Mantle Convection in The Earth and Planets. Cambridge University Press, Cambridge.

[54] Simons M., Solomon S. C., Hager B. H. (1997): Localization of gravity and topography: constrains on the tectonics and mantle dynamics of Venus. *Geophys. J. Int.* **131**, 24-44.

[55] Smith D. E., Zuber M. T., Neumann G. A., Lemoine F. G. (1997): Topography of the Moon from the Clementine lidar. *J. Geophys. Res.* **102**, 1,591-1,611.

[56] Smith D.E., Zuber M.T., Solomon S.C., Phillips R.J., Head J.W., Garvin J.B., Banerdt W.B., Muhleman D.O., Pettengill G.H., Neumann G.A., Lemoine F.G., Abshire J.B., Aharonson O., Brown C.D., Hauck S.A., Ivanov A.B., McGovern P.J., Zwally H.J., Duxbury T.C. (1999): The global topography of Mars and implications for surface evolution. *Science* **284**, 1,495-1,503.

[57] Solomatov V. S., Moresi L. N. (1996): Stagnant lid convection on Venus. *J. Geophys. Res.* **101**, 4,737-4,753.

[58] Spohn T., Schubert G. (2003): Oceans in the icy Galilean satellites of Jupiter? *Icarus* **161**, 456-467.

[59] Squyres S. W., Janes D. M., Schubert G., Bindschadler D. L., Moersch J. E., Turcotte D. L., Stofan E. R. (1993): The Spatial Distribution of Coronae and Related Features On Venus. *Geophys. Res. Lett.* **24**, 2,965-2,968

[60] Stein C., Hansen U. (2003): Self-Consistent Formation of a low Viscosity Zone. *AGU Fall Meeting*, Abs. No. T32B-0936.

[61] Steinbach V., Yuen D. A. (1992): The effect of multiple phase transitions on Venusian mantle convection. *Geophys. Res. Lett.* **19**, 2,243-2,246.

[62] Stevenson D. J., Schubert G., Spohn T. (1983): Magnetism and thermal evolution of the terrestrial planets. *Icarus* **54**, 466-489.

[63] Tarantola A. (1987): Inverse Problem Theory. Elsevier, Amsterdam.

[64] Torrence C., Compo G. P. (1998): A practical guide to wavelet analysis. *Bull. Am. Meteorol. Soc.* **79**, 61-78.

[65] Turcotte D. L. (1993): An episodic hypothesis for venusian tectonics. *J. Geophys. Res.* **98**, 17,061-17,068.

[66] Turcotte D. L., Shcherbakov R., Malamud B. D., Kucinskas A. B. (2002): Is the Martian crust also the Martian elastic lithosphere? *J. Geophys. Res.* **107** E11, 5,091-5,110.

[67] Varshalovich D. A., Moskalev A. N., Kjersonskii V. K. (1988): Quantum Theory of Angular Momentum. World Scientific, Singapore.

[68] Vecsey L., Matyska C. (2001): Wavelet spectra and chaos in thermal convection modelling. *Geophys. Res. Lett.* **28** (2), 395-398.

[69] Vecsey L. (2002): Chaos in Thermal Convection and The Wavelet Analysis of Geophysical Fields. UK MFF, Praha.

[70] Vecsey L., Hier Majumder C. A., Yuen D. A. (2003): Multiresolution tectonic features over the Earth inferred from a wavelet transformed geoid. *Vis. Geosci.* **8**, 26-44.

[71] Watts A. B. (2001): Isostasy and Flexure of the Lithosphere. Cambridge University Press, Cambridge.

[72] Wilhelms D. E. (1987): The Geologic History of the Moon. US Geological Survey Professional Paper 1348.

[73] Zuber M. T., Solomon S. C., Phillips R. J., Smith D. E., Tyler G. L., Aharonson O., Balmino G., Banerdt W. B., Head J. W., McGovern C. L., Neumann G. A., Rowlands D. D., Zhong S. (2000): Internal structure and early thermal evolution of Mars from Mars Global Surveyor topography and gravity. *Science* **287**, 1,788-1,793.

Internet References

[i1] **National Space Science Data Center**
http://nssdc.gsfc.nasa.gov

[i2] **University Corporation for Atmospheric Research**
http://www.windows.ucar.edu

[i3] **Massachusetts Institute of Technology**
http://www.mit.edu

[i4] **Planetary Data System**
http://pds.jpl.nasa.gov

[i5] **Homepage of Don Mitchell**
http://www.mentallandscape.com

[i6] **U.S. National Imagery and Mapping Agency EGM96 model**
http://www.nima.mil/GandG/wgsegm

[i7] **NOAA's National Geophysical Data Center**
http://www.ngdc.noaa.gov

[i8] **Eric Wolfram's World of Math**
http://mathworld.wolfram.com